AD 725 255

Semi-Annual Technical Report No. 3

(for period Feb. 2, 1971 to July 31, 1971)

Title: Steerable Volume and Surface Spin Waves in Ferrimagnetic Films

Contract No.: DAHC15 70 C 0190
ARPA Order No.: 1512
Program Code No.: D10

Name of Contractor: Massachusetts Institute of Technology
Cambridge, Mass. 02139

Principal Investigator: F.R. Morgenthaler
(617) 864-6900 Ext. 4623

Effective Date of Contract: Feb. 2, 1970
Contract Expiration Date: Feb. 1, 1973

Total Amount of Contract through Feb. 1, 1973 $420,000.

Funds Alloted through Feb. 1, 1972 $280,000.

Sponsored by
Advanced Research Projects Agency
ARPA Order No. 1512

DISCLAIMER NOTICE

THIS DOCUMENT IS THE BEST QUALITY AVAILABLE.

COPY FURNISHED CONTAINED A SIGNIFICANT NUMBER OF PAGES WHICH DO NOT REPRODUCE LEGIBLY.

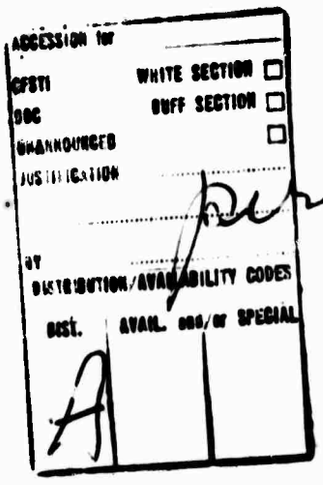

Per rept No. 3

The work reported in this document was made possible through support extended the Massachusetts Institute of Technology by the Advanced Research Projects Agency.

Unclassified
Security Classification

DOCUMENT CONTROL DATA - R&D

(Security classification of title, body of abstract and indexing annotation must be entered when the overall report is classified)

1 ORIGINATING ACTIVITY (Corporate author): Massachusetts Institute of Technology, Microwave and Quantum Magnetics Group/ Crystal Physics Laboratory, Dept. of Electrical Eng. and Ctr. for Materials Science and Engrg. Cambridge, Mass. 02139

2a REPORT SECURITY CLASSIFICATION: Unclassified

2b GROUP:

3 REPORT TITLE

Steerable Volume and Surface Spin Waves in Ferrimagnetic Films

4 DESCRIPTIVE NOTES (Type of report and inclusive dates)

Semi-Annual Technical Report No. 3 Feb. 2, 1971 - July 31, 1971

5 AUTHOR(S) (Last name, first name, initial)

Morgenthaler, Frederic R.

6 REPORT DATE	7a TOTAL NO. OF PAGES	7b NO. OF REFS
August 1, 1971	155	64

8a CONTRACT OR GRANT NO.	9a ORIGINATOR'S REPORT NUMBER(S)
DAHC 15 70 C 0190	Semi-Annual Technical Report No. 3
b. PROJECT NO.	
c.	9b. OTHER REPORT NO(S) (Any other numbers that may be assigned this report)
d.	

10 AVAILABILITY/LIMITATION NOTICES

11 SUPPLEMENTARY NOTES

Details of illustrations in this document may be better studied on microfiche

12 SPONSORING MILITARY ACTIVITY

Advanced Research Projects Agency
Arlington, Virginia 22209

13 ABSTRACT

This report describes in detail the technical progress made during the third six months of a three year interdisciplinary research program. One major goal of the program is the growth of yttrium-iron garnet (YIG), single crystals of high quality in both thin film and bulk form. Another is the development of novel techniques for controlling and studying energy propagation characteristics of volume and surface spin waves. One promising technique for accomplishing the former is the use of chemical vapor deposition (CVD) and our cumulative progress with this method is recounted fully. The latter goal is being met by a combination of optical and microwave techniques used to probe the dynamics of spin wave propagation. The optical experiments were described in the last semi annual report; our microwave propagation studies of magnetostatic surface spin waves in YIG slabs are presented herein.

DD Form 1473

Unclassified
Security Classification

14 KEY WORDS	LINK A		LINK B		LINK C	
	ROLE	WT	ROLE	WT	ROLE	WT
spin waves						
ferrimagnets						
microwaves						
yttrium iron garnet (YIG)						
chemical vapor deposition						
top seeded solution growth						
crystals						
thin films						
magnons						
magnetostatic						

INSTRUCTIONS

1. ORIGINATING ACTIVITY: Enter the name and address of the contractor, subcontractor, grantee, Department of Defense activity or other organization (*corporate author*) issuing the report.

2a. REPORT SECURITY CLASSIFICATION: Enter the overall security classification of the report. Indicate whether "Restricted Data" is included. Marking is to be in accordance with appropriate security regulations.

2b. GROUP: Automatic downgrading is specified in DoD Directive 5200.10 and Armed Forces Industrial Manual. Enter the group number. Also, when applicable, show that optional markings have been used for Group 3 and Group 4 as authorized.

3. REPORT TITLE: Enter the complete report title in all capital letters. Titles in all cases should be unclassified. If a meaningful title cannot be selected without classification, show title classification in all capitals in parenthesis immediately following the title.

4. DESCRIPTIVE NOTES: If appropriate, enter the type of report, e.g., interim, progress, summary, annual, or final. Give the inclusive dates when a specific reporting period is covered.

5. AUTHOR(S): Enter the name(s) of author(s) as shown on or in the report. Enter last name, first name, middle initial. If military, show rank and branch of service. The name of the principal author is an absolute minimum requirement.

6. REPORT DATE: Enter the date of the report as day, month, year, or month, year. If more than one date appears on the report, use date of publication.

7a. TOTAL NUMBER OF PAGES: The total page count should follow normal pagination procedures, i.e., enter the number of pages containing information.

7b. NUMBER OF REFERENCES: Enter the total number of references cited in the report.

8a. CONTRACT OR GRANT NUMBER: If appropriate, enter the applicable number of the contract or grant under which the report was written.

8b, 8c, & 8d. PROJECT NUMBER: Enter the appropriate military department identification, such as project number, subproject number, system numbers, task number, etc.

9a. ORIGINATOR'S REPORT NUMBER(S): Enter the official report number by which the document will be identified and controlled by the originating activity. This number must be unique to this report.

9b. OTHER REPORT NUMBER(S): If the report has been assigned any other report numbers (*either by the originator or by the sponsor*), also enter this number(s).

10. AVAILABILITY/LIMITATION NOTICES: Enter any limitations on further dissemination of the report, other than those imposed by security classification, using standard statements such as:

(1) "Qualified requesters may obtain copies of this report from DDC."

(2) "Foreign announcement and dissemination of this report by DDC is not authorized."

(3) "U. S. Government agencies may obtain copies of this report directly from DDC. Other qualified DDC users shall request through

_____."

(4) "U. S. military agencies may obtain copies of this report directly from DDC. Other qualified users shall request through

_____."

(5) "All distribution of this report is controlled. Qualified DDC users shall request through

_____."

If the report has been furnished to the Office of Technical Services, Department of Commerce, for sale to the public, indicate this fact and enter the price, if known.

11. SUPPLEMENTARY NOTES: Use for additional explanatory notes.

12. SPONSORING MILITARY ACTIVITY: Enter the name of the departmental project office or laboratory sponsoring (*paying for*) the research and development. Include address.

13. ABSTRACT: Enter an abstract giving a brief and factual summary of the document indicative of the report, even though it may also appear elsewhere in the body of the technical report. If additional space is required, a continuation sheet shall be attached.

It is highly desirable that the abstract of classified reports be unclassified. Each paragraph of the abstract shall end with an indication of the military security classification of the information in the paragraph, represented as (*TS*). (*S*). (*C*), or (*U*).

There is no limitation on the length of the abstract. However, the suggested length is from 150 to 225 words.

14. KEY WORDS: Key words are technically meaningful terms or short phrases that characterize a report and may be used as index entries for cataloging the report. Key words must be selected so that no security classification is required. Identifiers, such as equipment model designation, trade name, military project code name, geographic location, may be used as key words but will be followed by an indication of technical context. The assignment of links, rules, and weights is optional.

Semi-Annual Technical Report No. 3

(for period Feb. 2, 1971 to July 31, 1971)

Title: Steerable Volume and Surface Spin Waves in Ferrimagnetic Films

Contract No.: DAHC15 70 C 0190
ARPA Order No.: 1512
Program Code No.: D10

Name of Contractor: Massachusetts Institute of Technology
Cambridge, Mass. 02139

Principal Investigator: F.R. Morgenthaler
(617) 864-6900 Ext. 4623

Effective Date of Contract: Feb. 2, 1970
Contract Expiration Date: Feb. 1, 1973

Total Amount of Contract through Feb. 1, 1973 $420,000.

Funds Alloted through Feb. 1, 1972 $280,000.

Sponsored by
Advanced Research Projects Agency
ARPA Order No. 1512

ABSTRACT

This report describes in detail the technical progress made during the third six months of a three yesr interdisciplinsry research program titled: "Steerable Volume and Surface Spin Waves in Ferrimagnetic Films". One major goal of the program is the growth of yttrium-iron garnet (YIG), single crystals of high quelity in both thin film and bulk form. Another is the development of novel techniques for controlling and studying energy propagation characteristics of volume and surface spin waves. One promising technique for accomplishing for former is the use of chemical vepor deposition (CVD) and our cumulative progress with this method is recounted fully. The latter goal is being met by a combination of optical and microwave techniques used to probe the dynamics of spin weve propagetion. The optical experiments were described in the lest semi ennual report; our microwave propagation studies of magnetostetic surfsce spin waves in YIG slabs are presented herein. Specificelly:

Single crystal films of YIG up to 2.4 microns thick were grown epitaxially on nonmagnetic garnet substrates. The films were deposited by the chemical reaction of gaseous yttrium and iron chlorides with water vapor and/or oxygen in an open system et 1200°C and 2.5 Torr. Ferromagnetic resonance linewidths in the range of one oersted snd highly uniform domain patterns were observed on smooth and crack-free films deposited on GGG.

The thermodynamic characteristics of the system were examined through computer calculations of the equilibrium gas phase composition and of the free energy changes for deposition of various oxide phases. Certain experimental results are explained and the theoretical effects of changing certain growth conditions are examined using the results of the calculations.

It is proposed that the absence of vapor phase nucleation at low pressure and the relatively low rates of deposition in the present system are due to the high gas velocity through the deposition zone at reduced pressure.

The propagation of surface waves along a ferrite slab surface transversely magnetized in an arbitrary direction is studied theoretically and experimentally.

First, properties of volume magnetostatic waves are reviewed. The approach and techniques used are then applied to the case of surface waves.

Normal modes of a transversely magnetized ferrite slab are solved. Non-reciprocal surface modes with a well defined frequency band are shown to exist only when the angle between the magnetization and the slab surface is smaller than a certain critical angle. Beyond that angle, only discrete volume modes can be supported. Furthermore, the surface wave propagation constant and transverse mode pattern are controlled by the magnetization direction. The possibility of switching surface modes is discussed.

Experiments conducted for surface waves at 3.0 to 4.0 G.HZ. using fine wire excitation are discussed. The material used is a YIG single crystal slab with a (110) plane surface but magnetized transversely in (100) plane. Experimental results generally confirm all of the theoretical predictions except that the measured pulse delay time deviates from the theory mainly due to incomplete sample saturation.

I. INTRODUCTION

The Microwave and Quantum Magnetics Group and the Crystal Physics Laboratory, both within the M.I.T. Center for Materials Science and Engineering, have undertaken a three year interdisciplinary program in the area of "microwave magneto-ultrasonics" aimed at further developing several novel concepts which may lead to new and/or improved solid state devices employing electromagnetic/spin/elastic wave coupling. Device possibilities include multi-tapped delay lines, magnetoelastic beam switches and pulse compression filters. In particular, the research program will concentrate on the growth and exploitation of improved single crystal yttrium iron garnet substrates in which volume and surface spin wave propagating at microwave frequencies can be magnetically steered and/or otherwise controlled.

In order to produce crystals of yttrium iron garnet of the quality needed for the research envisioned in this program, two major constraints must be dealt with. First, the crystals must be of the necessary high quality to avoid introducing extraneous effects due to grain boundaries and strain inhomogeneities. The chemical purity is of major importance since rare earth impurities drastically increase spin wave relaxation rates. Second, the growth technique should permit ready fabrication of the types of structures desired, sich as multi-layer configurations and thin slabs. Consequently, both chemical vapor deposition (CVD) techniques and top seeded solution (TSS) growth appear attractive and both will be employed throughout the entire contract period. Thin films and bulk crystal substrates will be evaluated optically, magnetically and acoustically for purity, homogeneity and low losses. Promising specimens will be used for magnetostatic wave and exchange dominated spin wave propagation experiments at microwave frequencies.

A surface spin wave propagating parallel to an air-crystal boundary of a thin film has its energy largely confined within some characteristic distance that under certain conditions should be magnetically controllable. In one instance causing the energy to be closely confined to the surface and in another allowing it to spread out and fill the entire film. Volume spin waves are also subject to magnetic control. For example, beam steering is possible due to dipole-dipole interactions that in turn can be influenced through directional changes in the magnetizing field.

A high power (50 mw) He-Ne laser operating continuously at 1.15μ has been obtained for use in producing Bragg scattering from elastic and spin-elastic microwave packets within YIG crystals. This high resolution system which is now operational forms the basis for studies of spin-alastic conversion in spatial and/or temporal gradients of magnetic field.

The CVD furnace is operational and has to date produced a number of high quality YIG films. Microwave studies on the propagation of magnetostatic surface spin waves have been successful and have revealad the importance of a high degree of surface perfection.

The masters degree theses of R. Gentilman and J.K. Jao have been completed and form the basis of this report.

Dr. A. Linz has been assigned responsibility for overseeing the top-seeded solution crystal growth and chemical vapor deposition program, Professor D.J. Epstein for crystal evaluation with respect to magnetic properties and Professor F.R. Morgenthaler for microwave spin wave propagation studies; as principal investigator the latter has overall responsibility for coordinating the various phases of the research.

GROWTH OF YTTRIUM IRON GARNET (YIG) SINGLE CRYSTAL FILMS BY CHEMICAL VAPOR DEPOSITION (CVD)

by

Richard Gentilman

The material which follows is identical in content to a thesis submitted to the Department of Metallurgy and Materials Science on May 14, 1971, in partial fulfillment of the requirements for the degree of Master of Science.

TABLE OF CONTENTS

LIST OF FIGURES

LIST OF TABLES

I. INTRODUCTION

A. Yttrium Iron Garnet

Yttrium iron garnet (YIG) is a mixed oxide which is ferrimagnetic with properties that find application in magnetic devices operating at microwave frequencies. YIG is one of a class of synthetic materials produced by making ionic substitutions in the mineral "garnet", $Ca_3Al_2Si_3O_{12}$. The synthetic garnets have the general chemical formula:

$$3A_2O_3 \cdot 5B_2O_3 \quad \text{or} \quad A_3^{III}B_5^{III}O_{12}$$

where "A" is one or more of the following trivalent cations: Y or the rare earths Pm, Sm, Eu, Gd, Tb, Dy, Ho, Er, Tm, Yb, and Lu; "B" is one or more of: Fe, Al, and Ga.

The garnets possess cubic symmetry but not a simple crystal structure[1]. The large oxygen anions are not precisely close-packed. The "B" ions occupy tetrahedral sites, but the somewhat larger "A" ions are coordinated by 8 oxygens - four slightly more distant than the others. Eight $A_3B_5O_{12}$ units form a cubic unit cell of latice parameter 12.0 to 12.5Å. The room temperature lattice constant of YIG is 12.37Å; its X-ray density is 5.17 g/cc.

Only the iron garnets are ferrimagnetic. YIG has a Curie temperature of 550°K and the Curie points of all the other simple iron garnets fall within about 20°K of this temperature. The room temperature saturation magnetization ($4\pi M_s$) of YIG is approximately 1700 gauss.

The magnetization of YIG, like that of most ferrimagnetic substances, decreases smoothly and monotonically with increasing temperature and goes to zero at the Curie point. However, certain rare earth iron garnets exhibit drastically different $4\pi M_s$ vs. T relationships (Figure 1). Unlike

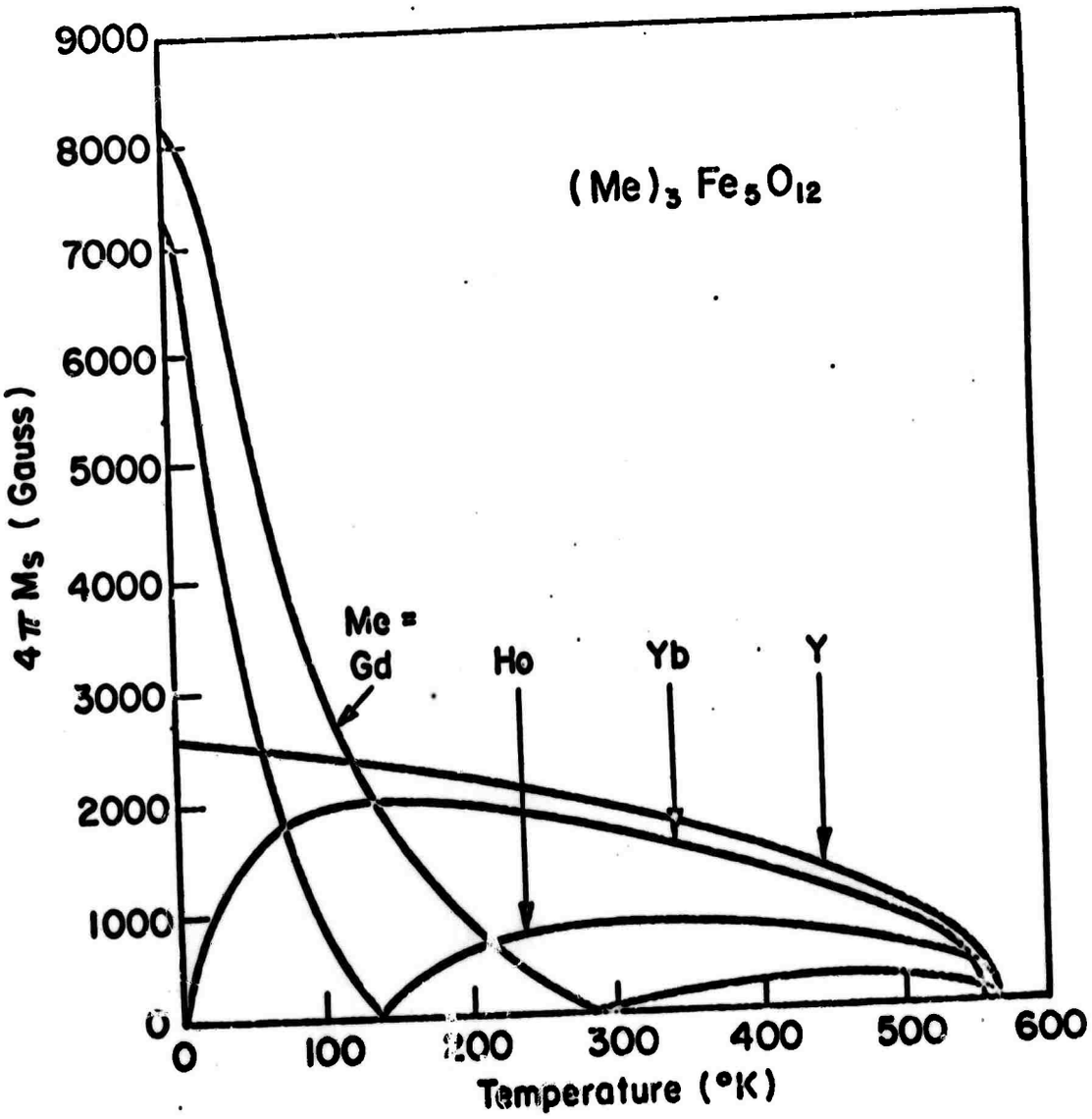

Figure 1: Temperature dependence of the magnetization of some iron garnets

Y^{III}, rare earth "A" cations make a small but significant contribution to the overall magnetization of the garnet - especially at low temperatures. In some rare earth garnets, this contribution causes a second point of zero magnetization at the "compensation" temperature somewhat below the Curie point[2]. By combining two or more different "A" ions, it is possible to produce a garnet with a temperature dependence of magnetization which is a superposition of those of the constituent simple garnets.

Other types of ionic substitutions are of interest. Replacing nonmagnetic Ca or Al for Fe decreases the saturation magnetization approximately linearly[3]. Fe^{III} ions can also be replaced by Si^{IV}. The substitution of silicon causes other iron cations to become divalent; thus the normally insulating crystal becomes electrically conductive. Other properties, such as magnetic anisotropy, magnetostriction, and lattice spacing similarly can be modified by mixing two or more simple garnets. Special purpose mixed garnets with up to six different cations have been reported[4], [5].

The particular characteristic which makes the magnetic garnets attractive for microwave applications is low magnetic loss in this frequency range compared with other magnetic materials. The parameter which characterizes microwave losses is the magnetic resonance linewidth. YIG has the narrowest linewidth of all known magnetic materials[6]. Due to its low loss characteristics, YIG classically has found application in various microwave magnetic components such as isolators, circulators, phase shifters, etc.[7]. However, the substitution of even small amounts of Si^{IV} for Fe^{III} or rare earth ions for Y^{III} causes a greatly increased linewidth in YIG[8].

Many new device applications and the minaturization of existing components can be envisioned if magnetic garnets can be prepared as thin single crystal films[9]. In particular, good quality films could be used as magnetoclastic surface wave devices. It is possible to manipulate or "steer" surface waves with magnetic fieldssuch that, in principle, signal processing can be done on the surface of the garnet film.[10] This leads to the possibility of developing integrated microwave circuitry analogous to present day electronic integrated circuits.

Other applications for magnetic garnet single crystal films have been suggested. One is for the bubble domain memory currently under development[11]. In this case, small cylindrical domains are created and propagated digitally within the film - each "bubble" corresponding to a binary "bit" of information. Pure YIG is not used for bubble materials because of the high magnetization. Instead, various ionic substitutions are made to reduce the magnetization (so that $4\pi M_s \approx 150$ gauss) and to produce a uniaxial anisotropy.

An additional potential application is to exploit the magnetooptic properties of transparent magnetic films in display devices.

In all the applications discussed, uniform and highly perfect films are required.

B. Chemical Vapor Deposition

Chemical vapor deposition (CVD) describes a process by which a solid phase is formed as the product of a chemical reaction involving one or more gaseous species. CVD was first used to form polycrystalline coatings of refractory metals but has since been used to produce a multitude of metals and compounds as polycrystalline deposits and single crystals[12].

CVD involves a material transport process as well as a chemical

reaction since the source of the reacting gases must be external to the reaction zone. In flow systems, reactant gases are transported to and by-product gases from the deposition zone by forced convection. In CVD systems, a gaseous metal halide is frequently used when the vapor pressure of the pure metal is too low at the deposition temperature.

As a crystal growth technique, CVD offers several advantages over other techniques. The growth process is isothermal; therefore, strains and other problems caused by thermal gradients inherent to pulling techniques are eliminated. High purity crystals can be attained because all reactants are gaseous and the transport process acts as a "distillation" against many potential impurities. Thirdly, CVD offers continuous and independent control over all reacting species since the flows of the gases can be readily metered and controlled. This type of control is absent in other crystal growth methods in which the composition is fixed by the initial batch composition.

Some unattractive features of CVD are: (1) CVD systems are inherently complicated due to the number of (particularly composition) parameters which need to be optimized and controlled, and (2) usually large single crystals (centimeter dimensions or larger) are not obtained.

CVD is well suited to the growth of epitaxial single crystal films by placing a suitable substrate single crystal in the deposition zone. The process is also ideal for creating composition gradients in crystals by simply changing certain gas flow rates with time.

C. Growth of YIG by CVD

Previously reported systems. The first reported growth of YIG by CVD was Linares and McGraw in 1964[13]. Utilizing the assumed overall reaction:

$$3YCl_3\ (gas) + 5FeCl_3\ (gas) + 12H_2O\ (gas) = Y_3Fe_5O_{12} + 24HCl\ (gas)$$

at atmospheric pressure and 1050-1150°C, these workers grew YIG crystals approximately 0.5 mm. in size for a 24 hour run. The following year, the same workers reported the growth of YIG films on $Y_3Al_5O_{12}$ (YAG), $Y_3Ga_5O_{12}$ (YGG), and $Gd_3Ga_5O_{12}$ (GGG) of an estimated thickness of 400 Å for a two hour run[14]. In the above work, a straight tube furnace with three temperature zones was used. Crucibles containing the solid metal chlorides were placed in the first two zones ($FeCl_3$ at 330°C, YCl_3 at 1050°C) in order to produce an equilibrium vapor pressure of 1 Torr. The chloride vapors were transported by a flow of argon to the third zone (T = 1100°C) and there reacted with "wet" oxygen.

Two years later, Mee et al.[15] reported what they called the first "proven" growth of epitaxial films of YIG on YAG and $Gd_3Fa_5O_{12}$ (GIG). (In their paper, these workers presented arguments intended to discount the results reported by Linares et al.). They assume an overall reaction of:

$$3YCl_3\ (gas) + 5FeCl_2\ (gas) + \frac{19}{2}H_2O\ (gas) + \frac{5}{9}O_2\ (gas) = Y_3Fa_5O_{12} + 19HCl\ (gas)$$

and deposit films at atmospheric pressure and about 1200°C in a T-shaped reactor. Later publications by the same workers[16],[17] report ferromagnetic resonance measurements on a variety of CVD-produced YIG films. Typical linewidth values were 12-15 oersted for YIG on YAG and 0.6-3.0 oersted for YIG on GGG. The linewidths for the latter case are extremely narrow and indicative of very high quality single crystal YIG. The somewhat larger linewidths observed for YIG on YAG are caused by the stresses in the film developed during cooling from the crystal growth temperature by the thermal expansion mismatch with the substrate[18].

Robinson et al.[19] have recently reported the epitaxial growth of mixed terbium erbium iron garnet by CVD. The system used was a straight tube furnace similar to that of Linares et al.[14]. One significant difference is that no water vapor was present in the system. Oxygen was the only oxidizing gas introduced into the deposition zone.

Stein[20] has reported the CVD growth of epitaxial GIG. The system and techniques used were closely modeled after those of Mee et al.[17]. Films 0.3 to 3.0 microns thick were grown during one hour runs at 1100-1200°C.

The above, previously reported YIG-CVD systems have several features in common: (1) the reaction of the metal chlorides with water vapor and/or oxygen occurs at one atmosphere pressure and about 1200°C, (2) the metal chloride vapors are produced by subliming the solid chlorides, (3) the forced flow of an inert gas transports the chloride vapors to the reaction zone.

None of the works report any investigation of the thermodynamic or kinetic characteristics of the CVD process. Some magnetic characterization of the films has been reported, but no serious attempt to relate magnetic properties to material characteristics or to the crystal growth conditions has been reported.

Comparison of present system with previous systems. The crystal growth system used in the present work differs in at least two significant respects from the previous systems: (1) the reaction occurs at reduced pressure (2-10) Torr) and with no appreciable flow of inert gas, and(2) gaseous metal chlorides are produced by direct chlorination of the metals:

$$Y + \frac{3}{2}Cl_2 = YCl_3$$
gas gas

$$Fe + \frac{3}{2}Cl_2 = FeCl_3$$
gas gas

In these respects, the present system is similar to those used by Schaffer[21] and Fonstad et al.[22] to grow high quality bulk single crystals of Al_2O_3 and SnO_2, respectively. In these systems, the metal chloride is generated in a chamber external to the growth furnace. In the present system, however, the chlorination reactions occur inside the furnace due to the higher temperatures required for suitable partial pressures of the chlorides.

One major advantage of direct chlorination to produce the gaseous chlorides is that direct control is available by metering the flow of chlorine to the reactors containing each meta. Since the chlorination reactions essentially go to completion for a wide range of temperatures, the chloride transport rate is, thus, independent of temperature and is determined by the input chlorine flow rate only. This direct control is attractive for the growth of ternary compounds like YIG. It is especially attractive for growing crystals with controlled composition gradients since the chloride transport rates can be systematically changed during a run. The chloride transport rate for the sublimation method used by the previous works, however, depends upon temperature, the inert gas flow rate, and the details of the gas flow patterns in the vicinity of the crucible containing the solid chloride.

D. Present Research Objectives

The object of the present work is to grow YIG as strain-free, epitaxial single crystal films of suitable dimensions on nonmagnetic

substrates. "Suitable dimensions" will be taken to be a minimum of 4 microns thick by 0.5 cm. on an edge. Films with these dimensions will be suitable for evaluating prototype magnetic device applications. In order to minimize the strains, it will be necessary to grow the films on substrates with similar thermal expansion coefficients. Fortunately, $Gd_3Ga_5O_{12}$ (GGG) has a lattice constant nearly identical to that of YIG and has a considerably closer thermal expansion match with YIG than other simple garnets.[18] GGG is, therefore, an ideal substrate. Good quality Czochralski grown GGG isnow commercially available. Ultimately, the quality of epitaxial YIG films will be limited by the quality of the substrate; defects present in the substrate are transmitted to the film as it grows.

The present work also will attempt to investigate the thermodynamics and the kinetic characteristics of the growth process. Also, initial attempts will be made to relate characteristics of the YIG films to crystal growth conditions.

II. EXPERIMENTAL PROCEDURES

A. Description of the System

A block diagram of the CVD system is given in Figure 2.

Pressure regulated flows of hydrogen, oxygen, and chlorine (three independent flows of chlorine) are metered through 150 mm. flowmeter tubes with spherical floats (Brooks; Matheson). The flowmeter tubes were individually calibrated and considerable deviation from manufacturer-supplied calibration curves was found. Hydrogen and oxygen calibrations were made with a precision volume displacement meter (Matheson). The chlorine flowmeters were calibrated both by displacement of a saturated chlorine and sodium chloride aqueous solution and by displacing helium into the precision volume meter. The calibrations obtained by these two methods used for chlorine agreed to within 2 percent.

Two needle valves - one upstream and one downstream - and a pressure gauge are used with each flowmeter. With this arrangement, both the pressure and the desired meter reading can be adjusted. This is important because the flowmeter calibration is correct only for a specific pressure (one atmosphere). There is a toggle-type shut-off valve in series with each needle valve since the latter are not designed for shut-off purposes.

The metal chloride generation and the CVD occur within a sealed alumina tube (54 mm. I.D.) inside a glo-bar heated furnace. The total heated zone is approximately 50 cm. long. Temperatures are measured with Pt/Pt-13% Rh thermocouples. In addition to the glo-bars running parallel with furnace tube, there are four glo-bars perpendicular with it in the second half of the heated zone. The temperatures of the two zones are independently controlled with SCR-type proportional controllers.

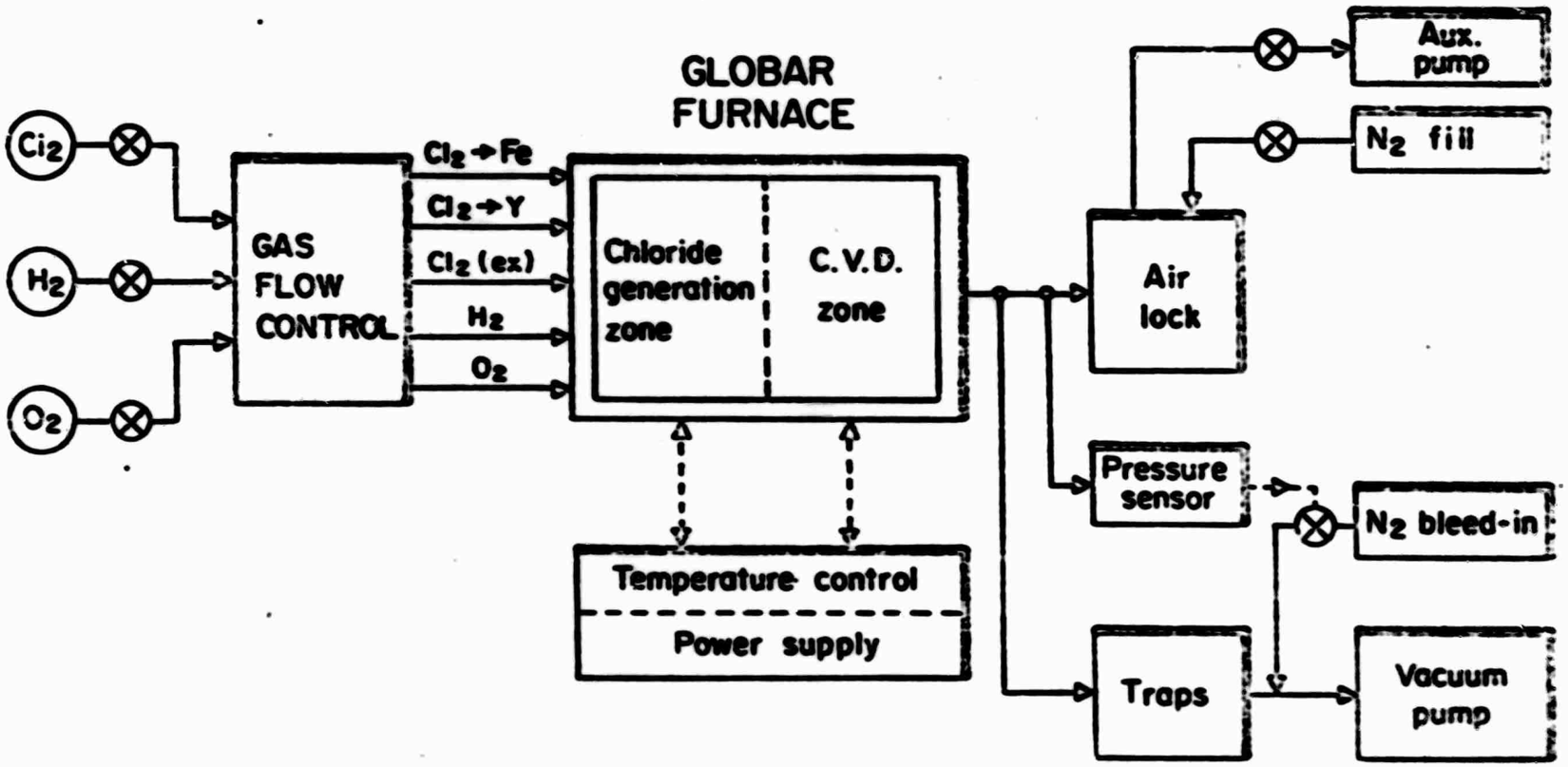

Figure 2: Block diagram of the CVD apparatus

The details of the interior of the furnace and the gas flow patterns are shown in Figure 3. The metal chloride generation occurs in the first half of the furnace. Two independent flows of chlorine enter the small alumina tubes containing the heated yttrium and iron metals, respectively. The chlorine reacts with the metal to produce the gaseous metal chloride. Yttrium chloride and iron chloride exit from the chlorinator tubes, mix inside the inner nozzle tube, and pass into the deposition zone along the center of the furnace tube.

Flows of excess chlorine (to be used to control the deposition rate) and hydrogen enter the furnace in the annulus between the inner and outer nozzle tubes. These gases enter the deposition as a cylindrical sheath surrounding the metal chlorides flow. Oxygen enters the furnace along the outside of the outer nozzle tube and enters the deposition zone along the inside diameter of the furnace tube.

With this gas injection scheme, the nozzle tubes isolate the chloride generation process from the other reactant gases. In addition the hydrogen and excess chlorine sheath surrounding the metal chlorides as they enter the deposition zone hinders the immediate mixing and reaction of oxygen with the chlorides. This scheme has been used in other CVD systems to prevent the build-up of oxide deposits on the ends of the nozzle tubes[21],[22]. Such build-up could alter the gas flow patterns during a run and even block off the injection orifices.

All the tubes named above are of high purity, dense alumina, and the ends of all tubes are sealed using Viton O-rings.

In the second zone, the CVD zone, the input gases mix and deposit the solid phase(s) thermodynamically and kinetically favored. The substrate crystals, YAG or GGG, sit on an alumina boat 10-15 cm. from the end of the gas nozzles. Under proper conditions, YIG is deposited

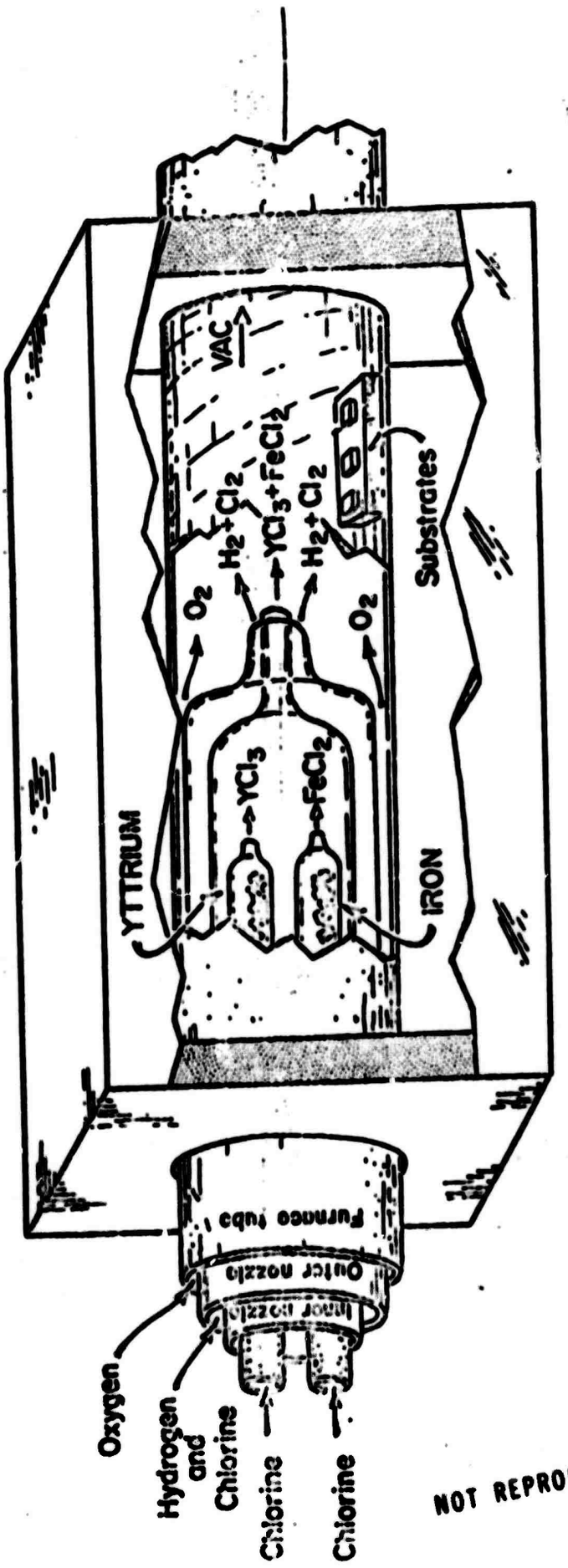

Figure 3: Details of the interior of the CVD furnace

epitaxially on the substrates. In the deposition zone, a fused silica tube is used as a liner to collect the deposited solids.

The unreacted and product gases pass out of the deposition zone and through two traps upstream from the mechanical vacuum pump. The first trap is a large glass jar with stainless steel bottles for collecting solid particles (mostly iron and yttrium chlorides) which have condensed in the gas phase. The second trap is a liquid nitrogen cold trap to freeze out chlorine and hydrogen chloride, thus protecting the pump from these corrosive species.

The system pressure is measured by two gauges connected to the system at the downstream end of the furnace tube. The first is a mechanical diaphram-type gauge (Heraus). This gauge is most accurate within the range from about 100 to 5 Torr. However, much of the present CVD work was conducted at approximately 2 Torr. Pressures in the range from about 10 to 0.1 Torr were measured with an electronic pressure sensing transducer (Rosemount). This sensor is also used to control the total pressure. The sensor output feeds an open loop servo circuit which controls the flowrate of nitrogen bled into the vacuum line just above the pump (Figure 2). If, for example, a negative pressure deviation is detected, the bleed-in flow is increased; this decreases the effective pumping rate to the rest of the system, thereby causing the pressure to rise to the proper value.

As one check on possible changing conditions in the system, the partial pressure of oxygen in the gas stream exiting from the furnace tube is measured with an oxygen analyzer (Thermo Lab). The instrument produces an electrical potential proportional to the oxygen pressure by ionic conduction of oxygen through a solid electrolyte of stabilized zirconia.

The oxygen partial pressure, the total system pressure, and the

temperature at three points along the furnace hot zone are continuously monitored on a strip chart recorder.

At the downstream end of the furnace tube is an airlock chamber. This double seal device is used for loading and unloading the substrate boat without breaking the vacuum or otherwise disturbing the system. With the inner glass window sealing the system, the boat is placed in the airlock and the outer glass window installed. The chamber is then evacuated by an auxilliary mechanical vacuum pump. The inner window is then withdrawn into a side compartment, and the boat is pushed into the deposition zone with an alumina rod inserted through a vacuum fitting on the outer window assembly. The rod is then withdrawn, the inner window returned to its original position, and the airlock chamber filled to atmospheric pressure with nitrogen. The boat can be withdrawn from the deposition zone by the same procedure.

Prior to the installation of the airlock, it was necessary to load the substrates before the run began. Thus, only one loading could be accomplished per run. In addition, the carefully polished and cleaned substrate surfaces may have been damaged during the relatively long exposure to the system during heatup and before the proper gas flow conditions were established.

B. Materials

(1) Source Metals. The yttrium metal used in the present work was obtained in the form of coarse chips from Research Chemicals. The metal is 99.99 percent pure with respect to rare earth element impurities but contains slightly less than one percent tantalum, the material used for the yttrium melting crucible. No other impurity species are present in excess of 0.03 percent according to the spectroscopic analysis supplied with the metal.

The iron used was analytical reagent purity and in the form of wire lengths approximately 8 cm. long and 0.035 cm. thick.

(2) Gases. All gases used in the present work were obtained through the M.I.T. Office of Laboratory Supplies from the following sources:

Gas (grade)	Source
Chlorine (high purity)	Matheson
Oxygen	Airco
Hydrogen (prepurified)	Airco
Helium	M.I.T. Cryogenic Lab
Nitrogen (prepurified)	Airco

All the gases were used without additional purification.

(3) Substrates. The first substrate material available for the present work was a Czochralski-grown boule of YAG doped with approximately 1 % neodymium. It was transparent but slightly purple due to the doping. The boule also contained macroscopic imperfections along the centerline due to coring which occurred during its growth. The room temperature lattice constant determined by X-ray diffration (using silicon as a standard) was 12.023 Å, whereas the published lattice parameter of "pure" YAG is 12.008 ± .003 Å[18]. The boule had been grown along the (111) direction and was approximately 1 cm. in diameter. Slices cut normal to the (100) direction were used as substrates.

Later, some slices from Czochralski boules of GGG were obtained courtesy of Bell Telephone Laboratories. Slices cut normal to the (110) and (111) directions were used in the later runs of the present work. The lattice parameter of the GGG (110) measured at room temperature was 12.367 Å and that for the (111) slices was 12.379 Å; the literature value is 12.375 ± .003 Å[18].

C. Substrate Preparation

A clean, undamaged, and strain-free substrate surface is necessary for successful epitaxial deposition[23]. The cut YAG and GGG slices were

ground flat with coarse and then fine SiC grits. This was followed by a polish with Linde-A Al_2O_3. Each substrate was polished until the surface appeared optically smooth at 10x magnification.

In order to remove the damaged surface layer due to mechanical polishing, a chemical polish step is required. A satisfactory chemical polish would remove about 3 microns of substrate without destroying the attained surface smoothness. Several workers have reported the use of hot phosphoric acid as an etch for garnets and similar materials[24],[25],[26]. For each substrate material and crystallographic orientation, there is a critical temperature range for the uniform removal of material. Lower temperatures cause pitting and higher temperatures promote the precipitation of phosphate compounds which can contaminate the surface. An associated problem is rinsing the hot acid from the substrate before it cools and causes pitting at lower temperatures. Rinsing in a water bath was found to cause sufficient thermal shock to crack the substrates, but use of oil eliminated cracking.

Substrates etched with hot phosphoric acid were used in the early runs of the present work. This chemical polishing method was found to be only partially successful, at best. Typically, the substrates were suspended in the acid at 285°C for about 30 seconds. The YAG (100) substrates maintained their surface smoothness fairly well, while GGG (110) slices were etched unevenly. Etching rates of about 10 microns per minute for YAG (100) and 30 microns per minute for GGG (110) were determined from weight loss measurements. Although the first successful epitaxial deposits in the present work were achieved on substrates etched with hot phosphoric acid, a reliable polishing procedure, particularly for GGG, was not found.

In later deposition runs, Syton HT-50 (Monsanto) was used for the

final substrate polish and found to be successful. Syton is a basic suspension of colloidal silica of particle size .035 to .040 microns. Syton is thought to polish by both mechanical and chemical means, but the actual mechanism is not understood[25]. The rate of material removal by Syton has been estimated as 3-6 microns per hour[25]. In the present work, an automatic set up was used to final polish the substrates with Syton for 30-45 minutes.

After the final polish, the subatrates were washed with mild soap and water and then rinsed successively in boiling acetone, isopropyl alcohol, and benzene for a minimum of five minutes in each. Before being used for deposition, each substrate was weighed on a Mettler analytical balance (accuracy ± .0003 gm).

D. Procedures for a Run

Iron and yttrium metal (typically 25 and 10 grams, respectively) are loaded into the chlorinator tubes and the combined weight of each tube and metal is recorded. Then the various furnace tubes are assembled as in Figure 3, and the entire system is sealed. The system is then pumped out for several hours.

Flows of helium of approximately 50 cc/min. are turned on through each chlorinator tube just before the furnace heat up begins. The furnace reaches the deposition temperature (typically 1200°C) in about three hours. During this time, the cold traps are filled and the chlorine gas line is pumped out to remove any residual air or water vapor.

The gas flows are turned on in the following sequence: (1) chlorine to the iron, (2) excess chlorine, (3) chlorine to the yttrium, (4) hydrogen, and (5) oxygen. Several minutes are required before stabilized flow rates with one atmosphere pressure in the flowmeter tubes are attained. The total pressure (typically 2 to 10 Torr) is then adjusted to the

proper value.

The boat carrying the substrates is placed in the airlock chamber and the chamber evacuated. Before the inner window is withdrawn and the substrate boat pushed into the deposition zone, the three chlorine flows are temporarily halted and replaced by helium flows. If this were not done, the metal chlorides would condense as liquids on the boat and substrates as they are pushed through the cooler regions of the furnace tube. It was found that although the chlorides re-evaporate when the boat reaches the hotter regions of the furnace, the brief contact with the substrates damages the surfaces due to the corrosive effects of the chlorides.

When the boat is in place in the deposition zone, the push rod is withdrawn, the inner window sealed, and the chlorine flows restored. At this point, the actual deposition commences. After the desired deposition time has elapsed, the chlorine flows are again replaced by helium, and the boat is pulled into the airlock to be reloaded if so desired.

After the last unloading, the power to the furnace and the gas flows are turned off, except that helium is again passed over the metals. When the system has cooled to room temperature (in about 12 hours), it is slowly brought up to atmospheric pressure and then disassembled and cleaned. The chlorinator tubes are weighed and the weight loss due to transport recorded. The nature and amounts of other deposits in the system (i.e., back diffused chlorides, growth on the injection nozzles, and other oxides deposited on the fused silica liner tube) are noted.

Each substrate is weighed after deposition, and the weight change is recorded.

E. Procedures for Characterization of Deposits

(1) Identification. All polycrystalline deposits were identified by X-ray diffraction powder patterns using a Norelco diffractometer unit.

Single crystal films were identified as YIG also using the diffractometer. Since all substrates were cut along a low index crystallographic plane, placing the substrate on the diffractometer will give diffraction from the lattice planes which are even integral multiples of this crystallographic plane. For epitaxial films a few microns thick, there is diffraction from both the film and the substrate. These two peaks can be resolved, particularly at high Bragg angles. For YIG on YAG, the difference in lattice constants is such that the respective (1200) reflections lie at Bragg angles differing by 4 degrees. For YIG on GGG, the (880) reflections differ by about 0.15 degrees; this difference, also, can be readily resolved on the diffractometer. Thus, by comparing the X-ray diffraction pattern from the film on the substrate with that from the bare substrate, the existence of epitaxial YIG can be confirmed.

YIG films can also be identified by color. Films a few microns thick are yellow-green and transparent. Thicker films are darker green; for thicknesses greater than about 25 microns, the films are black and opaque[17].

(2) Morphology and Thickness. The single crystal nature of the films was confirmed by Laue back reflection X-ray diffraction.

The surface morphology of the films and other deposits was observed by reflected light microscopy.

On some substrates, a small area of the deposited film was chipped off (perhaps due to rapid cooling during removal from the furnace) thus creating a "step" at the film-substrate interface. At such a step, the

film thickness could be measured by interference microscopy (Zeiss) using monochromatic light[27]. In other cases the film thickness was calculated from weight gain measurements.

(3) Magnetic Characterization. Ferromagnetic resonance linewidth is often considered to be the principle criterion of YIG quality. In the present work, linewidth is measured in a microwave cavity using a Varian E-9 EPR Spectrometer.

The resonance measurements are made using a constant D.C. magnetic field (produced by a large electromagnet) and a time varying field of microwave frequency (typically 9.55 Ghz). The microwave power is transmitted to the cavity containing the sample. Ferromagnetic resonance occurs at a particular D.C. field strength for the selected microwave frequency. At resonance, the YIG film sample absorbs some of the microwave power. The linewidth is determined by measuring the power output from the cavity (and, hence, the absorption by the sample) as a function of D.C. field strength. In the present work, the linewidth is taken to be equal to the width of the peak of absorption versus field strength at half power.

The results of linewidth measurements on thin films, however, are not unambiguous indications of crystal quality. The measured linewidth depends upon the details of film shape, thickness, edge smoothness, and orientation with respect to both the D.C. and microwave fields[28].

Magnetic domain patterns were observed by the Faraday effect using transmission microscopy with polarized light. The dynamic behavior of the domains in response to changing applied magnetic fields also can be observed by this technique.

III. RESULTS

A. Growth Conditions and Behavior of the System

A total of thirty-three runs were made during the present work. Oxide deposits were produced starting with Run 3. YIG first occurred as the predominant oxide (in powder form as the result of homogeneous vapor phase nucleation) during Run 7. Epitaxial films were produced on YAG substrates during Runs 14 and 16 and on GGG substrates during Runs 27 and 28.

Conditions for Epitaxial Deposition. The system parameters used for Runs 16 and 27 (the two most successful runs) are given in Table 1. Calculations of the equilibrium gas phase composition are presented in Section IV.

While the listed growth conditions produced single crystal YIG films on the substrates, it is unlikely that these are optimum conditions. Subsequent runs in which the same input conditions were used did not necessarily produce epitaxial films. Instead, polycrystalline YIG, $YFeO_3$, or Fe_2O_3 was deposited on the substrates. It is felt that some aspect of the present CVD system (the chlorination of the yttrium metal, in particular) lacks sufficient control.

After the approximate conditions for growth of epitaxial films had been established, the major emphasis of subsequent runs was to modify the parameters in order to achieve conditions for consistent film growth. The effects of changing certain parameters are described below:

(1) Increasing the temperature produced $YFeO_3$ on the substrate.

(2) Increasing the system pressure to 10 Torr or higher caused homogeneous vapor phase nucleation to occur. This resulted in powdery deposits.

Table 1

	Run 16	Run 27
Deposition Temperature (°C)	1180	1210
Pressure (Toor)	2.4	2.5
Flow rates (cc/min at S.T.P.)		
Hydrogen	30	29
Oxygen	19	19
Chlorine (excess)	10	5
Chlorine to Fe	41	21
Chlorine to Y	10	6
Helium (thru Y chlorinator)	40	10
Length of run (min.)	125	65
Substrate Deposition Rate (mg/cm^2-hr)	0.6	0.5

(3) Increasing the flow of excess chlorine tended to produce $YFeO_3$ and Y_2O_3, with no apparent change in total deposition rate.

(4) Elimination of hydrogen (and, therefore, H_2O and HCl as well) resulted in much less oxide deposit on the substrate.

Other Deposits in the System. After a run, three distinct regions of deposition are evident on the quartz liner tube. Near the gas nozzle tubes and 8-10 cm. downstream is a region of relatively heavy polycrystalline oxide deposit - on the order of a few millimeters in thickness. This deposit usually is a mixture of several phases, as determined by X-ray diffraction powder patterns. Similar deposits appear on the outside surfaces of the outer nozzle tube. This suggests that there is considerable turbulence as the gases enter the deposition zone from the nozzles causing mixing and some back flow.

Further downstream, from approximately 10 to 24 cm. from the nozzles, is a region of light and uniform deposition. Deposition rates for polycrystalline material on the quartz liner were measured to be on the order of 2-5 mg/cm^2-hr. Unlike the heavier deposition near the nozzle, the quartz liner tube is translucent in this second zone, though distinctly discolored by the deposited material. Usually, there is only one phase deposited in this region, though sometimes more than one phase is present. In the latter case, there is gradual change along the tube from one phase to the next. The more iron-rich phases appear farther downstream, in agreement with the observations of Mee et al.[17].

The epitaxial films are deposited in this second zone. In all the runs which produced single crystal YIG films, YIG was also the predominant phase which deposited on the boat and quartz liner in the vicinity of the substrates. However, the deposition rate for epitaxial YIG was approximately 0.5 mg/cm^2-hr.

Farther downstream (more than about 24 cm. from the nozzles) the temperature falls off sharply. Iron oxides (Fe_2O_3 and Fe_3O_4) are heavily deposited in this zone. Even farther downstream are heavy deposits of unreacted iron and yttrium chlorides which condense from the gas stream as room temperature is approached. Large amounts of unreacted chlorides were collected in the colder regions of the furnace tube and in the solid particle trap. It is estimated that only a few percent of the metal chlorides are reacted and deposited as oxides. Of this amount only a small fraction is deposited in the second, uniform region where the epitaxial growth occurs.

Invariably, there is also some undesireable oxide deposit on the gas nozzle outlets. The amount of this deposit was found to vary from run to run, probably depending upon the relative velocities of the gases emerging from the concentric orifices. In principle, the amount of nozzle build-up should be reduced and possibly eliminated by equalizing the gas flow velocities and by shaping the nozzles so as to reduce gas turbulence.

In all but the last few runs of the present research, considerable back diffusion of the metal chlorides was observed within the inner nozzle tube. Both iron chloride and yttrium chloride (identified by chemical analysis) diffused into this stagnant volume and condensed in the cooler regions. Typically about 25 percent of the chlorides produced was "lost" due to back diffusion. In the last few runs, a 50 cc/min flow of helium through the inner nozzle tube and outside of the chlorinators (Figure 3) eliminated the back diffusion and forced all the chlorides into the deposition zone.

Chlorination and Transport. In the present work, the amount of iron

chloride generated by chlorination of the metal was directly related to the input flow of chlorine gas. From weight loss measurements averaged over all the runs, 2.12 mg. of iron was consumed per cubic centimeter of chlorine flow. (The weight loss data for most runs agreed to within 10 percent of this average value.). This corresponds to an iron chloride composition of $FeCl_{2.35}$ (or 35 % $FeCl_3$-65% $FeCl_2$) assuming complete chlorination.

After a run, the remaining iron is only slightly discolored. The metal is consumed from the most upstream end of the chlorinator tube where the chlorine first contacts it. There is no evidence that any iron is consumed farther downstream in the chlorinator, nor is there present any oxide or residual chloride. This suggests that the iron chlorination is immediate and complete, which is as expected since the reaction is highly favored thermodynamically and the run temperature is above the boiling points of both $FeCl_2$ and $FeCl_3$[29].

The yttrium chlorination, on the other hand, is not nearly so ideal. Weight loss data varies radically from run to run and in some runs a weight gain was recorded. The residue in the yttrium chlorinator contains considerable Y_2O_3 and YOCl as well as the metal. The relative amounts of these species vary from run to run, even for runs with the same growth conditions. However, despite this inconsistent behavior, some metal is always chlorinated, as evidenced by the presence in the system of yttrium-containing oxide deposits and back diffused yttrium chloride.

The boiling point of YCl_3 is 1510°C and its vapor pressure is only approximately 10 Torr at the system temperature[30]. The undesired source of oxygen to the yttrium chlorinator tube appears to be back diffusion of oxygen (and/or water vapor) from the deposition zone. Since yttrium metal has a high oxidation potential, the oxygen competes with the

chlorination process when solid Y_2O_3 and YOCl are formed. In some of the runs, a flow of helium was passed through the yttrium chlorinator to augment the relatively low chlorine flow. It was hoped that the increased gas velocity through the chlorinator tube would retard the back diffusion, but this procedure did not significantly reduce the formation of Y_2O_3 and YOCl.

In addition to the run to run discrepancies of the yttrium chlorination, there are indications that the chlorination rate changed during the course of a run. Longer runs (3-5 hours) were attempted in hope of producing thicker epitaxial films. In several of these runs, however, there was evidence that YIG was deposited initially but sometime later during the run another phase was deposited on top of the film. The low vapor pressure of YCl_3 and the back diffused oxygen appear to be the causes of the erratic behavior of the yttrium chlorination.

B. Structure and Properties of the Single Crystal YIG Films

1 Physical Properties

Visual. The YIG films are transparent and green in color. The films deposited on YAG (100) are heavily crazed by stresses caused by the thermal expansion mismatch between YIG and YAG[18]. The tensile cracks appear in a regular orthogonal pattern (Figure 4) with intercrack spacings on the order of 50 μm. The cracks lie in (100) directions of the film, as determined by Laue back reflection patterns. Weight gain measurements indicate a film thickness of 2.4 ± 0.5 microns.

The YIG films deposited on GGG (110) and (111) substrates are not cracked because of better thermal expansion match between YIG and GGG (relative to that between YIG and YAG)[18]. An interferogram of a portion of a (110) film from Run 27 is shown in Figure 5. A section of the YIG deposit has chipped away. The distance between interference

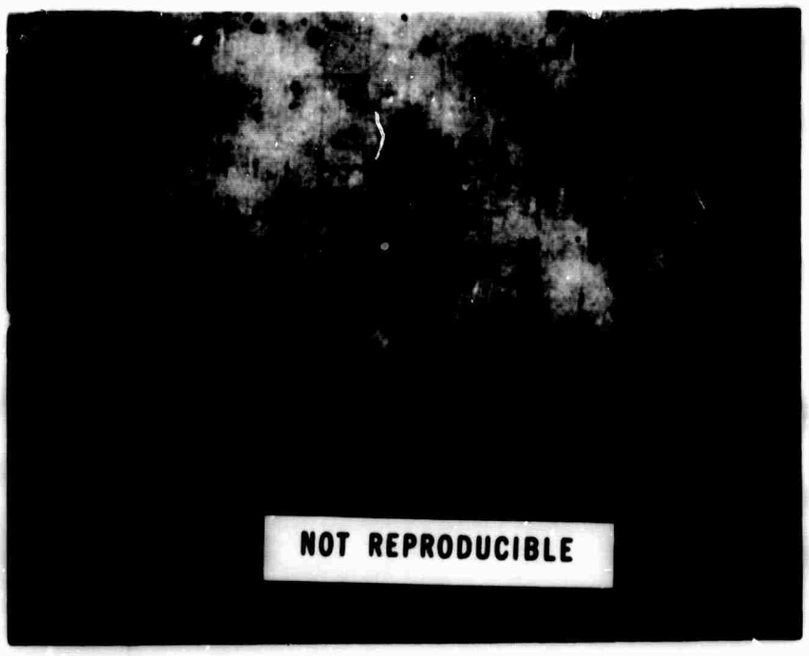

Figure 4: YIG film on YAG (100) substrate showing characteristic crack pattern. (80 X)

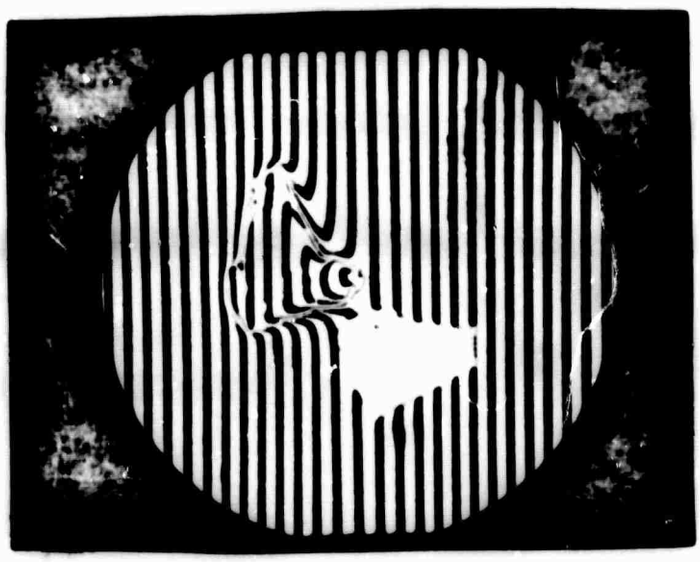

NOT REPRODUCIBLE

Figure 5: Interferogram of YIG film on GGG (1[illegible]0) substrate with a small piece of film chipped off. Fringe displacement across step gives film thickness of 1.13 ± .05 microns.

fringes is one-half the wavelength of thallium light ($\lambda = 0.535$ microns). By measuring the fringe displacement across the step where the film is missing, the film thickness is determined to be 1.13 ± 0.05 microns.

For all the single crystal films, the surface smoothness is the same as the original smoothness of the substrate. Isolated inhomogeneities which are present on all the films appear to be due to residual imperfections from the substrate polishing. Near edges of the substrate that were cut with a diamond saw, there are chipped surfaces. During the deposition run, single crystal YIG free of the inhomogeneities present on the polished surface grew on these "as fractured" surfaces.

Lattice Parameters. Using silicon as a standard, the lattice parameter of the YIG films was measured at fairly high Bragg angles. The results are given in Table 2.

The measured lattice parameters are somewhat smaller than the literature value of 12.376 ± .003 Å[18]. To be sure, the YIG films are somewhat strained due to the thermal expansion mismatch with the substrate. However, the strain present is a tensile strain, whose effect would be to increase, not decrease, the lattice constant of the YIG film.

2 Magnetic Characteristics

Observation of Domains. Magnetic domain patterns for YIG on YAG made visible with polarized light are shown in Figure 6. The irregular "fingerprint" pattern is characteristic of the highly strained films. The spacing between domains is approximately 3 microns. In a ferromagnetic film, the domain spacing is proportional to the film thickness and inversely proportional to the square of the magnetization. Both the thinness of the film and the high magnetization of YIG combine to produce such a narrow spacing. The domain pattern can be "wiggled" by moving a small

Table 2

Substrate & Orientation	Diffracting Plane	Lattice Parameter
YAG 100	(12 0 0) [2θ≈96°]	12.345 Å
GGG 110	(8 8 0) [2θ≈90°]	12.354 Å
GGG 110	(8 8 8) [2θ≈119°]	12.348 Å

Figure 6: Domain pattern of YIG film on YAG (100) substrate as revealed by polarized light. Note cracks and irregular "fingerprint" domain pattern (600 X).

magnet near the substrate. The domain mobility, however, is somewhat restricted due to the cracks and high strain in the film.

Domain patterns for YIG on GGG (110) are shown in Figure 7. Note that the pattern is very uniform with highly parallel domains. The domain spacing is about 2 microns. For YIG on GGG, the domains are considerably more mobile. The zig-zag pattern shown in Figure 7-b frequently appears after the domains have been moved with a hand magnet. The angle of the zig-zag is 115 ± 5 degrees.

Resonance Experiments. Microwave resonance measurements were attempted on several irregularly shaped samples of YIG films. Direct measurement of ferromagnetic resonance linewidth was complicated by the presence of many often overlapping peaks. There are two sources of the multiple peaks. Numerous magnetostatic resonance modes exist in any sample which is not a perfect sphere. In thin films, these modes occur at regular intervals from the primary resonance. The second source of multiple peaks is due to microscopic shape irregularities. Dillon[28] has reported that even minute voids or defects cause a single resonance peak to split into many peaks. Both regular mode patterns and peak splitting were observed in the present experiments.

Resonance linewidths were estimated from the strongest peak present in the spectrum. Estimated values for resonance with the D.C. magnetic field parallel with and normal to the plane of the film are given in Table 3.

The linewidths are of the same order as results reported by Mee et al.[17]. The extremely low linewidth for perpendicular resonance for the YIG on GGG (110) is somewhat uncertain due to the highly complex spectrum of that sample. The linewidth was taken from the strongest of many peaks

NOT REPRODUCIBLE

A.

B.

Figure 7: Domain pattern of YIG film on GGG (110) substrate as revealed by polarized light. (A) Highly parallel domains. (B) Zig-zag pattern which frequently occurs after domains have been moved with an external magnetic field. (760 X)

Table 3

Substrate & Orientation	Thickness (μm)	Linewidth (oersted) [and Resonance Field Strength (gauss)] perpendicular	parallel
YAG 100	2.4	----	14 [2680]
GGG 110	1.1	0.05* [5000]	0.8 [2660]
GGG 111	0.7	2.0 [4750]	8.5 [2670]

* Some uncertainty of this measurement due to highly complex spectrum.

present, though the widths of other nearby peaks were approximately the same as the strongest peak.

IV. DISCUSSION

A. Thermodynamic Considerations

Yttrium iron garnet is not the only solid deposit which can be produced from the vapor phase reaction of yttrium and iron chlorides with oxygen or water vapor. Frequently Y_2O_3, $YFeO_3$, and Fe_2O_3 as well as YIG (and occasionally Fe_3O_4 or YOCl) also appear in the present system. Mee et al.[17] report regular deposition zones in their furnace tube, with Y_2O_3 appearing most upstream followed in succession downstream by distinct zones of $YFeO_3$, YIG, and Fe_2O_3.

In the absence of a preferential substrate, the most favored solid phase is the one whose CVD reaction has the largest free energy decrease with respect to the actual composition of the gas in the system (i.e., the reaction with the largest chemical driving force).

A computer program was written to calculate (1) the equilibrium composition of the gas phase (given temperature, pressure, input gas flows, and thermodynamic data for the possible resulting gas species), and (2) the free energy changes of each of the possible CVD reactions.

Assumptions. The following assumptions were made:

(1) All gas species are in equilibrium with each other at the system temperature and total pressure.

(2) All gases are ideal, and all solid phases are pure (i.e., the solid phases have unit activity).

(3) The only gas species present in the system are the following ten: O_2, H_2, Cl_2, HCl, H_2O, Cl, $FeCl_2$, $FeCl_3$, YCl_3, and He. No lower chlorides of yttrium have been reported in the literature. Additional iron chloride species, such as FeCl and Fe_2Cl_6, are known to exist. However, order-of-magnitude calculations using the reported thermodynamic data[29]

indicate that these chlorides are present only in very minute quantities within the temperature and total pressure ranges applicable to the present system (1200 to 1700°K and 1 to 10^{-3} atmospheres). Other known gas species (e.g., H, O, O_3, H_2O_2, OH, ClO_2, Cl_2O, HClO, Fe, Y) are similarly neglected because they are not present in significant amounts according to the thermodynamic data.

(4) The chlorination reactions

$$Y + \tfrac{3}{2}Cl_2(g) = YCl_3(g)$$

$$Fe + \tfrac{3}{2}Cl_2(g) = FeCl_3(g)$$

go to total completion. In the case of iron, it is further assumed that the iron chloride formed initially is $FeCl_3$ (the higher vapor pressure specie) and not $FeCl_2$.

(5) Any change of gas composition resulting from the deposition of a condensed phase is negligible. This is thought to be a good assumption because of the high gas velocity of the system (Section IV-B) and because the observed fraction of chlorides which are oxidized is very small.

(6) YCl_3 and He (and O_2, when no hydrogen is present in the system) do not interact with other gas species and thus do not influence the equilibrium gas composition. Therefore, these species are considered to be "inert" with respect to the other gases present.

Basis of the Calculation - Gas Phase Composition. The variables of the system are temperature, total pressure, and input flow rates of hydrogen, oxygen, excess chlorine, chlorine to the iron, chlorine to the yttrium, and helium. Considering helium and yttrium chloride for the moment to be inert, mass balances for hydrogen oxygen, chlorine, and iron can be written:

$$[H_2]_o = [H_2] + [H_2O] + \frac{1}{2}[HCl]$$

$$[O_2]_o = [O_2] + \frac{1}{2}[H_2O]$$

$$[Cl_2 \rightarrow Fe]_o + [Cl_2(ox)]_o = [Cl_2] + \frac{1}{2}[Cl] + \frac{1}{2}[HCl] + [FeCl_2] + \frac{3}{2}[FeCl_3]$$

$$\frac{2}{3}[Cl_2 \rightarrow Fe]_o = [FeCl_2] + [FeCl_3]$$

where: $[x]$ = number of moles of "x"

$[x]_o$ = <u>input</u> number of moles of "x"

For unit time, the number of moles of each input gas specie is proportional to the flow rate. Since the mole <u>fraction</u> of each specie is the quantity of real interest, the proportionality constant relating "flow rate" and "number of moles" is arbitrary. Therefore, for convenience, the number of moles of each input gas can be set equal to its flow rate.

The various interacting gases are also related by four independent chemical reactions:

$$H_2 + \frac{1}{2}O_2 = H_2O \qquad (1)$$

$$H_2O + Cl_2 = 2HCl + \frac{1}{2}O_2 \qquad (2)$$

$$Cl_2 = 2Cl \qquad (3)$$

$$FeCl_3 = FeCl_2 + \frac{1}{2}Cl_2 \qquad (4)$$

Associated with each reaction is an equilibrium constant, K:

$$K_1 = \frac{P_{H_2O}}{P_{H_2}(P_{O_2})^{\frac{1}{2}}} = \frac{X_{H_2O}}{X_{H_2}(X_{O_2})^{\frac{1}{2}} P_T^{\frac{1}{2}}} = \frac{[H_2O]\{[H_2O] + [H_2] + [O_2]\}^{\frac{1}{2}}}{[H_2][O_2]^{\frac{1}{2}} P_T^{\frac{1}{2}}}$$

$$K_2 = (\text{etc.}) = (\text{etc.}) = \frac{[HCl]^2[O_2]^{\frac{1}{2}} P_T^{\frac{1}{2}}}{[H_2O][Cl_2]\{[HCl] + [O_2] + [H_2O] + [Cl_2]\}}$$

$$K_3 = (\text{etc.}) = (\text{etc.}) = \frac{[Cl]^2 P_T}{[Cl_2]\{[Cl_2] + [Cl]\}}$$

$$K_4 = (\text{etc.}) = (\text{etc.}) = \frac{[FeCl_2][Cl_2]^{\frac{1}{2}} P_T^{\frac{1}{2}}}{[FeCl_3]\{[FeCl_2] + [FeCl_3] + [Cl_2]\}}$$

where: P_T = total pressure (atm.)

X_i = mole fraction of "i" $\left(X_i = \frac{[i]}{\sum_{\text{all species}} [j]}\right)$

P_i = partial pressure of "i" (atm.) $(P_i = X_i P_T)$

At equilibrium:

$\Delta G^\circ_R = RT \ln K$

and, in general:

$$\Delta G^\circ_R = \sum_{\text{products}} n_i \Delta G^\circ_{F,i} - \sum_{\text{reactants}} n_j \Delta G^\circ_{F,j}$$

where: ΔG°_{R} = standard free energy change for the reaction (cal/mole)

$\Delta G^{\circ}_{F,i}$ = standard free energy of formation for specie "i" (cal/mole)

R = gas constant: 1.98 cal/mole-°K

T = absolute temperature (°K)

Therefore, for a given temperature, total pressure, and set of input flow rates, if the standard free energies of formation of the various species are known, the number of moles of the eight interacting gas species can be determined by solving the above eight equations (four mass balances and four reaction equilibria) simultaneously. The four reaction equilibria equations are nonlinear, and, therefore, the system of eight equations must be solved numerically.

If hydrogen is omitted from the system the thermodynamics are somewhat simplified. In this case, no H_2, H_2O, or HCl will be present; O_2 will be the only oxygen containing gas and will not interact with any other gases present. Thus, the calculation reduces to solving four equations with four unknowns. Only the iron and chlorine mass balances and reactions (3) and (4) need to be considered.

Once the number of moles of each specie (including the "inert" species) has been determined, the respective mole fractions and partial pressures can be calculated directly.

The Deposition Reactions. With the equilibrium gas composition known, the thermodynamic favorability of the various CVD reactions can be determined. Fourteen deposition reactions are considered. Y_2O_3, $YFeO_3$, YIG, and Fe_2O_3 are the possible solid phases. In each case, the chlorides can be oxidized by oxygen or water vapor (if present). Either $FeCl_3$ or $FeCl_2$ can be the reactant when $YFeO_3$,

YIG, or Fe_2O_3 is formed. The fourteen reactions can be written in a compact form as:

$$n_1\,YCl_3 + n_2\begin{bmatrix}FeCl_3\\FeCl_2\end{bmatrix} + n_3\begin{bmatrix}O_2\\H_2O\end{bmatrix} \rightarrow \begin{bmatrix}Y_2O_3\\YFeO_3\\Y_{.75}Fe_{1.25}O_3\\Fe_2O_3\end{bmatrix} + n_4\begin{bmatrix}Cl_2\\HCl(+\ a_4'H_2)\end{bmatrix}$$

where: n_i = the appropriate stoichiometric coefficients. From each set of brackets, one specie is selected for each reaction.

In general, the free energy change associated with a chemical reaction is:

$$\Delta G = \Delta G^{\circ} + RT\ \ln Q \qquad (5)$$

where:

$$Q = \frac{\text{products } \prod a_i^{n_j}}{\text{reactants } \prod a_i^{n_i}}$$

a_k = activity of "k" $\begin{cases} = P_k, \text{ for ideal gas} \\ = 1, \text{ for pure solid} \end{cases}$

n_k = stoichiometric coefficient

At equilibrium:

$$\Delta G = 0$$

Therefore:

$$\Delta G^{\circ} = -RT\ \ln Q_{eq} = -RT\ \ln K \qquad (6)$$

Substituting (5) into (4):

$$\Delta G = -RT\ \ln(K/Q)$$

For CVD reactions, (K/Q) is defined to be the supersaturation. Thus, "supersaturation" and "free energy charge" are directly related parameters for determining the thermodynamic favorability of a deposition reaction.

For each reaction, the parameters Q, ΔG°, K, K/Q, and ΔG are calculated.

The Computer Program. A flow chart of the computer program is given in Figure 8. The main program calls for a subroutine to solve the set of simultaneous, non-linear equations by an iterative method. The subroutine was based on a library subroutine of the M.I.T. Computation Center[31] but was somewhat modified by the author to improve the chances for convergence.

A typical page of print-out by the program (for Run 16) is shown in Figure 9. The program can be run as many times as desired with different input conditions and/or modified thermodynamic data. Thus, it is possible to determine the theoretical effect of changing any of the CVD growth conditions on the relative thermodynamic favorability of the various deposits.

Thermodynamic Data. The standard free energies of formation for most of the chemical species considered in the present calculations were taken from the JANAF tables and elsewhere in the literature. For use with the computer program, the data was approximated by a linear function over the temperature range 1200 to 1400°K as:

$$\Delta G^\circ_F(T) = A + BT \text{ (kcal/mole)}$$

Values of A and B for the various species along with the accuracy and source of the data are given in Table 4.

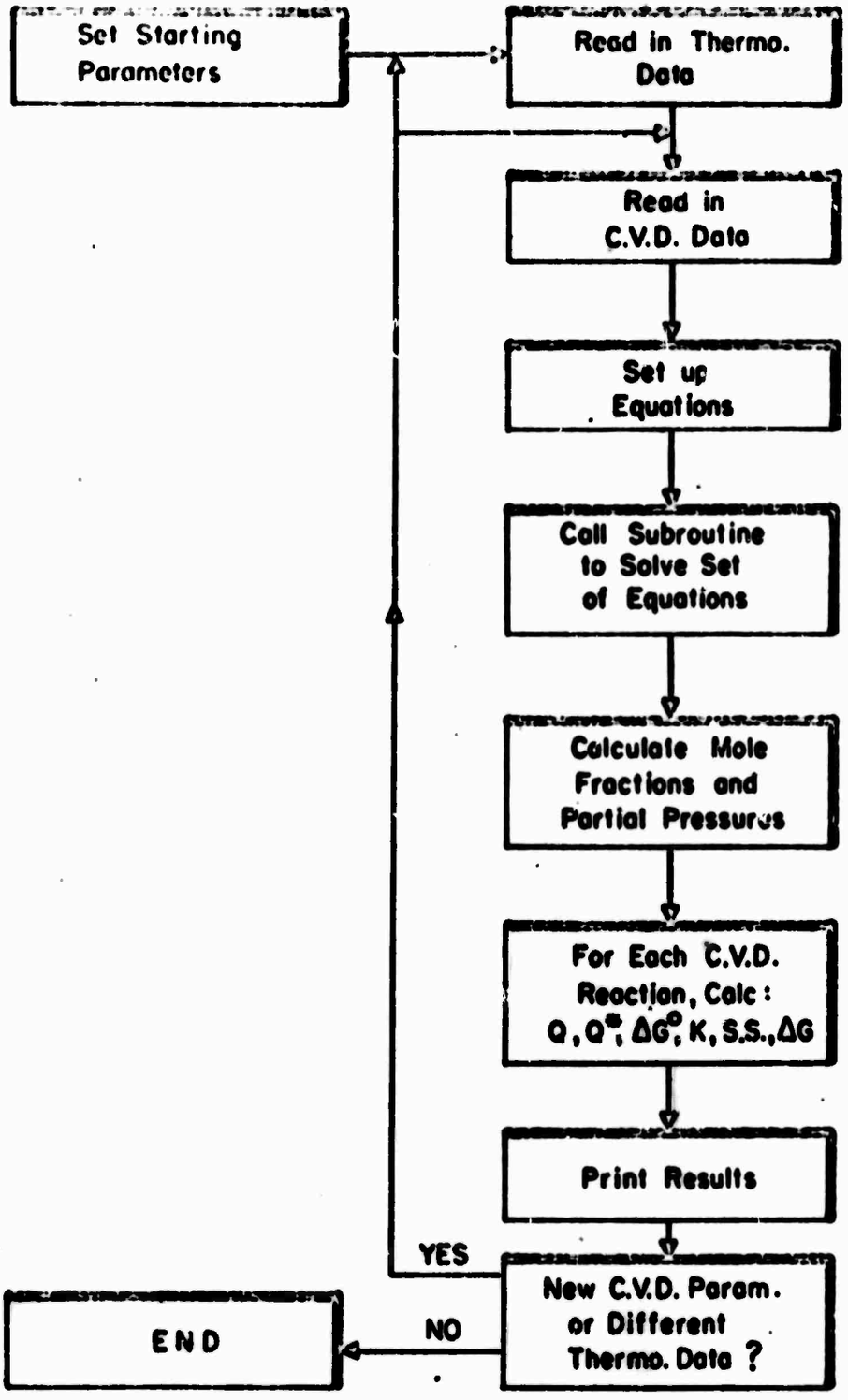

Figure 8: Flow chart of computer program for thermodynamic calculations.

TEMPERATURE = 1177 DEG.C= 1499 DEG.K
TOTAL PRESSURE = [illegible] ATM. = 2.4 TORR

INPUT FLOWS (CC/MIN AT S.T.P.)

N2	3[illegible]
O2	19.[illegible]
CL2 (A)	1[illegible]
CL2 - FE	41.[illegible]
CL2 - V	1[illegible]
OTHER	4[illegible]

ASSUMED DELTA G STD. OF FORMATION

V2O3	= -357.14	FECL3	= -52.90	H2O	= -46.00
VFEO3	= -237.65	FECL2	= -47.60	HCL	= -24.79
O25VIG	= -295.19	VCL3	= -1[illegible]3.79	CL	= 9.15
FE2O3	= -1[illegible]7.				

GAS COMPOSITION MOLE FRACTION PARTIAL PRESSURE (ATM)

O2	3.1[illegible]7727	(3.[illegible]377E-01)	6.[illegible]0340319 (3.40319E-04)
N2	3.[illegible]813	(3.[illegible]691E-01)	9.[illegible]C16440 (1.00440E-04)
FECL3	3.[illegible]36716	(3.[illegible]716E-02)	8.[illegible]C02121 (2.12008E-05)
FECL2	2.[illegible]34613	(2.[illegible]1848E-[illegible])	6.[illegible]858361 (5.83615E-04)
VCL3	3.[illegible]00716	(3.[illegible]4672E-01)	9.[illegible]C14752 (1.47525E-04)
N2	3.[illegible]	(3.[illegible]97593E-[illegible])	3.[illegible] (3.[illegible]810E-[illegible])
HCL	3.[illegible]18734	(3.[illegible]3[illegible]8E-[illegible])	9.[illegible]C[illegible]C672 (1.[illegible]CC67E-03)
CL2	3.[illegible]2[illegible]17	(3.[illegible]2917E-02)	8.[illegible]C[illegible]3037 (6.30807E-06)
CL	3.[illegible]2123	(3.[illegible]2123E-02)	8.[illegible]C[illegible]6671 (8.76526E-06)
[illegible]	3.[illegible]2[illegible]2	(3.[illegible]2[illegible]3E-[illegible])	8.[illegible]C[illegible]68519 (8.[illegible]54[illegible]E-04)

DEPOSITION REACTION DATA

PRODUCT V2O3	PRODUCT VFEO3	PRODUCT O25VIG	PRODUCT FE2O3	INITIATOR N2	INITIATOR H2O	FE SOURCE FECL3	FE SOURCE FECL2	[illegible] @ [illegible]	[illegible] @ STAR [illegible]	(KCAL/MOLE) DEL G STD	K (EQUIL)	K (EQUIL)/Q SUPERSATURATION	(KCAL/MOLE) DELTA G
				•				1.89168E-03	1.[illegible]63[illegible]E-04	-25.74	7.[illegible]8291E 03	4.[illegible]1388E 06	-43.74
	•			•		•		1.[illegible]3159E-02	7.[illegible]3945E-04	-19.65	7.[illegible]6213E 02	5.[illegible]7919E 04	-31.49
	•			•			•	1.[illegible]8467E-01	5.[illegible]9834E-04	-24.35	4.[illegible]8279E 03	2.[illegible]5485E 04	-29.13
		•		•		•		2.[illegible]1370E-02	1.[illegible]2[illegible]69E-03	-14.79	1.[illegible]7275E 02	8.[illegible]C83EE 03	-25.83
		•		•			•	5.[illegible]9942E-[illegible]	9.[illegible]2102E-04	-21.42	1.[illegible]7361E 03	2.[illegible]6964E 03	-22.89
			•	•		•		9.[illegible]1534E-02	5.[illegible]1437E-03	-2.[illegible]	2.[illegible]0069E 02	2.[illegible]1975E 01	-8.86
			•	•			•	1.[illegible]8[illegible]79E-01	3.[illegible]3079E-03	-12.[illegible]	8.[illegible]C536E 01	4.[illegible]2435E 00	-4.15
•					•			1.[illegible]1577E-01	3.[illegible]6[illegible]1E-[illegible]	-53.94	1.[illegible]4439E 08	1.[illegible]2472E 07	-46.91
	•				•	•		8.[illegible]5331E-01	2.[illegible]5[illegible]2E-04	-47.25	1.[illegible]4056E 07	1.[illegible]7453E 05	-34.65
	•				•		•	1.[illegible]6137E-01	2.[illegible]9717E-04	-27.85	1.[illegible]6339E 04	1.[illegible]0125E 05	-33.09
		•			•	•		1.[illegible]3[illegible]79E-02	4.[illegible]1416E-04	-42.99	3.[illegible]1860E 06	2.[illegible]4360E 04	-29.05
		•			•		•	5.[illegible]5449E-02	4.[illegible]8[illegible]42E-01	-18.74	6.[illegible]8383E 02	1.[illegible]2333E 04	-27.04
			•		•	•		5.[illegible]4[illegible]20E-02	1.[illegible]7[illegible]40E-03	-3.[illegible]2	3.[illegible]7C13E 04	9.[illegible]6071E 01	-12.03
			•		•		•	2.[illegible]2494E-03	2.[illegible]2494E-03	[illegible].[illegible]	9.[illegible]C913E-02	2.[illegible]2234E 01	-8.90

Figure 9: Typical page of computer print out.

Table 4

Specie	A ($\times 10^{-2}$)	B ($\times 10^{-4}$)	accuracy (kcal/mole)	source
H_2O (g)	-0.598	+1.364	0.01	JANAF[29]
HCl (g)	-0.227	-0.139	0.1	"
Cl (g)	+0.299	-0.437	2.0	"
$FeCl_3$ (g)	-0.640	+0.864	1.2	"
$FeCl_2$ (g)	-0.384	-0.639	2.0	"
Fe_2O_3 (s)	-1.930	+5.872	0.3	"
YCl_3 (g)	-2.240	+4.000	3.0	Smithells[32]
Y_2O_3 (s)	-4.559	+6.811	0.5	Ackermann et al.[33]

It should be noted that the data for Y_2O_3 (calculated by Ackermann et al.[33] from previous experimental data[34],[35] is substantially different from earlier data by Kelley[36] which was calculated from estimated heat capacities.

No data for YIG or $YFeO_3$ has been reported in the literature; however, the phase equilibrium for the system Fe_2O_3-FeO-$YFeO_3$ has been determined by Van Hook[37]. There are two invarient reactions in the system: a eutectic reaction in which oxide liquid is in equilibrium with YIG and iron oxide, and a peritectic reaction in which liquid and $YFeO_3$ are in equilibrium with YIG. If the thermodynamic characteristics of the liquid phase were known, it would be possible to calculate thermodynamic data for both YIG and $YFeO_3$ from Van Hook's results. Calculations which assume the liquid phase to be an ideal solution of Fe_2O_3, FeO, and Y_2O_3 liquids give free energies of formation for YIG and $YFeO_3$ above the "common tangent" value by approximately 15 and 20 kilocalories per mole, respectively. However, for an intermediate phase, such as YIG or $YFeO_3$, to be stable, its standard free energy of formation must by less than that for a mixture of the end components, Y_2O_3 and Fe_2O_3 (i.e., below the common tangent between the end components). Thus, the assumption of an ideal liquid solution is quite erroneous and results in data which contradict the basic criterion of phase stability.

A survey was undertaken of crystalline oxide systems with intermediate compounds for which thermodynamic data is known. It was found that the standard free energies of formation for the intermediate phases was typically only 1 to 10 kilocalories per mole below the common tangent value. Therefore, for the present calculations, data

5 and 3 kilocalories per mole below the common tangent values were arbitrarily selected for $YFeO_3$ and YIG, respectively:

$$\Delta G^\circ_F(YFeO_3, s) = -329{,}800 + 63.55\ T \left[\frac{kcal}{mole}\right]$$

$$\Delta G^\circ_F(Y_{.75}Fe_{1.25}O_3, s) = -295{,}700 + 62.42\ T \left[\frac{kcal}{mole}\right]$$

Results of Calculations. The calculated equilibrium gas compositions for Runs 16 and 27 are given in Table 5.

It should be noted that although $FeCl_3$ has a lower standard free energy of formation at 1200°C than $FeCl_2$, the dissociation reaction (4) is highly favored at the reduced pressure of about 2 Torr. The data in Table 5 indicates that the reaction is nearly complete. At atmospheric pressure, however, (all other conditions held constant) the dissociation only goes to about 25 percent of completion. Thus, for other iron garnet CVD systems [17],[19],[20] which vaporize solid $FeCl_2$ at atmospheric pressure, it is not a good assumption that $FeCl_2$ is the reacting gas. Instead, thermodynamics shows that $FeCl_3$ is the predominant iron chloride specie if there is excess chlorine (either added intentionally or the reaction product of previous deposition) present in the system.

The free energy changes for each of the CVD reactions for Runs 16 and 27 are plotted in Figures 10 and 11. The lines on these figures are for ease in relating the various data points and should not be construed to represent any sort of continuous function. Free energy changes for specific compositions only - Fe_2O_3, YIG, $YFeO_3$, and Y_2O_3 - are represented in the figures.

Computer calculations were made over a wide range for each of the system parameters. The plots for all of these calculations have

Table 5

Gas	Partial pressure (atm.) Run 16	Run 27
O_2	3.40×10^{-4}	4.79×10^{-4}
H_2O	1.60×10^{-4}	6.37×10^{-4}
$FeCl_3$	0.21×10^{-4}	0.08×10^{-4}
$FeCl_2$	5.84×10^{-4}	5.79×10^{-4}
YCl_3	1.48×10^{-4}	1.68×10^{-4}
HCl	10.07×10^{-4}	9.94×10^{-4}
Cl_2	6.37×10^{-6}	1.44×10^{-6}
Cl	6.71×10^{-6}	1.98×10^{-6}
H_2	3.10×10^{-9}	2.30×10^{-8}
He	8.85×10^{-4}	4.20×10^{-4}

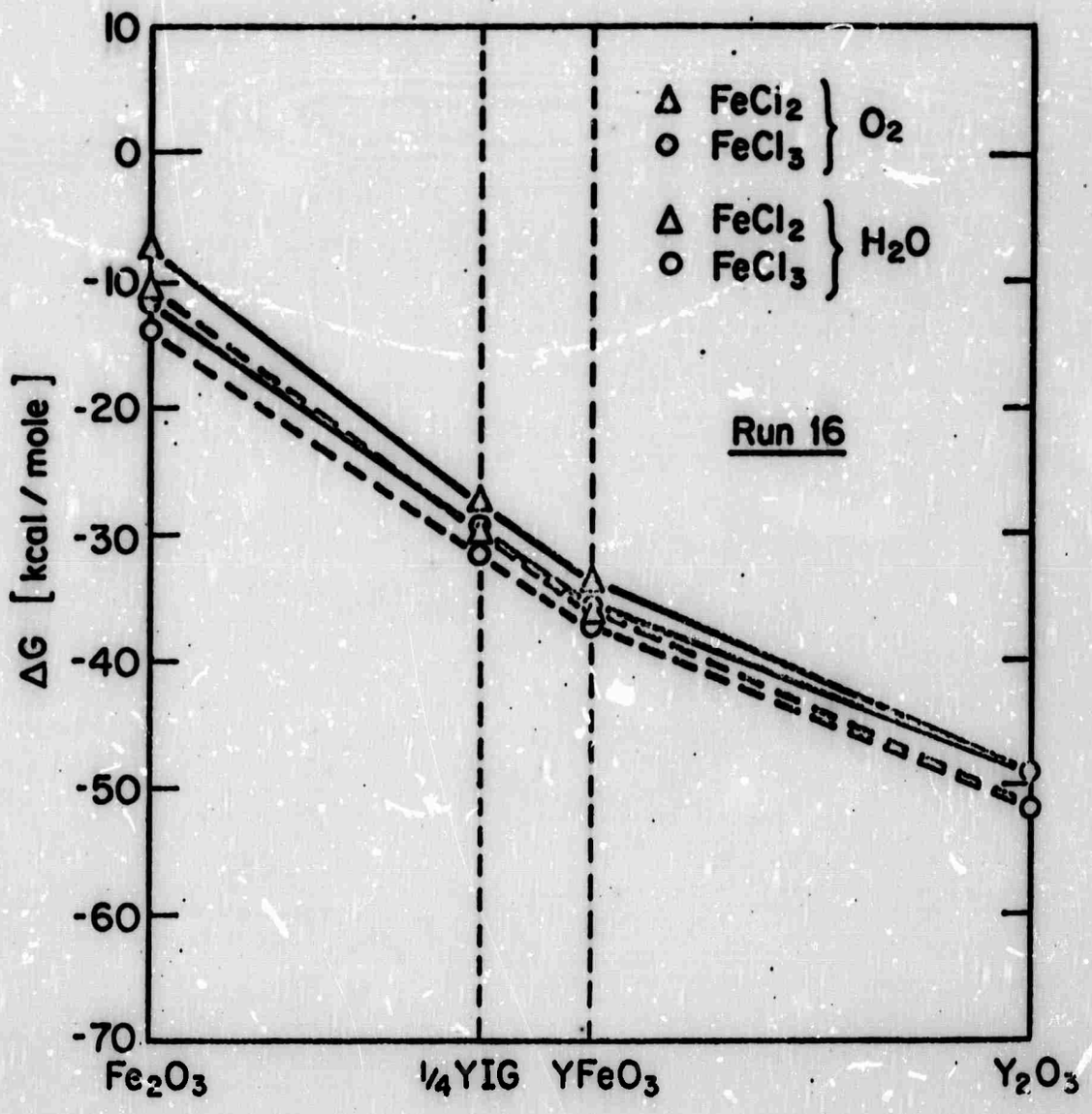

Figure 10: Calculated free energy changes for deposition of various phases - Run 16.

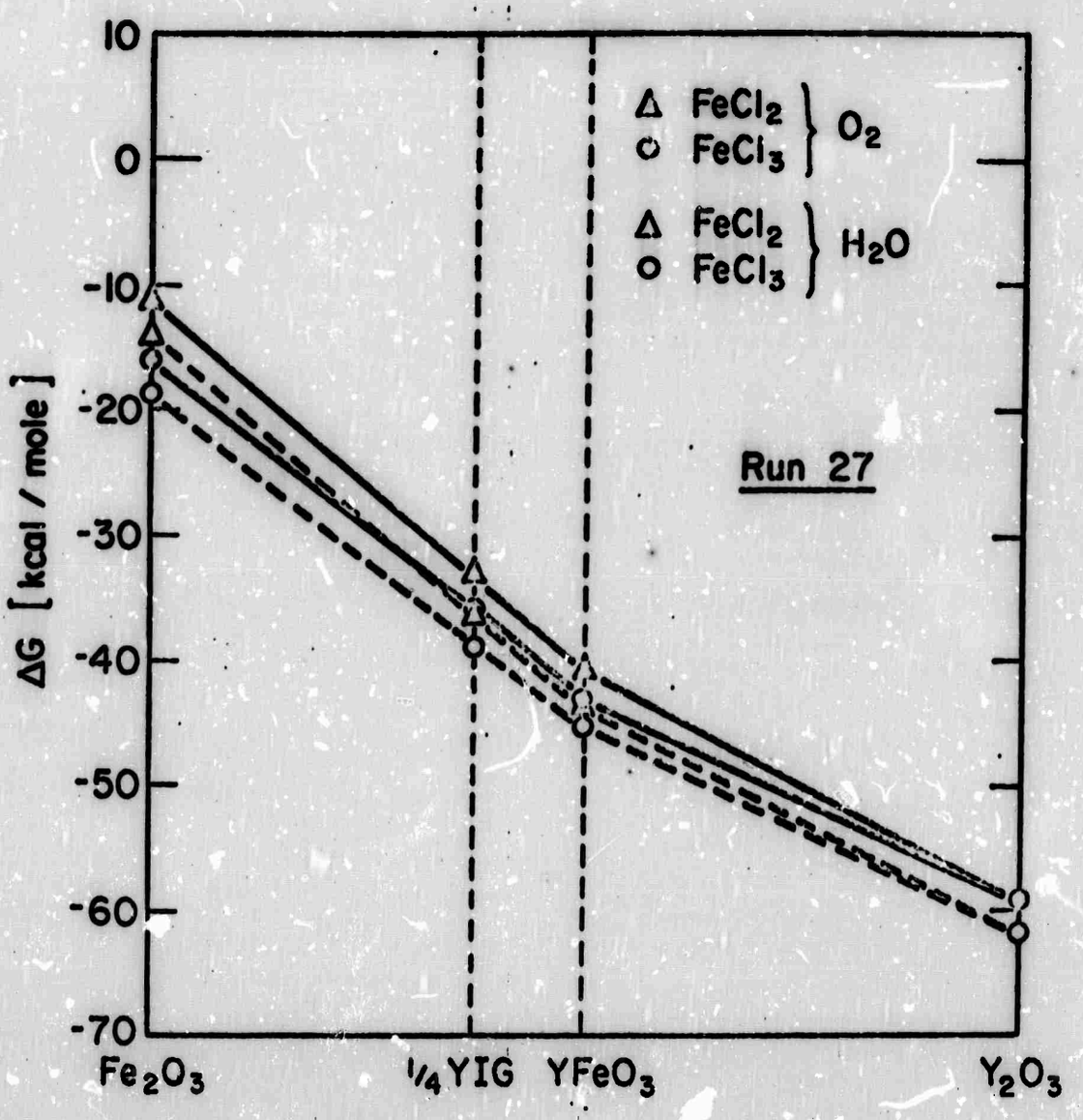

Figure 11: Calculated free energy changes for deposition of various phases - Run 27.

several features in common:

(1) The data for H_2O as the oxidizing gas is congruent with the data for O_2 and is displaced by only a few kilocalories per mole below it.

(2) The data for $FeCl_3$ as the reactant lies a few kilocalories per mole below that of $FeCl_2$, and the difference increases going towards Fe_2O_3 (See Figures 10 and 11).

(3) The largest free energy decrease is always associated with the deposition of Y_2O_3. The free energy changes become successively less negative for $YFeO_3$, YIG, and Fe_2O_3.

(4) The data for the intermediate compounds deviate from the Y_2O_3 - Fe_2O_3 common tangent by 3 and 5 kilocalories per mole for YIG and $YFeO_3$, respectively. This corresponds to the arbitrary negative deviation selected for the standard free energies of formation for these phases.

The effects upon the thermodynamic results due to changing various system parameters (temperature, total pressure, flow of excess chlorine, flow of hydrogen, ratio of iron chloride to yttrium chloride, ratio of chlorine bearing gases to oxygen bearing gas) are shown in Figures 12 through 17. The changes in the data for changing one growth parameter or ratio at a time are given with respect to the conditions (underscored) for Run 16. For simplicity, data is presented only for O_2 and $FeCl_3$ as reactant gases and Fe_2O_3 and Y_2O_3 as deposition products. However, it should be emphasized that each straight line represents a set of fourteen points similar to those in Figures 10 and 11.

Interpretation and Evaluation of Results. The thermodynamic effect of changing various system parameters can be catagorized in terms of a translation and/or a slope change of the ΔG data in Figures 12-17.

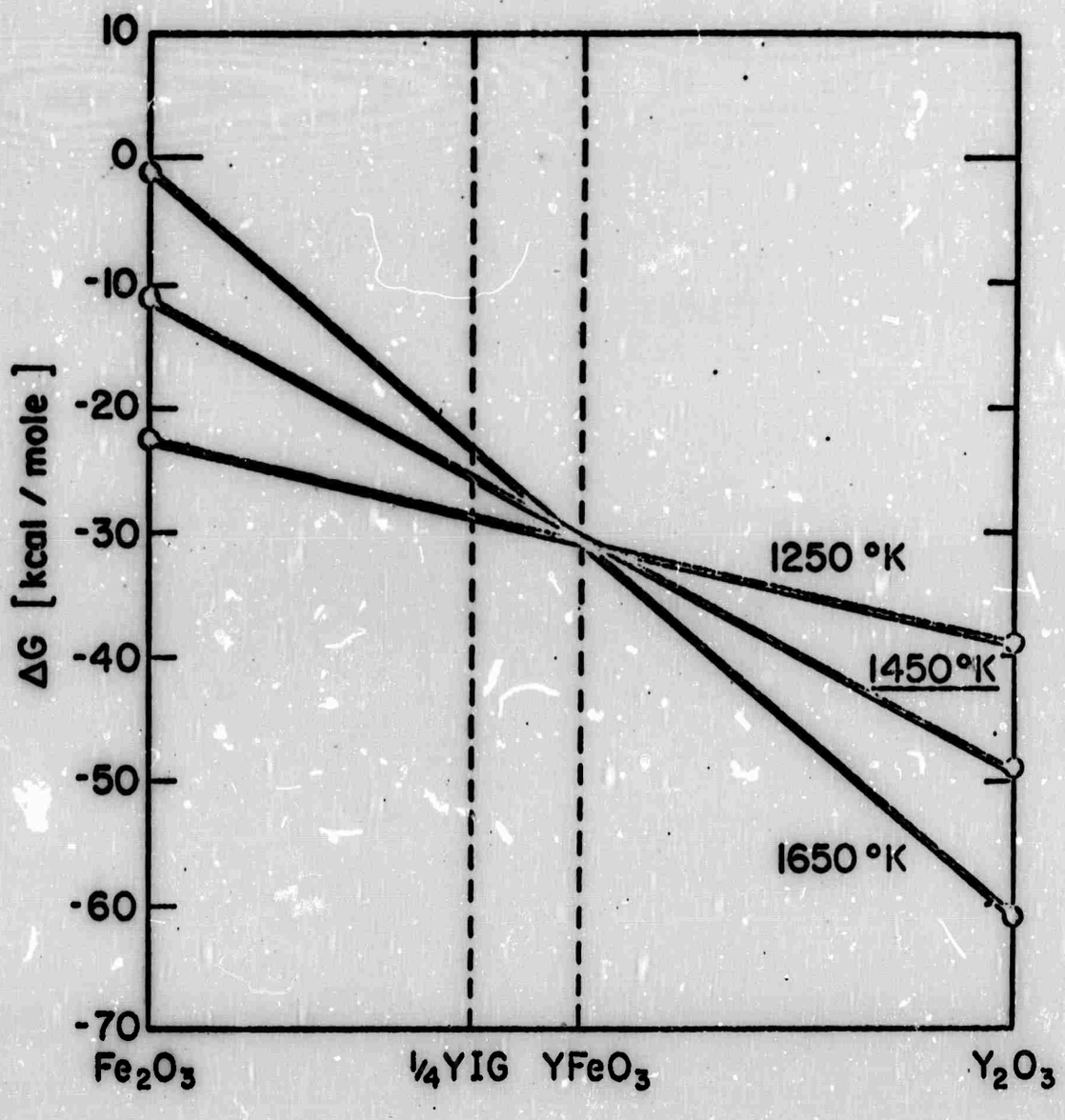

Figure 12: Calculated effect of changing temperature.

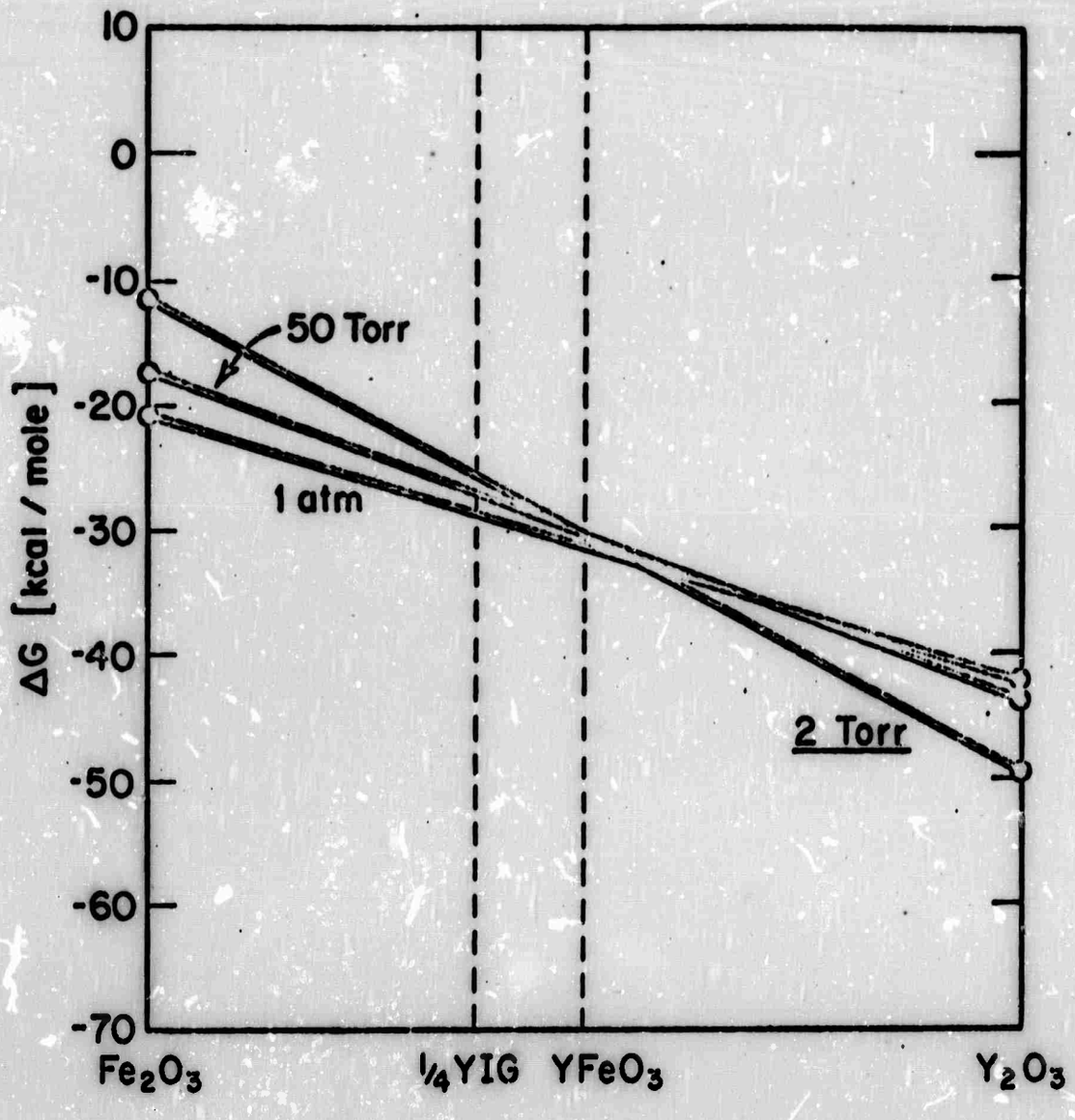

Figure 13: Calculated effect of changing <u>total pressure</u>.

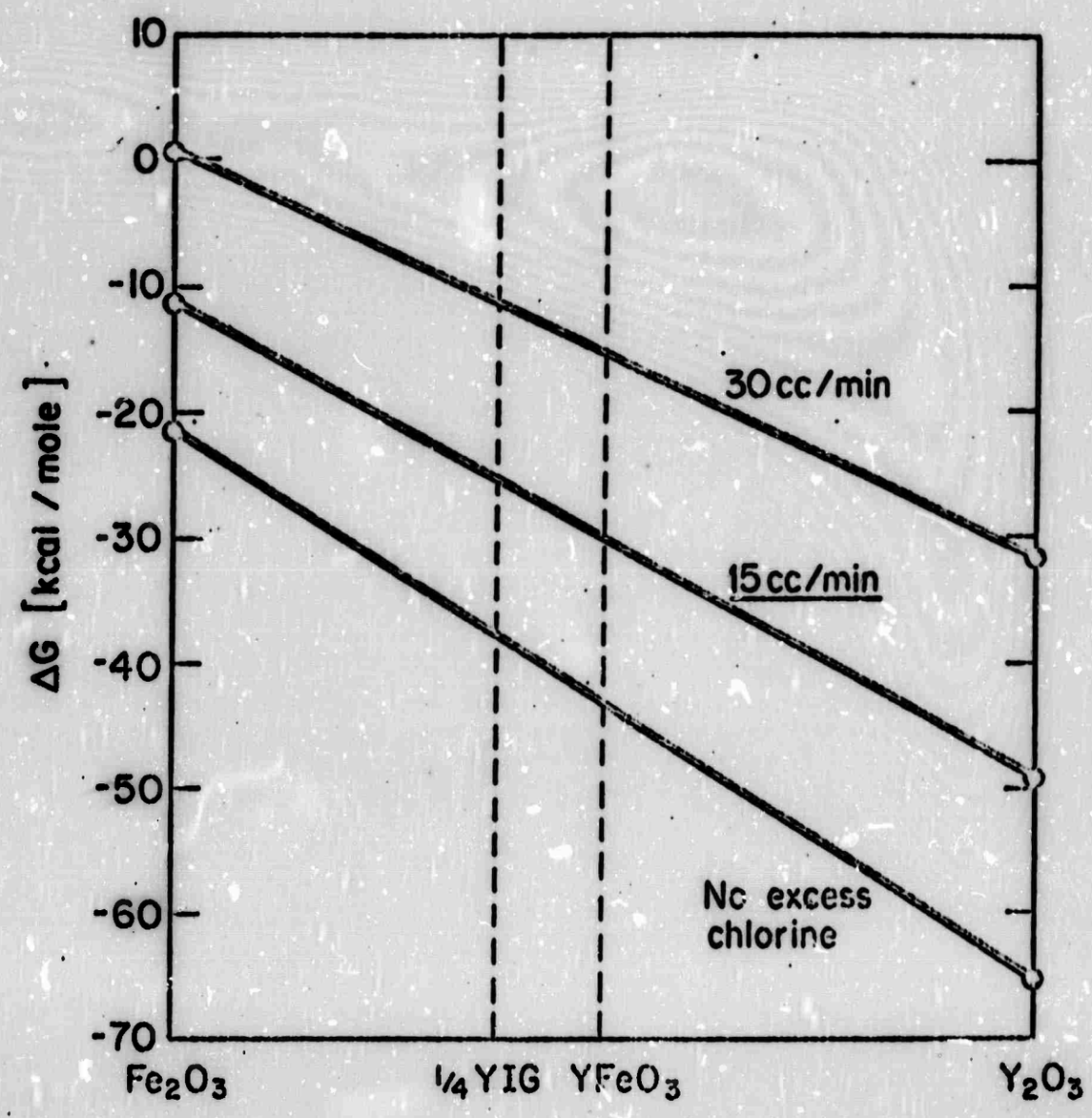

Figure 14: Calculated effect of changing flow of excess chlorine.

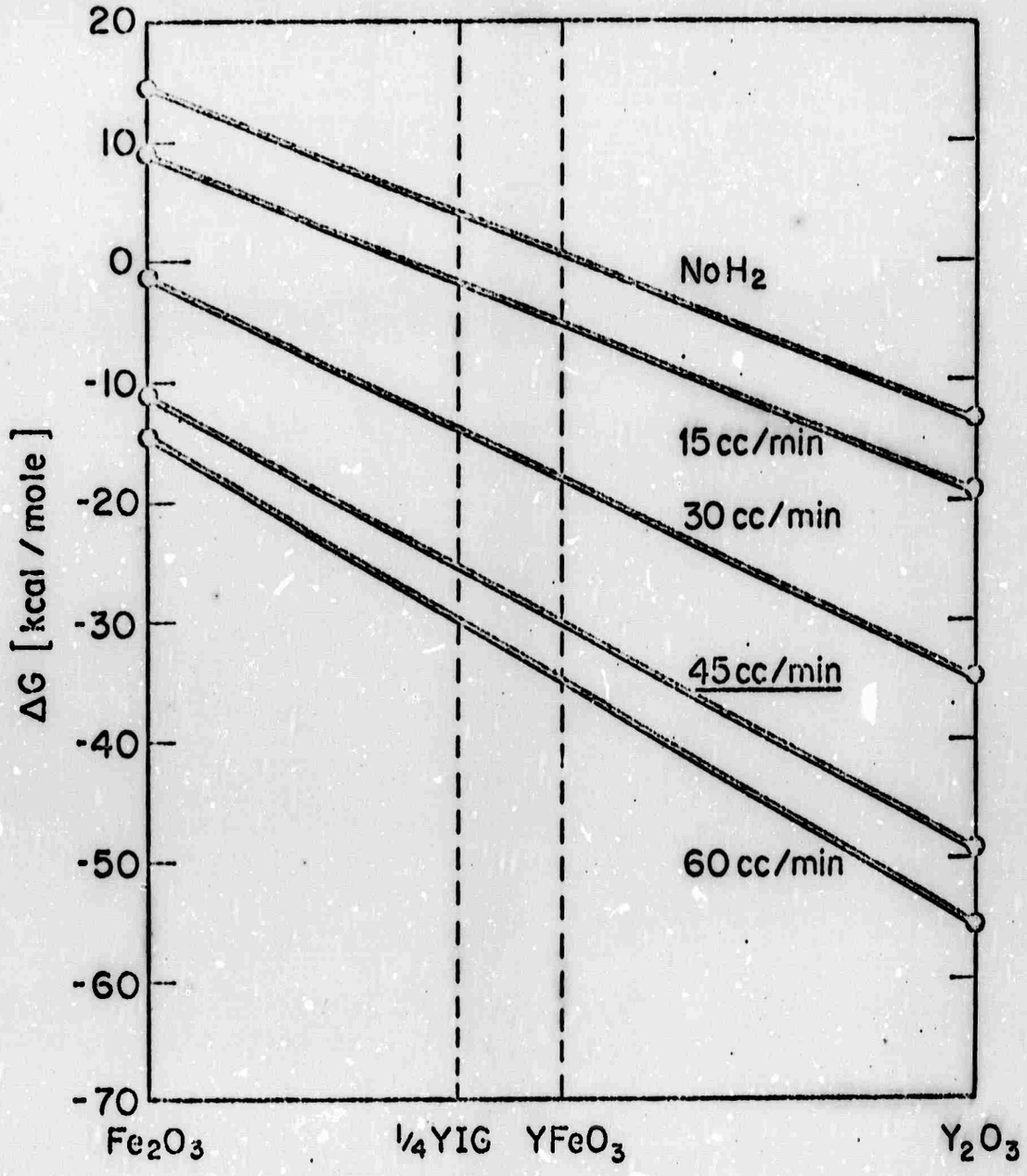

Figure 15: Calculated effect of changing flow of hydrogen.

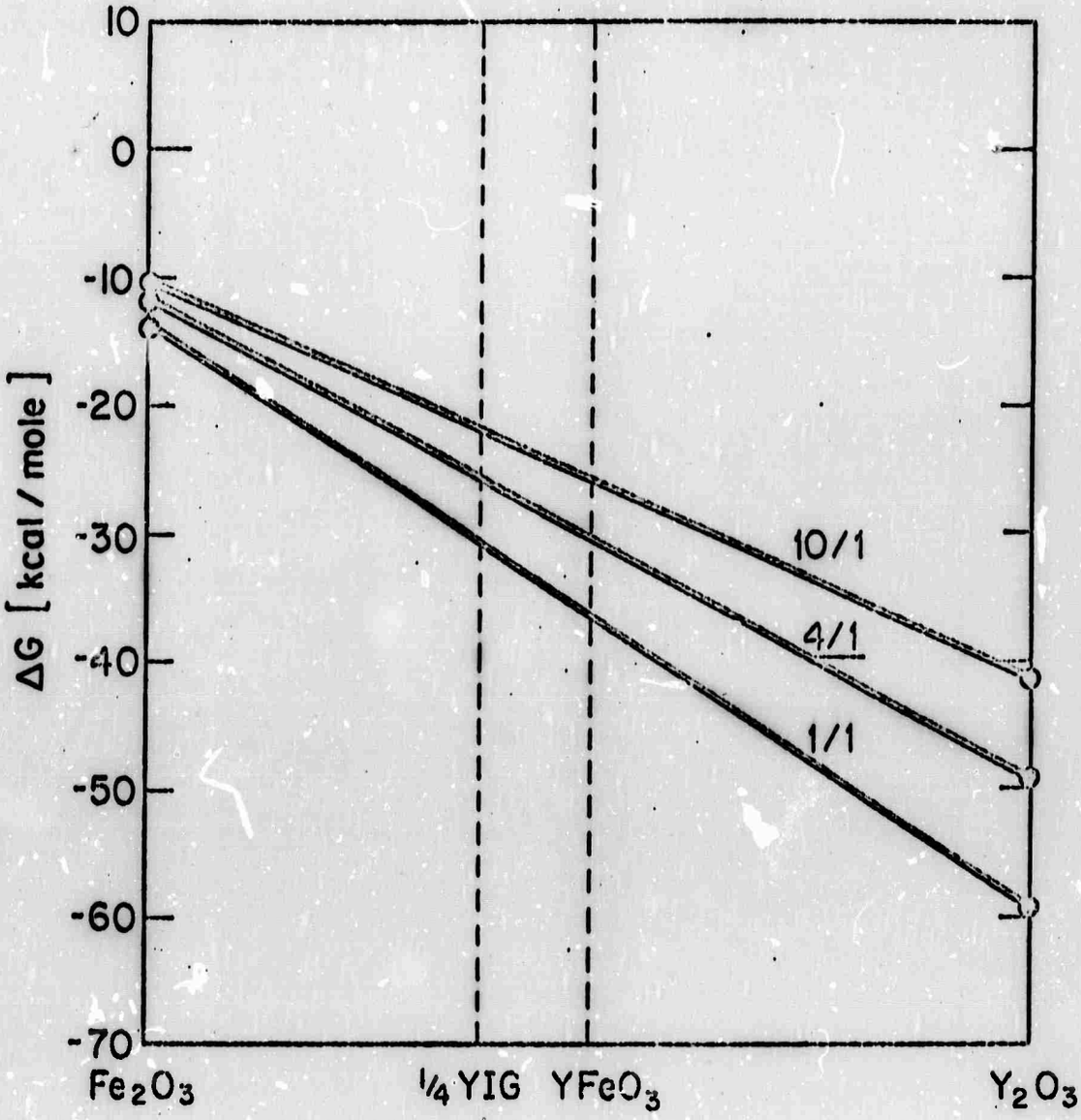

Figure 16: Calculated effect of changing ratio of iron chloride to yttrium chloride.

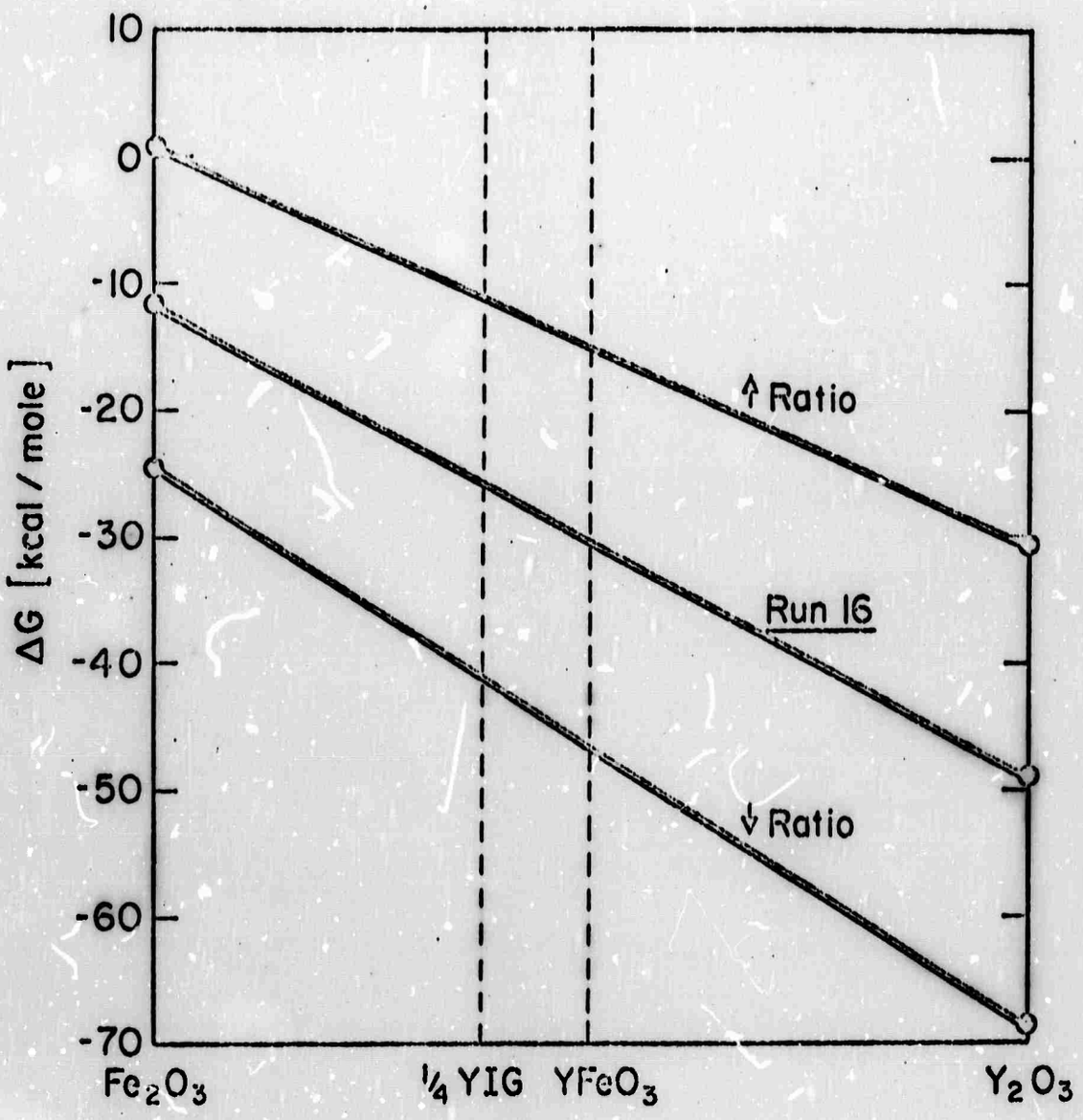

Figure 17: Calculated effect of changing ratio of chlorine bearing gases to oxygen bearing gases.

A translation corresponds to equal positive or negative shifts in the thermodynamic favorability of deposition for all of the phases. A slope change means that there are changes in the relative favorability of formation of the various phases. Temperature and system pressure changes cause slope changes, while the effect of changing the flow rates of hydrogen, excess chlorine, and the ratio of chlorine bearing gases to oxygen bearing gases is one of translation. Changing the ratio of iron chloride to yttrium chloride causes both a slope change and a translation; the favorability for the deposition of Fe_2O_3 is only slightly altered while that of Y_2O_3 is significantly changed.

There are some correlations between the predictions of the thermodynamic calculations and the observed results of the deposition runs (Section III):

(1) An increase in temperature decreases the driving force for the formation of YIG while that for $YFeO_3$ is unchanged. This agrees with the observation that $YFeO_3$ is deposited instead of YIG at higher temperatures.

(2) The general observation that yttrium containing phases appear most upstream in the deposition zone is supported by thermodynamic result that Y_2O_3 is the most favored phase with $YFeO_3$, YIG, and Fe_2O_3 being successively less favored.

(3) Eliminating the flow of hydrogen substantially reduces the amount of deposition, as is predicted by the thermodynamics.

However, certain observations are not predicted by the calculations:

(1) The calculated effect of total pressure does not predict a marked change in the driving force that would cause vapor phase nucleation to occur at 10 Torr but not at 2 Torr.

(2) The calculated effect of an increased flow of excess chlorine

is to decrease the overall amount of deposit without changing the relative favorability of deposition of the various phases. However, the observed effect is an increase in the amount of yttrium bearing phases without a significant change in the total amount of deposit.

The Effect of a Substrate. Even though the deposition of a solid phase may be favored thermodynamically, there is an activation energy barrier to nucleation. Thus, a certain minimum driving force is necessary for a phase to be deposited on a solid surface. However, it is likely that a clean and undamaged YAG or GGG substrate presents a surface with a very small activation barrier to the nucleation of YIG. If this is true, epitaxial YIG films can be deposited on garnet substrates with a smaller thermodynamic driving force (ΔG) than is necessary for polycrystalline deposition on a random surface. This is consistent with the observation that deposition rates for YIG single crystal films are significantly smaller than rates for polycrystalline YIG and other oxide phases.

Summary. Certain characteristics of the present YIG-CVD system can be explained thermodynamically. However, the system does not conform to all the assumptions necessary for the calculations. In particular, the non-ideality of the chlorination reactions and gas stream depletion effects due to heavy deposition near the gas input nozzles complicate matters considerably. In addition, accurate thermodynamic data for YIG and $YFeO_3$ is needed before the calculations can be further refined.

B. Kinetic Considerations

The behavior of a flowing system such as the present YIG-CVD system is strongly dependent upon its material transport characteristics. In the present system, gas molecules move both by forced convective flow and by diffusion.

(1) Forced Flow. The bulk velocity, V, of a gas stream flowing through a cylindrical tube is:

$$V = \frac{F}{A}$$

where: F = volumetric flow rate

A = cross-sectional area of tube

Assuming the gases to be ideal and for a given temperature, pressure, tube radius, and gas flow rate at standard temperature and pressure (S.T.P.):

$$V = 1.4 \times 10^{-2} \frac{TF}{PR^2} \qquad (7)$$

where: T = temperature ($^{\circ}$K)

F = total flow rate at S.T.P. (cm^3/min)

P = pressure (Torr)

R = tube radius (cm)

Using the system parameters for Run 16, the bulk gas velocity through the deposition zone is 167 centimeters per second. Temperature, total flow rate, and tube radius are approximately fixed for a given CVD system; however, pressure can vary widely. The gas velocity at 10 Torr would be reduced to 42 centimeters per second; at atmospheric pressure, the velocity would be only 0.55 centimeters per second.

For the gas velocity calculated for Run 16, for example, the residence time, τ, of a gas molecule in the deposition zone is only about 0.15 seconds. This short time cast doubt on the previous assumption that all the gases in the deposition zone are in equilibrium.

The relative gas velocities through the nozzles can also be determined. Although the overall gas flow is divided roughly equally between the

three concentric orifices (Section II), the cross-sectional area of the outer annulus through which oxygen flows is about twenty times greater than the areas of the middle and inner orifices. Thus, the oxygen velocity is much slower than that of the other input gases. The resulting velocity gradient present where the gas streams first contact each other is a probable source of the nozzle turbulence described in Section III.

For the present nozzle geometry, it would appear that turbulence will always be present unless the outer gas velocity is drastically increased. Robinson et al.[19] report a special nozzle design to insure laminar flow. On the other hand, the T-shaped furnace used by Mee et al.[17] appears to be designed to enhance gas mixing through turbulence.

The nature of the flow through the deposition zone farther downstream can be determined from the Reynolds number:

$$N_R = \frac{VR}{\nu}$$

where: ν = kinematic viscosity (cm^2/sec)

From the kinetic theory of gases:

$$\nu \approx \frac{1}{3}\bar{c}l$$

where: $\bar{c}$ = mean molecular velocity (cm/sec)

l = mean free path (cm)

From the Maxwell-Boltzman distribution:

$$\bar{c} = \left(\frac{8kT}{\pi m}\right)^{\frac{1}{2}}$$

where: m = mass of molecule.

The mean free path is:

$$l = \frac{1}{\Pi\sigma^2 n}$$

where: σ = scattering radius of molecule (cm)

n = molecules per unit volume (cm^{-3})

Assuming ideal gas behavior and $\sigma^2 = 3 \times 10^{-15} cm^2$:

$$\bar{c} = 1.45 \times 10^4 \left(\frac{T(^\circ K)}{M(g)}\right)^{\frac{1}{2}} \qquad (9)$$

$$l = 1.10 \times 10^{-5} \frac{T(^\circ K)}{P(Torr)} \qquad (10)$$

where: M = molecular weight of the gas.

Using the growth parameters from Run 16 with 47.2 as the average molecular weight (as calculated from the equilibrium gas composition):

$\bar{c} = 8.04 \times 10^4$ cm/sec

$l = 6.60 \times 10^{-3}$ cm

$\nu = 1.76 \times 10^2$ cm^2/sec

$N_R = 7.65$

For fluid flow through a cylindrical tube, laminar flow occurs for Reynolds numbers less than about 2000. Thus, laminar flow through the deposition zone is predicted once the nozzle turbulence has subsided. This is consistent with the observation of the second zone of uniform and relatively light deposition.

(2) Gas Diffusion. The kinetic theory of gases predicts that the diffusivity of a gas is approximately equal to its kinematic viscosity:

$$D = \alpha\nu \qquad (11)$$

where: α = constant ($1.2 < \alpha < 1.4$)

Taking $\alpha = 1.3$, the diffusivity of the gas phase for Run 16 is 2.29×10^2 cm^2/sec. Assuming:

$$x = \sqrt{Dt}$$

where: x = diffusion distance (cm)

t = diffusion time (sec)

the time for diffusion of gas from the center axis to the wall of the deposition zone is 0.033 seconds.

Combining the convective and diffusive transport (and ignoring nozzle turbulence), gas molecules entering along the center line of the deposition zone reach the wall via diffusion a distance downstream from the nozzles given by:

$$L^* = \frac{VR^2}{D} \qquad (12)$$

This expression is of the same form as one derived by Robinson and Wong[38]. Incorporation of equations

$$L^* = 0.2\ F\left(\frac{M}{T}\right)^{\frac{1}{2}} \qquad (13)$$

Therefore, if the present system were completely laminar, the gas molecules would reach the deposition zone wall 5.4 centimeters downstream from the nozzles.

It is at first surprising to note that the above expression is independent of both the system pressure and radius. However, pressure has exactly opposite effects upon V and D, and the R^2 factor in V cancels that in equation (12). Thus, equation (13) indicates that the gas transport characteristics in the deposition zone would be the same as those for a similar system operating at atmospheric pressure.

(3) Chemical Kinetics. If transport kinetics are rate controlling, the above discussion predicts equal deposition rates for atmospheric and reduced pressure systems. However, transport in CVD systems is rate limiting usually only at "high" temperatures. At lower temperatures, rates are controlled by a chemical raction[39],[40],[41].

Assuming that the present system operates in the "lower" temperature range where chemical kinetics are controlling, the deposition rate becomes dependent upon the gas phase residence time in the deposition zone. The residence time is:

$$\tau = \frac{L}{V}$$

where: l = length of the constant temperature deposition zone (cm).
In terms of the system parameters:

$$\tau = 71.5 \frac{PLR^2}{TF} \qquad (14)$$

In the present system, pressure is the only parameter in equation (14) which can vary widely. A critical residence time (and, thus, a critical system pressure) exists for which chemical equilibrium is just attained and the maximum deposition rate allowed by the chemical kinetics is reached. For shorter residence times (lower pressures), a lower deposition rate is expected. Equivalently, the effective chemical driving force for the CVD reactions is reduced for high gas velocities.

The decreased effective driving force at 2 Torr relative to that at 10 Torr is consistent with the absence of vapor phase nucleation at the lower pressure. The higher deposition rates reported in other garnet CVD systems[17],[19],[20] can similarly be explained. In these atmospheric pressure systems, residence times are estimated to be approximately two orders of magnitude longer than in the present system.

The effect of the high gas velocity at reduced pressure appears to be a tendency to "spread out" the deposition. Thus, if the deposition zone were very long, the total amount of deposition at reduced pressure would be equal to that deposited more heavily over a shorter distance at atmospheric pressure. The observation that only a small fraction of the generated chlorides are deposited as oxides in the present system is consistent with the reduced effective driving force for the deposition. If the high temperature region of the furnace were longer, more of the chlorides would be expected to react and deposit.

Although the lower deposition rate at reduced pressure will require longer run times to produce films of a given thickness, low pressure systems would be expected to have both longer garnet deposition zones and more uniform deposition rates over a given distance of the zone. The atmospheric pressure CVD systems[17],[19],[20] all report substantial gradients in deposition rates along the deposition zone. Thus, if film thickness is to be carefully controlled, a low pressure, high velocity system would potentially yield more uniform deposition rates.

V. SUMMARY AND CONCLUSIONS

Epitaxial single crystal YIG films have been successfully grown on YAG and GGG substrates by chemical vapor deposition at about 1200° C and 2.5 Torr. The films on GGG are crack-free and of good quality as evidenced by ferromagnetic resonance linewidths in the range of less than one to a few oersteds and by very uniform domain patterns. Measured lattice parameters of the films are approximately 0.03 percent smaller than the literature value for YIG.

Films up to 2.4 microns thick were achieved with deposition rates of approximately one micron per hour. The surface condition of the films is directly determined by that of the substrate.

Computer-aided thermodynamic calculations of the equilibrium gas composition in the system and of the free energy changes for the deposition of the various possible oxides were made. Certain characteristics of the deposition in the system can be explained by the results of these calculations.

The observation of vapor phase nucleation at 10 Torr but not at 2 Torr is thought to be due to the lower gas velocity - and, therefore, higher effective driving force - at the higher pressure. Similarly, the lower rates of deposition observed in the present system relative to systems operating at atmospheric pressure is believed to be due to the significantly higher gas velocity through the deposition zone in the present case.

Improvement of the yttrium chlorination process is necessary before films can be grown more repeatably and to greater thicknesses.

If optimized, the present reduced pressure, direct chlorination CVD system will have certain advantages over other systems reported in the

literature. Direct control of the chloride transport rates and more uniform growth rates along the deposition zone are potentially available with the present system.

VI. SUGGESTIONS FOR FUTURE WORK

System Improvements. Before the present CVD system can be optimized, it is necessary to improve the yttrium chlorination process to prevent oxidation of the metal. For envisioned future work, a constant rate of chloride generation for several hours and perhaps several days will be required. Suggested possible methods for preventing the oxidation are (1) a flow of hydrogen or some other reducing gas in addition to chlorine through the chlorinator tube and (2) further increased flow of inert gas through the chlorinator in order to increase the total gas velocity and thus prevent back diffusion.

A longer constant temperature deposition zone is suggested for studying the deposition characteristics over a greater distance.

Parameter Optimization. More work is necessary to optimize the crystal growth conditions, first, in order to produce films repeatably and then to optimize the parameters with respect to crystal quality. More detailed characterization of the deposited films will be required for the latter.

Future Research. Some of the potential applications of epitaxial YIG require films tens of microns thick or even bulk single crystals of centimeter size. Other applications call for doped YIG films and bulk crystals and materials with controlled property (and, therefore, composition) gradients. In all cases, materials of high purity and quality are required.

The materials described above potentially can be grown by CVD at reduced pressure.

VII. REFERENCES

1. S. Geller and M. A. Gilleo, Acta Cryst. 10 (1957) 787
2. F. Bertaut and R. Pauthenet, Proc. I.E.E. B104 (1957) 261
3. G. R. Harrison and L. R. Hodges, Jr., J. Am. Ceram. Soc. 44 (1961) 214
4. L. K. Shick et al., Appl. Phys. Letters 18 (1971) 89
5. L. G. Van Uitert et al., Mat. Res. Bull. 5 (1970) 825
6. E. G. Spencer, R. L. LeCraw, and C. S. Porter, J. Appl. Phys. 29 (1958) 429
7. B. Lax and K. J. Button, Microwave Ferrites and Ferrimagnets, McGraw Hill (1962) 540
8. R. L. Comstock and C. E. Fay, J. Appl. Phys. 36 (1965) 1253
9. E. Stern, IEEE Trans. MTT-17 (1969) 835
10. F. A. Pizzarello, J. H. Collins, and L. E. Coarver, J. Appl. Phys. 41 (1970) 1016
11. A. H. Bobeck, Bell Sys. Tech. J. 46 (1967) 1901
12. C. F. Powell, in Vapor Deposition (C. F. Powell, J. H. Oxley, and J. M. Blocher, Jr., eds.), Wiley & Sons (1966) 249
13. R. C. Linares and R. B. McGraw, Jr., J. Appl. Phys. 35 (1964) 3630
14. R. C. Linares, R. B. McGraw, and J. B. Schroeder, J. Appl. Phys. 36 (1965) 2884
15. J. E. Mee et al., Appl. Phys. Letters 10 (1967) 289
16. M. Sparks et al., J. Appl. Phys. 40 (1969) 1518
17. J. E. Mee et al., IEEE Trans. MAG-5 (1969) 717
18. S. Geller, G. P. Espinosa, and P. B. Crandall, J. Appl. Cryst. 2 (1969) 86
19. McD. Robinson, A. H. Bobeck, and J. W. Nielson, submitted to IEEE Trans. MAG

20. B. F. Stein, J. Appl. Phys. 41 (1970) 1262

21. P. S. Schaffer, J. Am. Ceram. Soc. 48 (1965) 508

22. C. G. Fonstad, A. Linz, and R. H. Rediker, J. Electrochem. Soc. 116 (1969) 1269

23. J. E. Mee, IEEE Trans. MAG-3 (1967) 190

24. J. Easterfield, Brit. J. Appl. Phys. (J. Phys. D) 2 (1969) 1159

25. L. K. Shick, J. Electrochem. Soc. 118 (1971) 179

26. R. Aeschlimann, F. Gassmann, and T. P. Woodman, Mat. Res. Bull. 5 (1970) 167

27. A. E. Feuersanger, Solid State Design 4:10 (1963) 29

28. J. F. Dillon, Jr., J. Appl. Phys. 31 (1960) 1605

29. JANAF Thermochemical Tables, Dow Chemical Co., Midland, Mich., 1965

30. J. L. Moriarty, J. Chem. Eng. Data 8 (1963) 422

31. G. W. Westley, ZEROIN, 1969

32. C. J. Smithells, Metals Reference Book, 4th Ed., Plenum Press (1967) 244

33. R. J. Ackermann, E. G. Rauh, and R. J. Thorn, J. Chem. Phys. 40 (1964) 883

34. E. J. Huber, Jr., C. E. Holley, Jr., and E. L. Head, J. Phys. Chem. 61 (1957) 497

35. H. W. Goldstein et al., J. Phys. Chem. 63 (1959) 1445

36. K. K. Kelley, U. S. Bureau of Mines, Bulletin 542, 1954

37. H. J. Van Hook, J. Am Ceram. Soc. 45 (1962) 162

38. McD. Robinson and P. Wong, Proc. Second Int. Conf. on Chemical Vapor Deposition, May 1970, 127

39. E. G. Sylander, J. Electrochem. Soc. 109 (1962) 1121

40. McD. Robinson, ScD. Thesis, MIT, 1967

41. R. N. Ghoshtagore, J. Electrochem. Soc. 117 (1970) 529

PROPAGATION OF MAGNETOSTATIC SURFACE SPIN WAVES IN YIG SLABS

by

Jen K. Jao

The material which follows is identical in content to a thesis submitted to the Department of Electrical Engineering on May 14, 1971 in partial fulfillment of the requirement for the Degree of Master of Science.

TABLE OF CONTENTS

INTRODUCTION

Since the discovery of a high quality ferrite material yttrium iron garnet (YIG) over ten years ago, Magnetostatic modes have been investigated theoretically and experimentally. Devices such as YIG delay lines utilizing magnetostatic waves have been successfully constructed. It has also been proved that magnetostatic waves can serve as a bridge providing coupling between electromagnetic power and exchange and magnetoelastic powers[1].

Damon and Eshbach solved the problem of magnetostatic modes in a ferrite slab[2,3] ten years ago. Surface modes were predicted. Current interest in surface wave technology makes it advisable to revaluate their results.

Nonreciprocal magnetostatic surface waves have been observed propagating in YIG slabs and epitaxial thin films[4,5]. In these experiments the magnetic field is applied parallel to the slab surface and orthogonal to the wave vector.

In addition to the unique nonreciprocal property of magnetostatic surface waves, Morgenthaler predicted that independently controllable propagation and decay constant would be attainable if the magnetic field is tilted away from the ferrite surface[6,7]. It appears possible to switch the surface wave propagating along one slab surface to the other by properly switching the bias magnetic field direction[6,7]. Due to these novel properties of surface waves potential planar devices such as isolators, switches, etc., may be realizable at microwave frequencies.

In this thesis, we present detailed theoretical and experimental knowledge about magnetostatic surface waves as well as a systematic

method of approach to such problems.

Chapter I is a brief review of magnetostatic spin waves in an infinite ferrite medium. Small signal equations of motion are stated and solved in a medium biased by uniform DC magnetic field. Quasi-normal modes are then used to discuss wave propagation in temporally or spatially non-uniform medium[8,9,10]. All concepts and techniques used in this chapter prove to be essential to the understanding of surface waves. As a matter of fact, they usually can be carried straight through to the latter case.

Chapter 2 is devoted to the study properties of surface modes. We start from a semi-infinite ferrite medium and then consider a slab of finite thickness. Normal modes are analyzed in detail by diagonalizing the torque equation when only the dipolar field is present, but the results can be easily generalized to include other rf magnetic fields. Finally, switching of surface modes is discussed in terms of normal modes and the dispersion relation.

Chapter 3 is a report on our experimental results conducted on YIG slabs. A surface wave pulse at microwave frequencies is excited and detected using fine wire antenna when the DC magnetic field is biased to operate in the magnetostatic region but is in a general direction transverse to the wave propagation direction. Data collected are then correlated with the theoretical predictions.

CHAPTER I

MAGNETOSTATIC SPIN WAVES IN INFINITE FERRITE MEDIUM

Owing to the efforts of many pioneer workers in the last decade, a lot of information on volume magnetostatic spin waves has already been complied. In this chapter only that portion relevant to the understanding of magnetostatic surface waves will be reviewed. Our discussion starts from the plane wave solution of the linearized equations of motion for the infinite ferrite medium and is followed by the method of normal modes treating the problem of magnetostatic spin waves. The last section, summarizes the important experimental literature.

Exchange interaction of spin waves is here only briefly discussed and magnetoelastic interactions are not included at all. The interested reader is referred to many other excellent review articles[11,12].

1.1 Small Signal Equations of Motion

In a lossless saturated ferromagnetic insulator, the motion of the magnetization vector is described by a set of small signal equations of motion governing interactions between the electromagnetic and spin system.

For the electromagnetic system, Maxwell's equations are

$$\nabla \times \vec{h} = \epsilon \frac{\partial \vec{e}}{\partial t} \tag{1.1a}$$

$$\nabla \times \vec{e} = -\mu_0 \frac{\partial}{\partial t}(\vec{h} + \vec{m}) \tag{1.1b}$$

$$\nabla \cdot (\vec{h} + \vec{m}) = 0 \tag{1.1c}$$

$$\nabla \cdot (\epsilon \vec{e}) = 0 \tag{1.1d}$$

For the spin system, the large signal torque density equation is of the form

$$\frac{\partial \bar{M}}{\partial t} = \gamma \mu_0 \bar{M} \times \bar{H} \tag{1.2}$$

The torque equation, when linearized, becomes

$$\frac{\partial \bar{m}}{\partial t} = -\omega_m \hat{i}_z \times \left(-\frac{H_i}{M} \bar{m} + \bar{h} + \bar{h}' \right) \tag{1.3}$$

where $\bar{M} = M_z \hat{i}_z + \bar{m}$, $\bar{H} = H_z \hat{i}_z + \bar{h} + \bar{h}'$, $\bar{m}$ is the small transverse component of $\bar{M}$ ($\bar{m} \cdot \bar{M}_z = 0$), $\bar{H}$ the total internal magnetic field, $\bar{h}$ the Maxwellian rf field and the vector $\bar{h}'$ is the total effective rf field arising from magnetic anisotropy $\bar{h}^{an}$, exchange $\bar{h}^{ex} = \lambda \nabla^2 \bar{m}$ (λ is the exchange constant), and anything else. For simplicity we neglect the anisotropy fields here. To simplify notation we define

$$H_i = H_0 - N_z M \tag{1.4}$$

and

$$\omega_m = -\gamma \mu_0 M \tag{1.5}$$

where

N_z is the appropriate demagnetizing factor arising from the surface dipolar magnetic field

and

γ is the gyromagnetic ratio (negative for electrons).

1.2 Plane Wave Solution In Infinite Ferrite Medium

Unless otherwise explicitely stated we assume the ferrite sample under discussion is biased with a DC magnetic field uniform spatially as well as temporally. In such a medium, the general solution of field quantities will be the superposition of many plane waves each with a different frequency ω and wave number k. The relation between ω and k

is termed the dispersion relation. For a single wave component, we have

$$\bar{h}(r,t) = \mathrm{Re}\left[\underline{h}\exp j(\omega t - \bar{k}\cdot\bar{r})\right] \tag{1.6a}$$

$$\bar{m}(r,t) = \mathrm{Re}\left[\underline{m}\exp j(\omega t - \bar{k}\cdot\bar{r})\right] \tag{1.6b}$$

$$\bar{e}(r,t) = \mathrm{Re}\left[\underline{e}\exp j(\omega t - \bar{k}\cdot\bar{r})\right] \tag{1.6c}$$

$\underline{h}$, $\underline{m}$, $\underline{e}$ are complex vector fields satisfying

$$j\bar{k}\times\underline{h} = -j\omega\epsilon\underline{e} \tag{1.7a}$$

$$j\bar{k}\times\underline{e} = j\omega\mu_0(\underline{h}+\underline{m}) \tag{1.7b}$$

$$\bar{k}\cdot(\underline{h}+\underline{m}) = 0 \tag{1.7c}$$

$$\bar{k}\cdot\epsilon\underline{e} = 0 \tag{1.7d}$$

and

$$\underline{m} = \underline{\underline{\chi}}\cdot\underline{h} \tag{1.8a}$$

$$\underline{\underline{\chi}} = \begin{bmatrix} \chi & -j\kappa & 0 \\ j\kappa & \chi & 0 \\ 0 & 0 & 0 \end{bmatrix} \tag{1.8b}$$

where

$$\chi = \frac{\omega_r\,\omega_m}{\omega_r^2-\omega^2} \tag{1.9a}$$

$$\kappa = \frac{-\omega\,\omega_m}{\omega_r^2-\omega^2} \tag{1.9b}$$

$$\omega_r = \omega_0^2 + \lambda k^2 \tag{1.10a}$$

$$\omega_0 = -\gamma\mu_0 H_i \tag{1.10b}$$

Define $k_0^2 = \omega^2\epsilon\mu_0$, then combine equations (1.7) and (1.8) we get

$$k^2\underline{h} - \bar{k}(\bar{k}\cdot\underline{h}) - k_0^2(\underline{\underline{1}}+\underline{\underline{\chi}})\cdot\underline{h} = 0 \tag{1.11}$$

which gives the dispersion

$$\frac{K^2}{K_0^2} = \frac{[\chi(\chi+1) - \kappa^2] + 2(\chi+1) \pm \{[\chi(\chi+1) - \kappa^2]^2 \sin^4\psi + 4\kappa^2\cos^2\psi\}^{1/2}}{2(\chi \sin^2\psi + 1)} \quad (1.12)$$

where ψ is the propagation angle with respect to z axis.

$$\sin^2\psi = \frac{K_x^2 + K_y^2}{K^2}$$

Equation (1.12) is plotted in Fig. (1.1). The dashed curve is the solution for ordinary wave where the rf $\bar{h}$ field is parallel to $\bar{M}$, and the solid curve is for extraordinary wave where the rf $\bar{h}$ field is prependicular to $\bar{M}$.

1.3 Magnetostatic Approximation

It has been shown that when $K \gg K_0$ or $K \ll K_0$ solutions of (1.7) approximately statisfy $\nabla \times \bar{h} = 0$ and give rise to an electric field $\bar{e}$ of higher order than $\bar{h}$[13]. In such regions of k this so called magnetostatic approximation is a very good one. Inclusion of the exchange interaction may or may not be required, depending on the wave number of interest. In addition, if the ferrite sample considered is comparable to the wavelength of the magnetostatic wave, boundary conditions may modify the dispersion drastically. Boundary conditions in the absence of the exchange interaction are the ordinary Maxwellian conditions requiring continuities of the normal component of magnetic flux and tangential components of magnetic fields. The exchange boundary condition is discussed in reference[14].

In the magnetostatic approximation, equations (1.1) reduce to

$$\bar{e} = 0 \quad (1.13a)$$

$$\nabla \times \bar{h} = 0 \quad (1.13b)$$

$$\nabla \cdot \bar{b} = -\nabla \cdot \bar{m} \quad (1.13c)$$

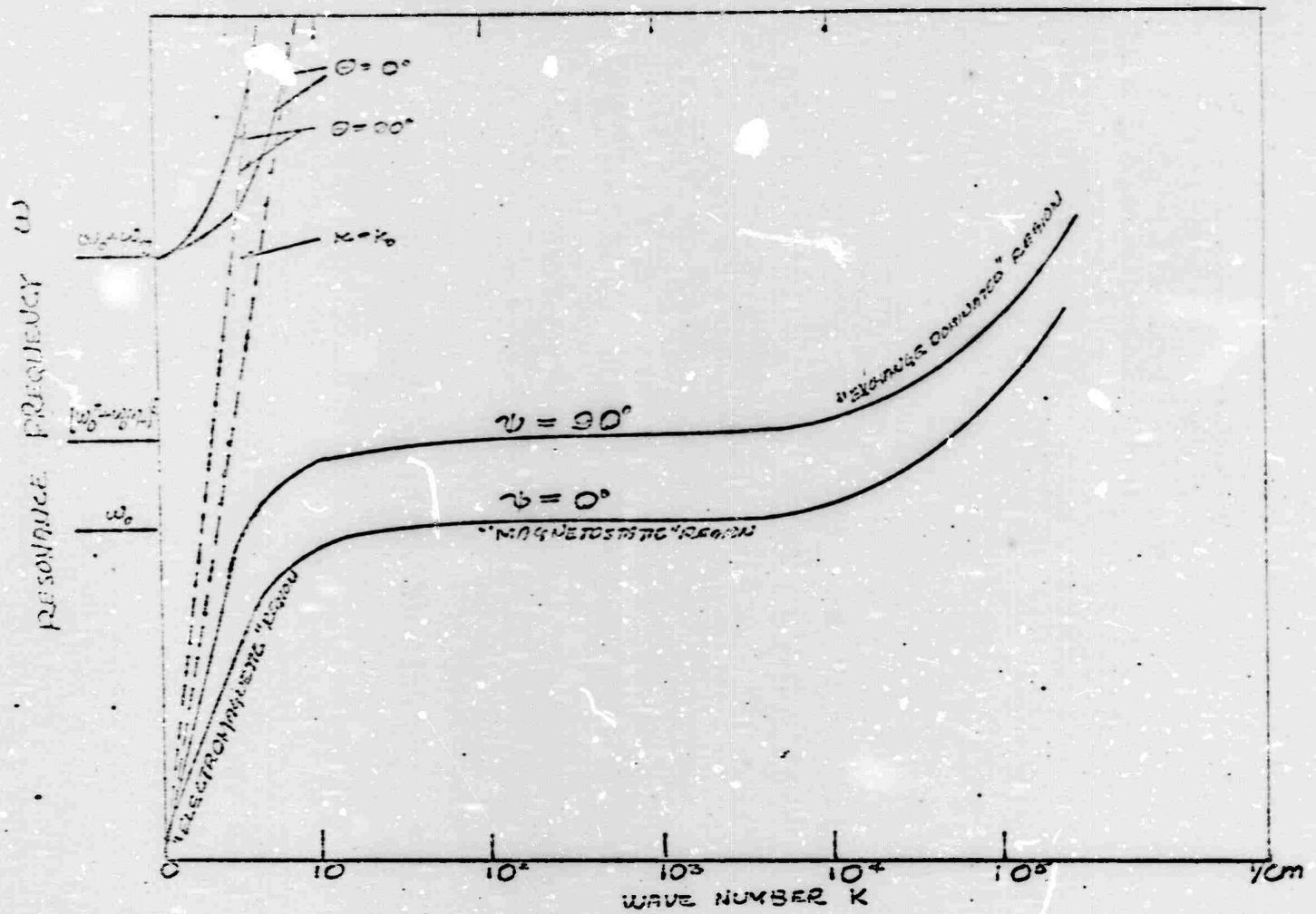

Fig. 1.1 Dispersion relation of spin waves in infinite ferrite medium

and $$\nabla \times \vec{e}_1 = -\mu_0 \frac{\partial}{\partial t}(\vec{h} + \vec{m}) \tag{1.13d}$$

$$\nabla \cdot \vec{e}_1 = 0 \tag{1.13e}$$

Equation (1.13b), when integrated, gives

$$\vec{h} = \nabla \phi \tag{1.14}$$

Together, Eqs. (1.8) and (1.13c) yield Walker's equation for the potential.

In the following section, magnetostatic wave solutions are obtained directly by solving the torque equation. This approach, the author believes, is more illuminating physically and allows convenient generalization.

1.4 Normal Modes of Magnetostatic Waves

In the magnetostatic approximation, a particular solution of the dipolar field $\vec{h}$ is evidently

$$\vec{h} = -\vec{k}\left(\frac{\vec{m}\cdot\vec{k}}{k^2}\right) \tag{1.15}$$

Together with the exchange field

$$\vec{h}^{ex} = -\lambda \omega_m k^2 \vec{m} \tag{1.16}$$

they constitute the total rf field for our purpose, because the homogeneous solution drops out in a infinite ferrite medium.

For mathematical simplicity but without losing generality, the coordinate system used in this section is shown below

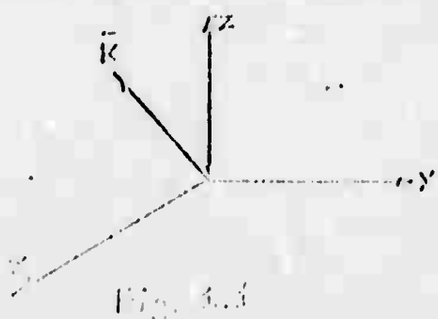

Fig. 1.1

With this choice, equation (1.3) becomes

$$\begin{bmatrix} \dot{m}_x \\ \dot{m}_y \end{bmatrix} = \begin{bmatrix} 0 & , & \omega_r \\ \omega_r + \omega_m \sin^2\varphi & , & 0 \end{bmatrix} \cdot \begin{bmatrix} m_x \\ m_y \end{bmatrix} \tag{1.17}$$

upon substitution of Eqns. (1.15) and (1.16)

To diagonalize Eq. (1.17), we define

$$\begin{bmatrix} m^+ \\ m^- \end{bmatrix} = \begin{bmatrix} 1 & , & j\frac{1}{e_k} \\ 1 & , & -j\frac{1}{e_k} \end{bmatrix} \cdot \begin{bmatrix} m_x \\ m_y \end{bmatrix} \tag{1.18}$$

Thus

$$\begin{bmatrix} m_x \\ m_y \end{bmatrix} = \begin{bmatrix} \frac{1}{2} & , & -\frac{1}{2} \\ -\frac{e_k}{2} & , & \frac{e_k}{2} \end{bmatrix} \cdot \begin{bmatrix} m^+ \\ m^- \end{bmatrix} \tag{1.19}$$

After substituting (1.19) into (1.17) we get

$$\begin{bmatrix} \dot{m}^+ \\ \dot{m}^- \end{bmatrix} = \begin{bmatrix} j\omega_k & , & 0 \\ 0 & , & -j\omega_k \end{bmatrix} \cdot \begin{bmatrix} m^+ \\ m^- \end{bmatrix} \tag{1.20}$$

where

$$e_k = \left(\frac{\omega_r + \omega_m \sin^2\varphi}{\omega_r} \right)^{1/2} \tag{1.21a}$$

is the spin wave ellipticity, and

$$\omega_k = \left[\omega_r \left(\omega_r + \omega_m \sin^2\varphi \right) \right]^{1/2} \tag{1.21b}$$

is the dispersion of magnetostatic waves in infinite medium. From (1.20) we have two decoupled normal modes. They are

$$\begin{bmatrix} m^+ \\ m^- \end{bmatrix} = \begin{bmatrix} A \exp j(\omega_k t - \vec{k}\cdot\vec{r}) \\ 0 \end{bmatrix} \tag{1.22}$$

and

$$\begin{bmatrix} m^{+} \\ m^{-} \end{bmatrix} = \begin{bmatrix} 0 \\ B e^{j(\omega t + \beta z)} \end{bmatrix} \tag{1.23}$$

The first modes is a counter-clockwise elliptically polarized wave traveling along $\bar{k}$ direction. By counter-clockwise we mean a rotation from x axis to y axis. The other mode is a clockwise elliptically polarized wave traveling along $-\bar{k}$ direction.

1.5 Effect of Non-uniform Fields

The propagation characteristics of magnetostatic waves in temporally of spatially non-uniform bias field can best be understood from conservation theorems for small signal energy and momentum. These topics have been treated extensively by Morgenthaler[14,15]. The main results are described below.

The small signal energy density come from magnetic Zeeman dipolar, and exchange term (anisotropy energy is neglected). The electric field is of higher order which contributes little to the energy density term but the electromagnetic power flow is still of comparable magnitude, and thus can not be thrown away.

With some manipulation, Eqs. (1.1), (1.3), and (1.5) imply following conservation laws.

$$\nabla \cdot \bar{S} + \frac{\partial W}{\partial t} = -P \tag{1.24a}$$

$$\nabla \cdot \bar{T} - \frac{\partial \bar{g}}{\partial t} = \bar{f} \tag{1.24b}$$

where

$$S_j = (\vec{e} \times \vec{h})_j - \mu_0 \lambda \frac{\partial \vec{m}}{\partial x_j} \cdot \frac{\partial \vec{m}}{\partial t} \tag{1.25a}$$

$$W = \frac{1}{2}\mu_0 \frac{H_i}{M} |\vec{m}|^2 + \frac{1}{2}\mu_0 |\vec{h}|^2 - \frac{1}{2}\mu_0 \lambda |\nabla \vec{m}|^2 \tag{1.25b}$$

$$g_j = \frac{1}{2} \mu_0 \left(\frac{\partial \vec{m}}{\partial x_j} \times \vec{m} \right) \cdot \vec{i}_z \tag{1.25c}$$

are small signal power flow, energy density and momentum density. $\vec{t}$ is the stress tensor, p the power density, and $\vec{f}$ the force density. In a lossless system, p is the time derivative of biasing DC field, and $\vec{f}$ the sum of spatial derivatives of material parameters and vector fields.

From the quasi-particle point of view, it may be shown that

$$\langle W \rangle = n \hbar \omega \tag{1.26a}$$

$$\langle \vec{S} \rangle = \langle W \rangle \vec{v}_g \tag{1.26b}$$

$$\langle \vec{g} \rangle = n \hbar \vec{k} \tag{1.26c}$$

$$\langle \vec{t} \rangle = -\langle \vec{g} \rangle \cdot \vec{v}_g \tag{1.26d}$$

where $\hbar$ is the Planck constant divided by 2π, and $\vec{v}_g$ is the group velocity.

The notation $\langle\ \rangle$ denotes the time average over a microwave period corresponding to the center frequency of the wave packet. In a time varying but spatially uniform magnetic bias field, $\vec{f} = 0$ so

$$\frac{\partial \langle W \rangle}{\partial t} = p \tag{1.27a}$$

$$\frac{\partial \langle \vec{g} \rangle}{\partial t} = 0 \qquad (1.27b)$$

In such a medium the wave packet propagates with a constant momentum density but varied energy content and power flow. From Eqs. (1.26) we conclude that in a time varying but spatially uniform medium, magnetostatic spin waves propagate at constant wave number and constant average small signal momentum but with variable frequency, average power and average energy. Similarly, in a time invariant but spatially non-uniform medium, magnetostatic spin waves propagate at constant frequency average power and energy but with variable wave number and momentum[16].

In discussing the propagation of magnetostatic spin waves in the non-uniform medium, quasi-normal mode method is especially useful. In essense, it is just the so called Liouville or WKB approximation, which has been successfully applied to the spin wave propagation.

Suppose the bias magnetic field is temporally varied in magnitude, then all time derivatives in equations of motions (1.1) and (1.3) can not be replaced by $j\omega$. By taking derivatives of Eqs. (1.18) and substitute Eqs.(1.17) and (1.19) into the resulting equation, we get

$$\begin{bmatrix} \dot{m}^+ \\ \dot{m}^- \end{bmatrix} = \begin{bmatrix} j\omega_k + \Gamma_c & , & \Gamma_c \\ -\Gamma_c & , & -j\omega_k + \Gamma_c \end{bmatrix} \cdot \begin{bmatrix} m^+ \\ m^- \end{bmatrix} \qquad (1.28)$$

where

$$\Gamma_c = \frac{-1}{2}\frac{\dot{c}_k}{c_k} = \frac{\dot{\omega}_0}{4}\frac{\omega_M \sin^2\theta_k}{\omega_k^2} \qquad (1.29)$$

So, in a time varying medium, the two originally decoupled [illegible] become coupled. If the wave propagates initially along the

k direction, there will be a reflected wave when the DC field is varying. But in an adiabetically changing medium, ie., the biasing field varies only slowly over a period of oscillation, then r_c will be quite small, the reflected wave is then usually negligible.

If as usual $\Omega_c << \omega_k$, we see that

$$m^+ \cong A' \exp\left[\int_0^t (\omega + j\alpha)\,dt\right] \tag{1.30}$$

The wave propagates with variable frequency.

In a spatially non-uniform but time invariant medium, the spatial derivative must be retained. Quasi-normal modes still apply, similiar to the case we have discussed above. For details please refer to references [8,9,10]. The result is that $\exp(-jkx)$ is replaced by $\exp\int_0^x jk\,dx$ under suitable constraints, such as the wave number k should vary slowly enough over a wavelength and the wave is not too close to the singular point.

1.6 Summary of Experimental Facts

The excitation of spin waves can be achieved in many ways. Although direct excitation is possible under certain conditions[17], the most efficient way is to make use of temporally or spatially non-uniform fields.

Coupling to spin waves by acoustically injecting signals through time varying bias fields was successfully accomplished by Morgenthaler and Hu [18]. The more conventional method proposed originally by Schlömann to achieve this end is through the non-uniform internal field of non-ellipsoidal sample. This method is described below explaining the excitation of 90 degree propagating spin waves.

The correct excitation mechanism discussed by Collin and Hu

coworkers[1], is that low k magnetostatic waves are at first excited at the sample edge. As these waves propagate in the non-uniform medium, they are finally transformed into spin waves with large wave number. How large the k number can be depends on the absolute value to the total internal field and the dispersion relation of waves consistent with the given sample. The efficiency of excitation depends critically on the spatial gradient and absolute value of internal bias field as well as the spin wave line width of the sample used.

Damon and Van de Vaart observed 90 degree magnetostatic spin waves propagating in a normally magnetized disk or rod [19,20]. For the case of normally magnetized disk, the dispersion of magnetostatic modes was obtained. The dispersion of different modes is shown in Fig. 1.3. The resultant internal magnetic field, modified by demagnetizing field, is shown in Fig. 1.4. Approximately

$$H_i(r) = H_i(0) + \beta r^2 \tag{1.31}$$

where

$$\beta = \frac{3s}{2R^2} M$$

Here s is the thickness and R is the radius of the disk. We define

$$\delta H_i(0) = H_i(0) - \left[\omega_0(\omega_0 + \omega_m)\right]^{1/2} \tag{1.32}$$

For $\delta H_i(0) > 0$, propagation occurs solely as magnetostatic waves. The effect of non-uniform field is shown in Fig. 1.5. The wave is at first excited in the low k magnetostatic wave region at the disk edge, but as it propagates toward the center, the k number will increase. Because the dispersion gives a slower group velocity for fields close to $\left[\omega_0(\omega_0 + \omega_m)\right]^{1/2}$, the wave will slow down as the center of disk

and therefore most of the propagation will occur in that region. If H_0 is adjusted to give a smaller $\delta H_i(0)$, the delay time of magnetostatic waves will be increased. The maximum delay occur when $\delta H_i(0)=0$. Magnetostatic waves are extremely sensitive to changes of bias field. The delay time is a strong function of $\delta H_i(0)$. Further decrease of H_0 makes $\delta H_i(0)$ negative and so results in high k exchange dominated spin waves. These waves are faster, so the delay times will be lowered. Since exchange dominated spin waves have comparable wavelengths with that of elastic waves, they couple strongly with each other [2]. Within that region of operation, magnetoelastic interactions can not be neglected.

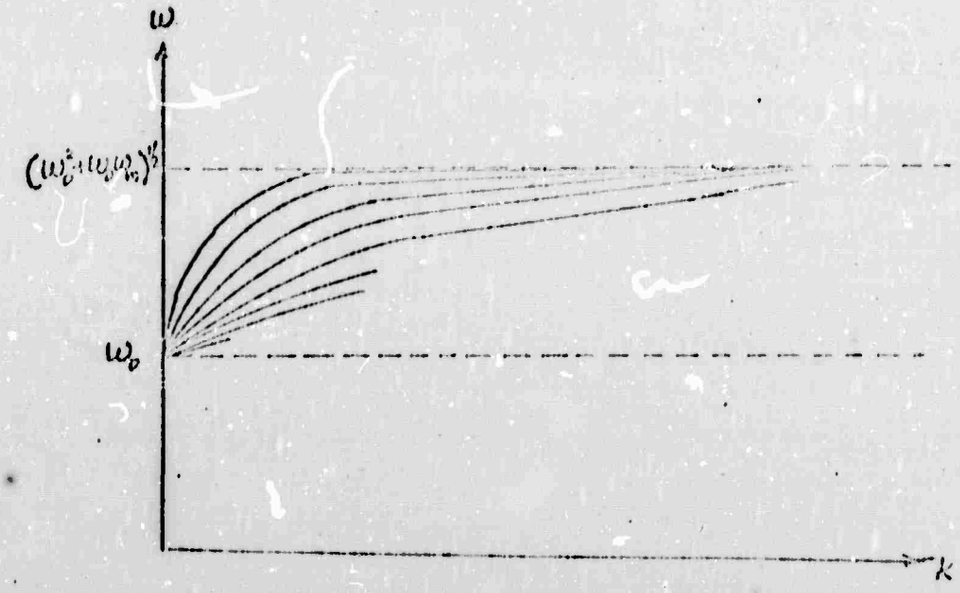

Fig. 1.3 Dispersion relations of different magnetostatic modes in disk

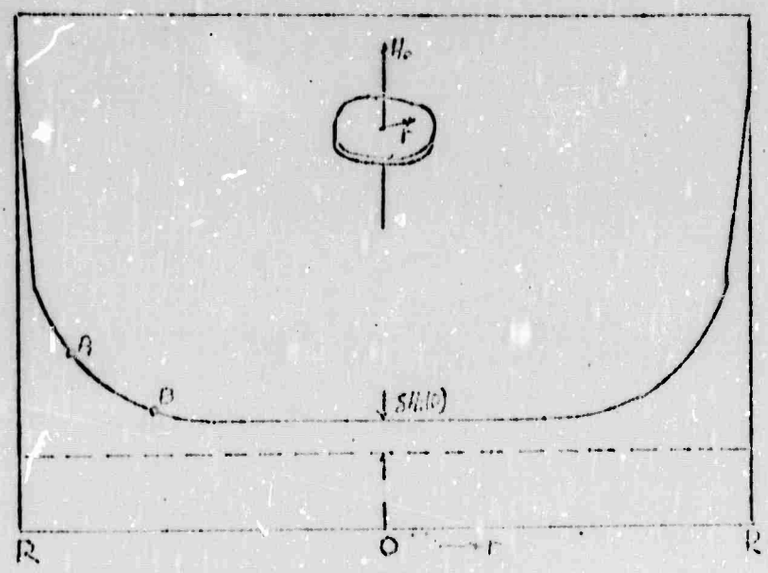

Fig. 1.4 Internal magnetic field profile

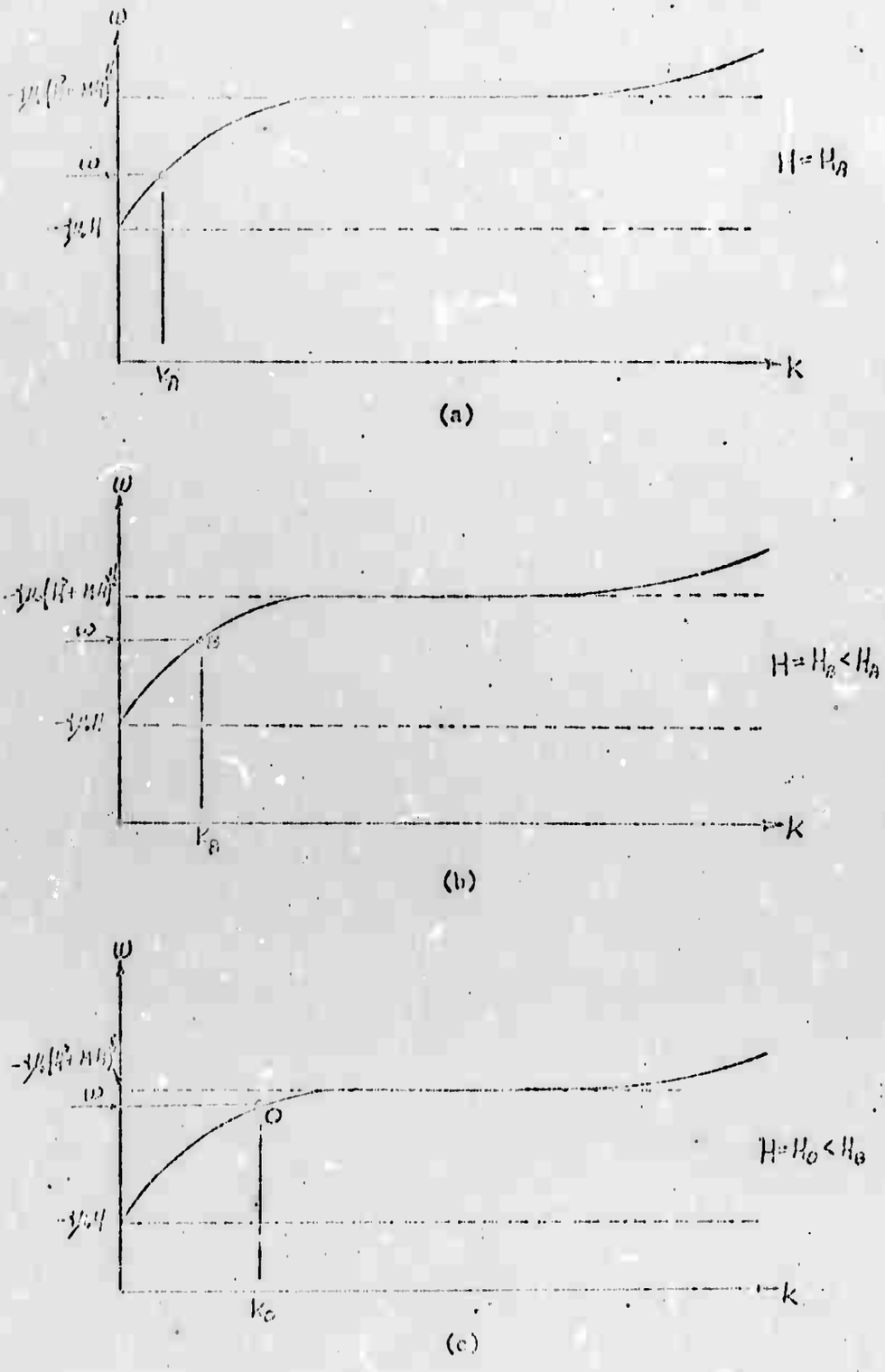

Fig. 1.5 Change of wave number in non-uniform internal

CHAPTER II

SURFACE MAGNETOSTATIC SPIN WAVES IN FERRITES

In the last chapter, we concentrated on magnetostatic spin waves in an infinite medium. Many properties and techniques discussed there can be carried straight through to the surface wave case, except that in the latter, boundary conditions play dominant roles. In this chapter, normal modes of surface waves are reviewed. The dispersion characteristics are discussed in detail. The exchange interaction is neglected here because we are primarily interested in magnetostatic waves with wave numbers smaller than 10^3-10^4 cm^{-1}.

Because of continuity and clarity of discussion, we present in the following sections only the highlights of magnetostatic surface waves. For mathematical details, please refer to Appendix C and D. References (2) and (6) are also pertinent.

2.1 Surface Modes of Semi-infinite Medium

Let us consider an semi-infinite medium, transversely magnetized in arbirary direction. The medium is termporally and spatially uniform (along Z_o and X_o direction). The geometry of the problem and the coordinate system used is shown below.

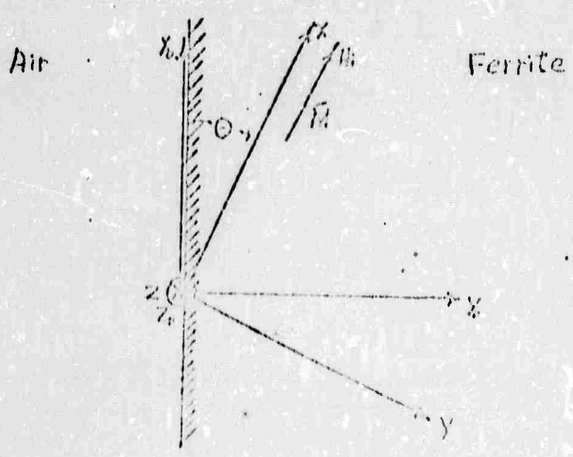

Fig. 2.1

Equations of motion for the ferrite are Maxwell's equations in the magnetostatic approximation and the torque equation as given by Eqs. (1.13) and (1.3). Boundary conditions require that tangential components of $\bar{h}$ and normal component of $\bar{h} + \bar{m}$ be continuous across the surface $y_0 = 0$.

Plane wave solutions uniform in x_0 direction are sought since they conform to the proposed excitation and appear to be reasonable physically. These waves vary spatially in the ferrite region according to $e^{-jk_z z - \alpha x}$, or equivalently, $e^{-jk_y y - \alpha \sin\theta_0 x - \alpha \cos\theta_0 y}$. The decay constant α is normally positive real for surface waves but in general may be complex.

Neglecting exchange and anisotropy fields, the $\bar{h}$ field is entirely dipolar in nature. Within the magnetostatic approximation it is given by

$$\bar{h} = \mathrm{Re}\left[-\bar{k}_f \frac{\bar{k}_f \cdot \bar{m}}{k_f^2} e^{-\alpha y_0} e^{-jk_z z_0}\right] \qquad \text{for } y_0 > 0 \qquad (2.1a)$$

$$\bar{h} = \mathrm{Re}\left[-\bar{k}_m \frac{\bar{k}_f \cdot \bar{m}}{k_f^2} e^{jk_y^0 y_0} e^{-jk_z z_0}\right] \qquad \text{for } y_0 < 0 \qquad (2.1b)$$

where

$$\bar{k}_f = -j\alpha \bar{i}_{y_0} + k_z \bar{i}_z \qquad (2.2a)$$

$$\bar{k}_m = -k_y^0 \bar{i}_{y_0} + k_z \bar{i}_z \qquad (2.2b)$$

and

$$k_y^0 = jk_y \qquad (2.3)$$

Constrained by the boundary conditions, it can be shown that (see appendix C) the only mode which can possibly be supported by a geometry shown in Fig. 2.1 is a surface mode characterized by a positive real α and negative real k_z. In a temprally uniform medium, all field quantities, such as $\bar{h}$, $\bar{m}$ vary according to $e^{j\omega t}$. The frequency ω is determined by the dispersion relation

$$\omega = \omega_k = \frac{(\omega_0 + \omega_m)\cos\theta}{2} + \frac{\omega_0}{2\cos\theta} \tag{2.4}$$

subject to the relations

$$\alpha' = -\left[\left|\frac{\omega_k^2 - \omega_0^2 - \omega_0\omega_m}{\omega_k^2 - \omega_0^2 - \omega_0\omega_m\cos\theta}\right|\right]^{1/2} k_z \tag{2.5}$$

and

$$\frac{k_z + \alpha'}{k_z - \alpha'} = -\frac{\omega_0}{\omega_m}\tan^2\theta \tag{2.6}$$

The surface modes in a semi-infinite medium, although a theoretical idealization, are the approximate magnetostatic eigenmodes supported by a ferromagnetic slab of thickness large compared to $1/\alpha'$. Most of the characteristics of surface wave propagation manifest themselves in this solution.

By examining the dispersion relation (2.4), we see that the frequency is independent of k. This is the limit of the true magnetostatic surface dispersion when k becomes large. Introduction of exchange interaction will cause the dispersion to curve upward proportional to k^2, while electromagnetic effects will bend the dispersion down in the low k region.

Since only one mode exists in semi-infinite medium, the geometry shown in Fig. 2.1 can support only nonreciprocal waves propagating in one direction. Because α' is always positive while the sign ω is controlled by $\cos\Theta$, for Θ less then $\pi/2$ the surface wave propagates in the negative z direction. On the other hand for Θ larger than $\pi/2$, it propagates in the positive z direction.

Furthermore, the left side of Eq. (2.6) is always less than 1, so that, for positive α,

$$0 \leq \frac{\omega_b}{\omega_m} \tan^2\Theta \leq 1 \tag{2.7}$$

No solution exists when Θ is larger than a critical angle given by

$$\Theta_{crit} = \cos^{-1}\left[\frac{\omega_b}{\omega_b+\omega_m}\right]^{1/2} = \cos^{-1}\left[\frac{H_i}{H_i+M}\right]^{1/2} \tag{2.8}$$

Upon substitution of (2.8) into (2.4), we see that at the critical angle

$$\alpha' = 0 \tag{2.9a}$$

$$\omega = \left[\omega_0\left(\omega_b+\omega_m\right)\right]^{1/2} \tag{2.9b}$$

which as expected is just the upper limit of the volume wave spectrum.

Therefore, as we till the bias field to increase the angle Θ, α' will decrease until the wave become uniform across the transverse plane and the dispersion will come down smoothly to the top of volume modes manifold as shown in Fig. 2.3.

2.2 Surface Modes of Finite Slab

With the introduction of another boundary at $x = D$ as

illustrated in Fig. 2.2, requires that the general solution should be a superposition of waves permitted by (2.5) .

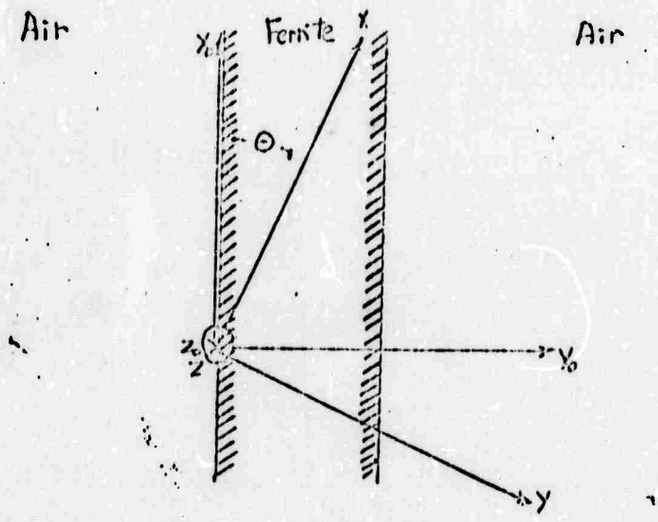

Fig. 2.2

The slab geometry shown in Fig. 2.2 is uniform along X_o and Z_o direction, and the dimension in X_o direction is considered infinite here. So in addition to a forward wave (denoted by index f), we have another contribution from the reflected wave (denoted by index r). Plane wave solutions of field quantities in air and ferrite regions are then

$$\bar{m} = Re\left\{\left[\bar{m}_f e^{-\alpha y_o} + \bar{m}_r e^{\alpha(y_o - D)}\right] e^{-jk_z z_o}\right\} \qquad \text{for } 0 \le y_o \le D \qquad (2.10a)$$

$$\bar{h} = Re\left\{\left[-\bar{k}_f \frac{k_f \cdot \bar{m}_f}{k_f^2} e^{-\alpha y_o} - \bar{k}_r \frac{\bar{k}_r \cdot \bar{m}_r}{k_r^2} e^{\alpha(y_o - D)}\right] e^{-jk_z z_o}\right\} \qquad \text{for } 0 \le y_o \le D \qquad (2.10b)$$

$$\bar{h} = Re\left\{\left[-\bar{k}_a^r\left(\frac{\bar{k}_r\cdot\bar{m}_r}{k_r^2} + \frac{\bar{k}_r\cdot\bar{m}_i}{k_r^2}e^{-2D}\right)\right]e^{jk_y^o y_o}e^{-jk_z z}\right\} \quad (2.10c)$$

for $y_o < 0$

$$\bar{h} = Re\left\{\left[-\bar{k}_a^r\left(\frac{\bar{k}_r\cdot\bar{m}_r}{k_r^2}e^{-2D} + \frac{\bar{k}_r\cdot\bar{m}_i}{k_r^2}\right)\right]e^{-jk_y^o(y_o-D)}e^{-jk_z z}\right\} \quad (2.10d)$$

for $y_o > 0$

where

$$\bar{k}_a^r = -k_y^o \bar{i}_{y_o} + k_z \bar{i}_z \quad (2.11a)$$

$$\bar{k}_a^f = k_y^o \bar{i}_{y_o} + k_z \bar{i}_z \quad (2.11b)$$

and

$$k_y^o = j k_z \quad (2.12)$$

and k_z are positively and negatively real respectively. They are related to ω by Eq. (2.5).

Despite infinitely many discrete volume modes that can exist in consistent with the slab geometry, there are only two surface modes that can possibly be supported as required by boundary conditions across both slab surfaces (see appendix D and section 2.3). These surface modes vary sinusoidally in time as $e^{j\omega t}$ in temporally uniform medium. The frequency ω is given by

$$\omega = \pm\,\omega_k \quad (2.13a)$$

where ω_k is the positive solution of the following dispersion relation

$$\omega_k^2 = \omega_0^2 + \omega_0\omega_m\left(\frac{1+\cos^2\theta}{2}\right) \pm \frac{-\omega_m^2\cos^2\theta + \omega_m^2\coth\alpha D\left[\omega_0^2\sin^2\theta\left(\coth^2\alpha D - 1\right) + \omega_m^2\cos^2\theta\right]^{1/2}}{2\left(\coth^2\alpha D - 1\right)} \tag{2.13b}$$

Let Q_f and Q_r be the forward and reflected wave amplitude of any component of $\bar{m}$ in (2.10), eg., m_{fz}, and m_{rz}. Then Q_f and Q_r are related by

$$\frac{Q_r}{Q_f} = -\frac{k_z\left[\omega_k + (\omega_0+\omega_m)\cos\theta\right] + \alpha\left(\omega_k + \omega_0\cos\theta\right)}{k_z\left[\omega_k + (\omega_0+\omega_m)\cos\theta\right] - \alpha\left(\omega_k + \omega_0\cos\theta\right)} e^{-\alpha D} \tag{2.14}$$

Transverse field patterns of these two surface modes are shown in Fig. 2.3. It can be shown that surface mode solutions are possible only when the ferrite slab is magnetized with a biasing angle θ satisfying

$$1 \geq \left|\cos\theta\right| \geq \left[\frac{\omega_0}{\omega_0+\omega_m}\right]^{1/2} \tag{2.15}$$

The critical angle, therefore has two values. One is equal to that of the semi-infinite medium, another is 90 degree larger. This is just as expected from the geometrical symmetry of our problem shown in Fig. 2.3.

Physically, both surface modes are identical. They cling to different slab boundaries and propagate in opposite directions - completely decoupled in a medium uniform both in time and in space (along z direction).

If $\theta = 0$, Eq. (2.13b) is reduced to the Damon and Eshbach mode[2] defined by

$$\omega_k^2 = \omega_0^2 + \omega_0\omega_m + \omega_m^2\left[2\left(\coth\alpha D + 1\right)\right]^{-1} \tag{2.16}$$

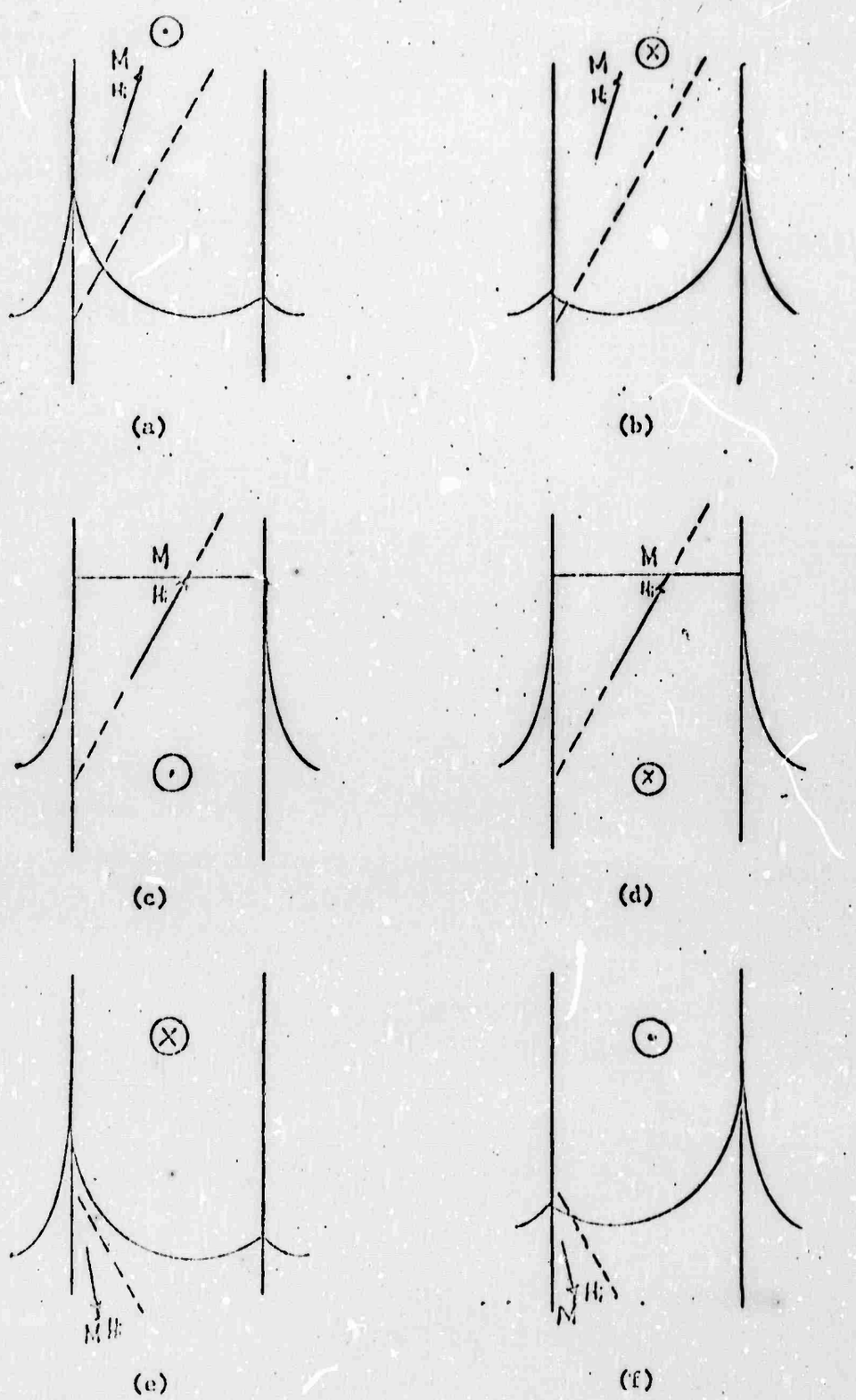

Fig. 2.3 Magnetostatic surface mode patterns in a ferrite slab.
Dashed lines shown define the critical angle.
Dots and crossbars show the wave propagation direction.

The other limit is when $\alpha' D \longrightarrow \infty$. This is the case when α' or D become very large enough so that the slab is essentially semi-infinite in nature. Under such condition, $\coth \alpha' D \longrightarrow 1$ and Eq. (2.13b) yields (2.4) as expected. For a given k_z or α', Eq. (2.13b) gives a solution of ω_k lying within the surface wave frequency band

$$\left[\omega_0(\omega_0+\omega_m)\right]^{1/2} \leq \omega_k \leq \frac{\omega_0+\omega_m}{2}\,|\cos\theta| + \frac{\omega_0}{2|\cos\theta|} \leq \omega_0 + \frac{\omega_m}{2} \qquad (2.17)$$

The dispersion relation (2.13b) is shown in Fig. 2.4.

2.3 Volume Modes In Finite Slab

Previously, we have discussed surface modes in finite slab. Because our approach is essential general, all equations cited before are valid no matter whether α' is real or complex. To restrict ω_k to lie within the frequency band given by Eq. (2.16), the dispersion (2.13b) is characterized by a positive real α' leading to hyperbolic functions. Therefore the surface wave dispersion has only a single branch rising from the top of volume wave manifold which eventually approaches the upper limit at large wave number.

To investigate the 90 degree(defined for our purpose to be the magnetostatic volume waves propagating along the z direction) volume wave spectrum in finite ferrite slab, we restrict ω_k to lie between the following limits.

$$\left[\omega_0^2+\omega_0\omega_m\cos^2\theta\right]^{1/2} \leq \omega_k \leq \left[\omega_0^2+\omega_0\omega_m\right]^{1/2} \qquad (2.18)$$

Within this frequency band, α' becomes imaginary implying that the waves also vary sinusoidally in the transverse plane. The dispersion

relation (2.13b) or (D.14b) is then characterized by the tangent function instead of the hyperbolic tangent. Hence, a series of volume modes is possible.

To facilitate the discussion, we define

$$r_a = \frac{\omega_k^2 - (\omega_0^2 + \omega_0\omega_m\cos^2\theta)}{\omega_0\omega_m(1-\cos^2\theta)} \qquad 0 \le r_a \le 1 \tag{2.19}$$

which measures how far from the bottom of volume wave frequency band ω_k lies. In particular,

$r_a = 0$ implies $\omega_k^2 = \omega_0^2 + \omega_0\omega_m\cos^2\theta$

and $r_a = 1$ implies $\omega_k^2 = \omega_0^2 + \omega_0\omega_m$

We also define

$$q = j\beta \tag{2.20a}$$

$$\beta = \left[\frac{\omega_0^2 + \omega_0\omega_m - \omega_k^2}{\omega_k^2 - \omega_0^2 - \omega_0\omega_m\cos^2\theta}\right]^{1/2}|k_z| = \left[\frac{1-r_a}{r_a}\right]^{1/2}|k_z| \tag{2.20b}$$

With these definitions, the dispersion relation (D.14b) becomes

$$\left[\frac{1}{2}\left(\frac{\omega_m}{\omega_0}\cot^2\theta + 1\right) - r_a\right]\tan\beta D = \left[r_a(1-r_a)\right]^{1/2} \tag{2.21}$$

Evidently different modes correspond to different solutions of βD. Now we label these modes as follows

$$(n-1)\pi \le \beta D \le n\pi \qquad n = 1, 2, 3, \cdots \tag{2.22}$$

then $0 \le \theta \le \theta_{crit}$

we have

$$\frac{1}{2}\left(\frac{\omega_m}{\omega_0}\cot^2\theta + 1\right) \geq 1 \geq r_a \geq 0$$

and there are always solutions for Eq. (2.21). However when

$$\theta_{crit} < \theta < \pi/2 \quad , \text{ it follows that}$$

and we have a singular point at

$$r_a = \frac{1}{2}\left(\frac{\omega_m}{\omega_0}\cot^2\theta + 1\right) \tag{2.23}$$

For $\theta = \pi/2$, the value of r_a is 1/2.

Forutnately, around that singular point, $\tan\beta D$ changes from plus to minus infinity, hence βD changes only slightly from $(n - \frac{1}{2})\pi - \epsilon$ to $(n - \frac{1}{2})\pi + \epsilon$ for the same well defined mode. The dispersion curves join smoothly from each side of that singular point as shown in the Fig. 2.5. Discontinuities at such singular points are removable by suitable modifying our over simplied model to include spin wave losses.

Fig. (2.4) and Fig. (2.5) are dispersion diagrams for $\theta \leq \theta_{crit}$ and $\theta > \theta_{crit}$ respectively. The propagation constent k_z can be calculated from Eqs. (2.20b). Note that at $\theta = 0$, the volume wave spectrum is suppressed, while for $\theta \geq \theta_{crit}$, the surface wave disappears completely.

Being imaginery, the reflected wave amplitude is equal to the forward wave amplitude, with a phase change determined by ω_k , ω, θ and D as can be seen from Eq. (2.14).

From Eq. (2.14)

$$(\quad) = (\quad) e^{j(\quad \beta D)} \tag{2.34a}$$

where

$$\Psi = \pi + 2\tan^{-1}\left\{\frac{k_z}{\beta}\left[\frac{\omega_k+\omega_0+\omega_m}{\omega_k+\omega_0\cos\Theta}\right]+j\alpha\left[\frac{\omega_k+\omega_0\cos\Theta}{\omega_k+\omega_0\cos\Theta}\right]\right\} \qquad (2.24b)$$

So, because of interference, volume modes have standing wave patterns in the transverse plane. From Eqs. (2.24) and (2.10a), m_y can be solved to be varying in y_o as

$$\cos\left[\beta(y_o-D)+\Psi/2\right]\cos\left(\beta D-\Psi/2\right) \qquad (2.25)$$

Similarly expressions can be obtained for other field quantities.

Transverse patterns for different modes, labeled according to (2.22), are shown in Fig. (2.6). They are drawn at fixed frequency near the top edge of volume mode manifold, ie.,

$$\omega_k \lesssim \left[\omega_0(\omega_0+\omega_m)\right]^{1/2} \quad \text{or} \quad r_a \lesssim 1$$

The propagation constant k_z is now a function of Θ. Although Ψ is less sensitive to changes in Θ, modes patterns are strong functions of βD and Θ. For large k_z, approximately $\Psi \approx \pi$, so, Eq. (2.25) becomes simply

$$\sin\left[\beta(D-y_o)\right]\cos(\beta D)$$

2.4 Switching of Surface Modes

In a ferrite slab, all the surface modes that can exist are shown in Fig. 2.3. For Θ close to 0 or π there is only one unique surface mode propagating in negative z direction. As shown in Fig. (2.3a) Fig. (2.3b), both waves climbing to different surfaces appear to be

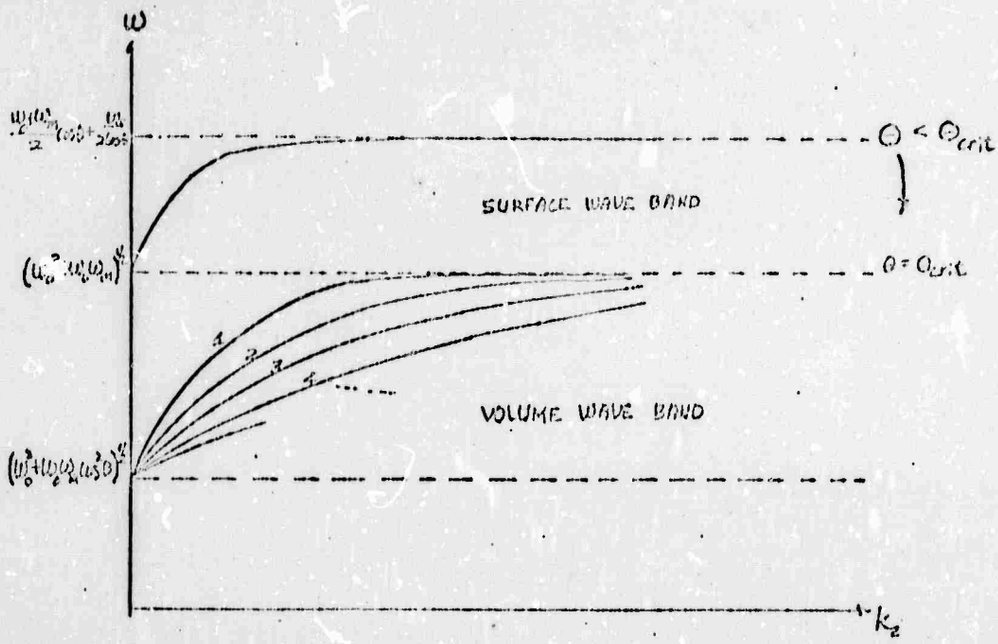

Fig. 2.4 Magnetistatic wave dispersion curve for normal modes of a ferrite slab biased with $|\cos\theta| = |\cos\theta_{crit}|$. The upper branch is the surface wave dispersion. The lower multiple branches are for volume wave propagating in z direction.

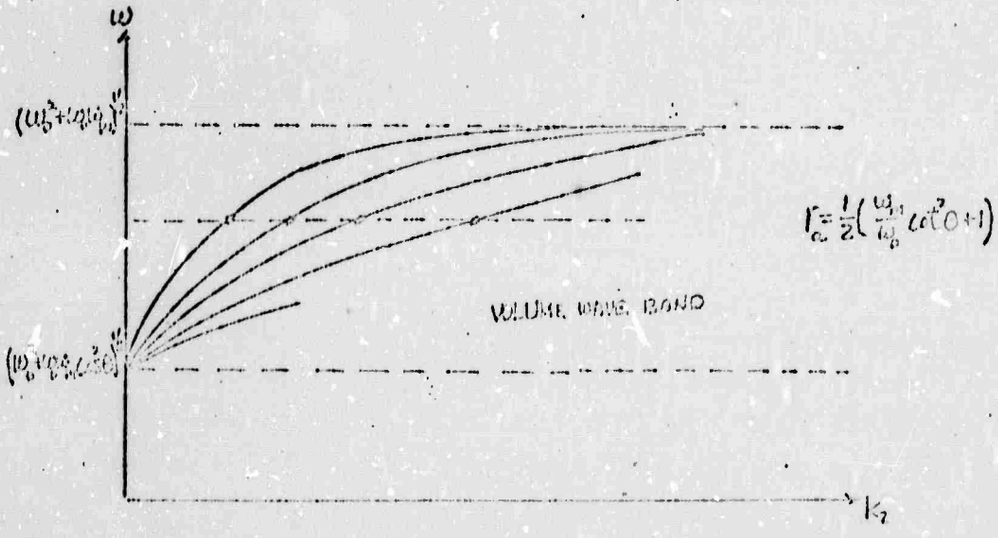

Fig. 2.5 Magnetostatic volume wave dispersion curves of a ferrite slab biased with $|\cos\theta| < |\cos\theta_{crit}|$.

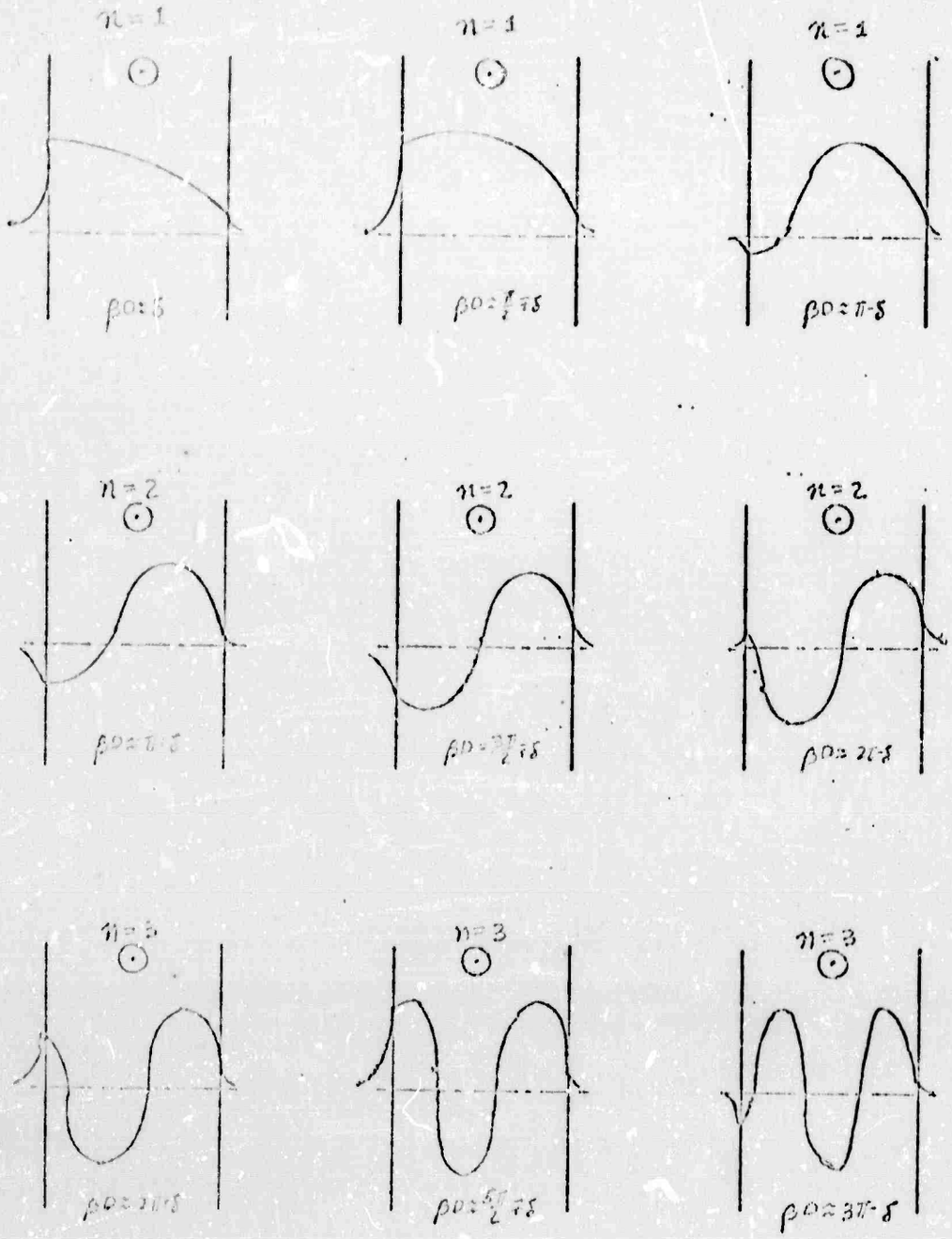

(a) $\Theta < \Theta_{crit}$ (b) $\Theta \approx \Theta_{crit}$ (c) $\Theta \approx 90°$

Fig. 7.6 Volume mode patterns for fixed $\omega_k \leq \omega [\omega_0^2 + \omega_{ce}\omega_{ci}]^{1/2}$. k_z is different for different Θ.

switchable from one surface to the other by switching the biasing magnetic field direction.

In a spatially uniform (along z direction) medium, the wave number k_z of the wave remains invariant as the direction of $\vec{H}$ will adjust the mode pattern in time. If Θ is increased adiabatically, so that Θ is varying slowly enough so that the precessing spins can follow $\vec{H}$ continuously, the mode pattern of the wave will then adjust itself smoothly to be consistent with the instantaneous geometry. A crude criterion to guarantee the adiabatic condition is $\dot{\Theta} \ll \omega_0$.

As discussed in the last section, we know that surface modes can be supported only when

$$1 \geq |\cos\Theta| \geq \cos\Theta_{crit}$$

Now given a surface mode propagating in -z direction with the bias angle Θ initially small, the mode will then pass through transversely uniform mode, volume mode and reversely to reach its final surface mode state when Θ is changing from nearly 0 passing through Θ_{crit} to nearly π. Graphically, this is illustrated in Fig. (2.4), this process can be represented by drawing a vertical line of constant k_z in the dispersion diagram in Fig. (2.4), its intersections with the dispersion curves are possible modes. When Θ is increasing from small value, ω_k will be lowered until approximately equal $[\omega_0(\omega_0+\omega_M)]^{1/2}$ corresponding to $\cos\Theta \geq \cos\Theta_{crit}$ and then be raised again.

Mathematical formulation of the switching problem is tedious and has not yet been worked out in detail. Procedures, nevertheless, are identical to those used in the section 1.5. Following the derivation in Appendix D, we see that all equations up to Eq. (D.30b) still apply if

the medium is varied adiabatically in time. But in this case parameters such as Ω , α , ω_k^2 are time functions.

The procedure to follow is as follows: Differentiate Eq. (D.10a), then use Eqs. (D.9) and (D.10b), the resultant equation is Eq.(D.11) plus an additional term which mixes the originally uncoupled normal modes and thus produces wave coupling and reflections. From this modified coupled quasi-normal modes equation, approximate solutions and other necessary information can be found. The result is a propagating wave with slowly varying amplitude and frequency. The reflected wave, shown in Fig. (2.3b) if we start with the wave shown in Fig. (2.3a), is expected to be small. However, details have to be investigated for $\Theta \approx \Theta_{crit}$, before any precise statement be made.

CHAPTER III

EXPERIMENTAL RESULTS

In the last chapter, magnetostatic surface waves have been discussed. Here experimental results from microwave pluse echo experiments are presented. The samples used are yttrium iron garnet (YIG) single crystal slabs of various shapes. Magnetostatic surface waves were excited by means of electromagnetic pulses injected (and detected) by short fine wires placed across the sample. The time delay and insertion loss were recorded as a function of the applied magnetic field at frequencies between 3.0 to 4.0 G.HZ. All experiments were performed at room temperature.

3.1 Experimental Set Up

The microwave system used consists mainly of the microwave signal sourse and the detection system. The signals used are microwave pulses of approximately 0.15 sec. and with a repetition rate between 1K.HZ. and 5K.HZ.

Shown in Fig. 3.1 is the microwave circuit diagram. Its main features are:

The signal generating system consists of a S-band (2.0 to 4.0 G.HZ.) sweep generator (Alfred 650) followed by a PIN modulator(Hp 8732B) which, when modulated by a pulse from a pulse generator (hp 8403A), is capable of producing a microwave pulse of a minimum duration of 0.15 sec. One regular and one precision attenuator (Alfred 1103) are used. In our experiments, a matched circulator is used as an isolator; the stub tuners (Weinschel 1870) are for impendance matching.

The receiving system consists of two parts. One is the superheterodyne system consist of a local oscillator (Alfred 650), one

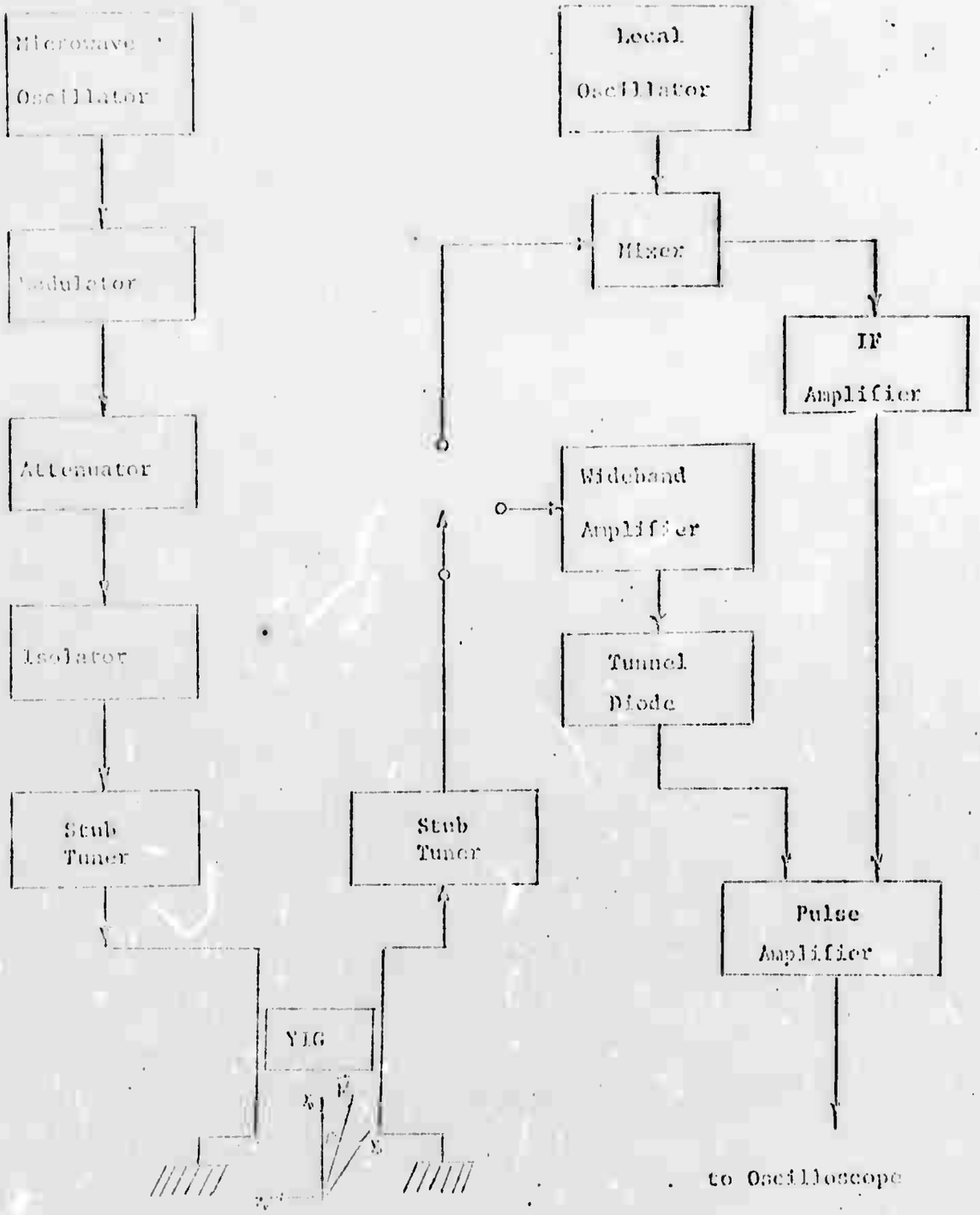

YIG Fire Mixer Assembly

Fig. 3.1 Schematic of the circuitry used to study the behavior of magnetostatic surface waves.

low noise IF amplifier (which has 110db gain) and one crystal detector as a substitute for a mixer. Another envelope detection system has one wide band, low noise transistor amplifier (Avantek AWA-40508/PS-5) and a tunnel diode (Aertech D112B).

The detected signal is amplified by a fast pulse amplifier (hp 462A) and displayed by an oscilloscope (Tektronics 585A).

3.2 Description of Experiments

Three samples were used in the experiments, all of them YIG single crystal slabs. For convenience of discussion, we label them as:

Sample 1: A circular disk 1cm in diameter and 1.4 mm in thickness. The slab plane is (110).

Sample 2: A 5x4x0.5 mm rectangular slab with a (110) plane and the long dimension parallel to (100) direction.

Sample 3: A 8x480.5 mm rectangular slab with a (110) plane and the long dimension parallel to (100) direction.

All experiments performed have following geometry, the $\vec{M}$ always lie in the (100) plane transverse to the wave propagation direction.

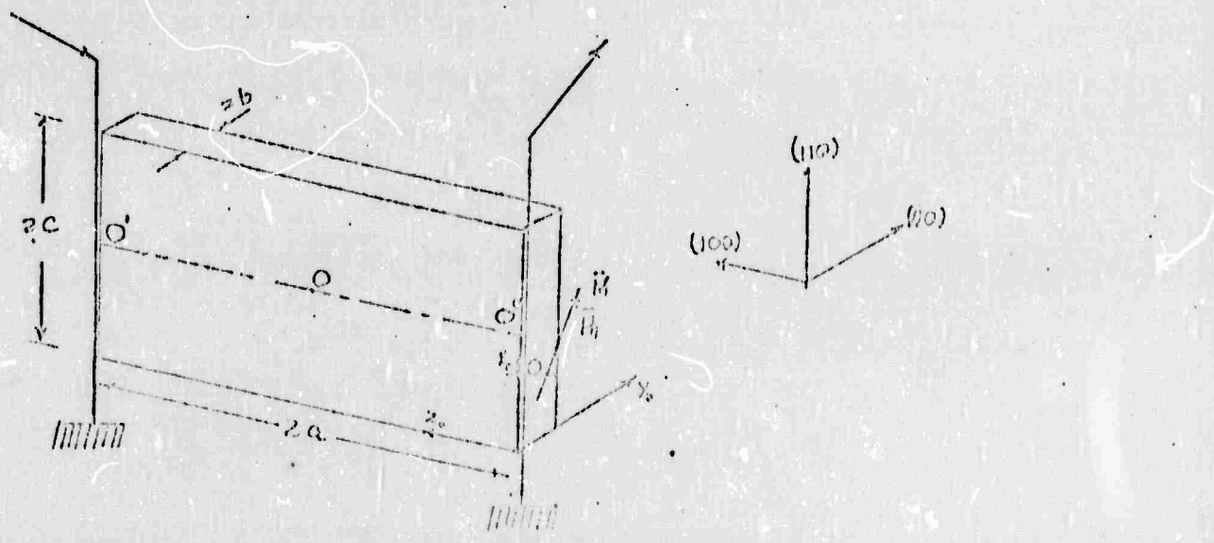

Fig. 3.2

Energy is coupled into and out of the samples by grounded fine wire antennas along the edges.

Because of crystalline anisotropy and demagnetizing field, the internal field and the external applied field are related by

$$\bar{H}_i = \bar{H}_o + \bar{H}_A - \bar{H}_{demag} \tag{3.1}$$

When the external biasing field is tilted away from the slab surface $(\theta \neq 0)$ shown in Fig. (3.2), the demagnetizing field is a very complicated function. For the case that the external field is parallel to the slab plane ($\theta = 0$), the first order demagnetizing field in the x_o direction along the center line 0'0", calculated from Schlomann's formula [21] is

$$H_{demag} = M \frac{1}{2\pi} \left[\cot^{-1} f(z) + \cot^{-1} f(-z) \right] \tag{3.2a}$$

$$f(z) = \frac{[(a-z)^2 + 4b^2 + c^2]^{1/2} c}{2b(a-z)} \tag{3.2b}$$

where M is 17500e and z is the distance measured from the center point 0.

Therefore, the internal field profile along 0'0" is trough like as shown below.

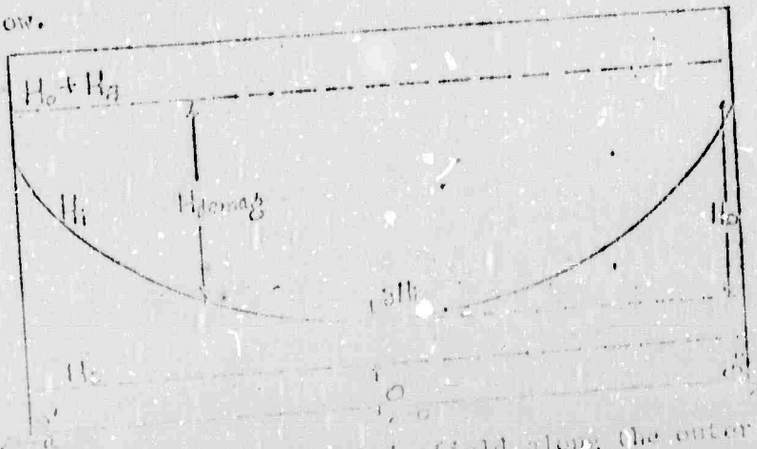

Fig. 3.3 Internal magnetic field along the outer line of the slab surface

In Fig. 3.3

$$\delta H_i = H_i(0) - H_c \tag{3.3}$$

where

$$H_c = \frac{1}{\gamma\mu_0}\left[\omega_0 + \frac{\omega_m}{2}\right] \tag{3.4}$$

Since the dispersion relation of magnetostatic surface waves is similar to that of 90 degree magnetostatic volume waves, the surface waves should therefore behave in a manner similar to that described in Chapter I.

To excite the magnetostatic surface wave, the energy is first coupled in at the sample edge as a low k magnetostatic mode. As it propagates towards the center, the frequency remains constant but the wave number increases according to the dispersion relation and the internal field value at each point.

If an electromagnetic wave pulse is fed into the sample at one end and detected at the other it suffers a total time delay given by

$$T = 2\int_0^{\circ} \frac{dz}{v_g} \tag{3.5}$$

where $v_g = \frac{\partial\omega}{\partial k_z}$

Assuming surface spin wave propagation the latter is calculated from the appropriate dispersion relation. Since the internal magnetic field is in general non uniform, Eq. (3.5) is usually calculated by numerical methods.

When operating in magnetostatic region, δH_i in Fig. (3.3) is larger than zero. With δH_i decreasing, the pulse delay time will increase to a maximum corresponding to $\delta H_i = 0$ which occurs at the cut off field $H_i(0) = H_c$. Beyond the cut off, surface spin waves with much larger k number are expected to be excited. However such waves have

been observed due to many experimental difficulties. The high k surface spin wave has not been well understood. Presumably, to observe it, surface boundary conditions of the sample become more critical because of the smaller wavelength involved. Furthermore, we should operate with lower magnetic bias fields in the frequency range employed in these experiments. But then incomplete saturation of the sample occurs leading to increased losses due to domain wall effects. In addition, the internal field profile is shifted in an unknown manner.

Experiments done on the different samples all started quantitatively with the magnetization parallel to the slab surface, ie., $\Theta = 0$, and then proceeded to the case $\Theta \neq 0$. Pulse time delay T and the cut off fields were determined for the maximum time delay could be measured. In addition to surface waves, 90 degree magnetostatic volume waves and zero degree magnetostatic volume waves were also observed in the same sample and experimental geometry.

In the beginning, experiments were done on one of the optically polished surface of sample 1. No convincing surface wave pulse was observed. One of the reasons is probably due to the flat profile of the internal field caused by the round sample shape. Later, a soft iron substrate of rectangular dimensions 30x15x1.5 mm was placed around the sample, to modify the field profile. Detectable signals were then observed. Both large surfaces of sample 2 were originally mechanically polished to be optically flat. The internal field of this sample is quite uniform and the H_n value in Fig. 3.3 calculated from Eq. (3.2) is only about 200e. With that sample, the maximum signal delay time detected was about 0.1 μsec. Mechanically polished surfaces are usually strained and are probably responsible for the large surface spin wave linewidth. It was discovered by J. D. Adam[22] that surface wave propagation loss would be

significantly reduced by polishing the surface chemically using the ortho-phospheric acid under suitable conditions [22]. To achieve the same purpose, the second sample was polished mechanically using syton, a kind of jelly of SiO_2 and water, which reacted chemically with the sample surface. By means of this simpler syton polishing process, we were able to get a strain free surface but at the sacrifice of the optical flatness. Using this sample, a delayed surface wave pulse up to 1 microsecond was detected. The improved linewidth was found to approximately several times smaller than the original value.

Experiments done on sample 3 have so far given the best results. Although the surfaces are only mechanically polished, we have already detected an up to 0.6 μsec. delayed pulse with reasonably good pulse shape. Magnetostatic (90 degree) volume waves were also observed. When H was tilted at an angle a little larger than the surface wave cut off angle, the best volume mode signals were detected to have a maximum delay of 2.0 μsec.

Qualitatively, the internal field profile plays a dominant role in coupling and it is more efficient to couple the electromagnetic energy into the low k magnetostatic modes. Surface conditions are critical and place severe constraints on how long the surface wave pulse can be delayed yet still be detectable. Usually the longer the delay time the worse the pulse shape due to the dispersive propagation characteristic of magnetostatic modes. Non-reciprocity of surface waves have also been observed in confirmation with the theory.

Using the third sample and the experimental configuration shown in Fig. 3.2, magnetostatic surface wave pulses with more than 0.4 μ sec. delay were detected when the external field was parallel to the slab

surface with either $\theta = 0$ or $\theta = \pi$. With one of the slab surfaces $y_0 = 0$ grounded by a metal plate, only surface wave pulses with about 0.1 μsec. delay were observed if the magnetic field was biased such that $\theta = 0$. But when the magnetic field direction is reversed to $\theta = \pi$, then again surface wave pulses with 0.4 μsec. delay appear. These facts tell us that surface waves are non-reciprocal. For a given propagation direction (sign of $\tilde{k}$) they travel on different slab surfaces $y_0 = 0$ or $y_0 = b$ (shown in Fig. 3.2) depending upon the direction of the biasing field. In addition, the surface wave dispersion relation changes according to the different boundary condition.

Similar phenomena were observed when the external field is tilted away from the slab plane ($\theta \neq 0$).

3.3 Data and Results

All experiments were done at room temperature with the geometrical configuration shown in Fig. 3.2.The external magnetic field was applied either parallel to the slab surface ($\theta = 0$) or tilted ($\theta \neq 0$) at an angle with respect to slab surface. Because of the demagnetizing field, the intensity and inclination angle ϕ of the external applied field H_0 are different from θ and H_i. The appropriate relations are given by Eqs. (B4) in Appendix B.

Fig. 3.4 shows the first order demagnetizing field calculated according to Eq. (3.2) when the field is applied parallel to the slab surface. It can be seen from the figure that the internal field profile inside sample 2 is much flatter than that inside sample 3.

Figs (3.5) to (3.10) are experimental data for sample 3 compared

Both large faces of the sample 3 are mechanically polished to be optically flat. Fig. 3.5 shows the microwave pulses at 3.9 G.Hz. These pulses were injected and detected by fine wire antennas. As they propagated through the YIG slab as magnetostatic surface waves, they suffered a time delay increasing with the decreasing biasing field. The input power of the signals used increases from (a) to (e) in Fig. (3.5).

In Fig. 3.6, the surface wave time delay and attenuation are plotted against the external biasing field. The disagreement in theory and experiment is believed mainly due to the incomplete saturation of the ferrite sample.

With the configuration shown in Fig. 3.2, we observed also the 90 degree magnetostatic volume waves propagating along z_0 direction as well as the 0° degree magnetostatic volume waves propagating along x_0 direction in addition to the magnetostatic surface waves. Cut off fields corresponding to the maximum delay time of those waves are plotted in Figs.(3.7) to (3.9). Dotted lines are theoretical curves including the magnetic anisotropy but without demagnetizing field correction. Solid lines are those including the demagnetizing field of the magnitude 121.86Oe.

Cut off fields for 90 degree volume waves and the excitation frequencies are related by the following formula

$$\omega_k = \left[(\omega_0' + N_{zz}\omega_m)(\omega_0' + \omega_m)\right]^{1/2}$$

ω_0', N_{zz} are given in Appendix B. For 0° degree volume waves, it is

$$\omega_k = \left[\omega_x'(\omega_0' + N_x\omega_m)\right]^{1/2}$$

From Figs. (3.7) to (3.9), it can be seen that better agreement

are obtained at higher applied field. At low fields, the sample is usually not saturated.

The Fig. (3.10) shows the comparision of experimental cut off fields of magnetostatic surface waves and 90 degree volume waves propagating along z direction with theoretical predictions.

Calculations of these cut off fields are given in Appendix A and B. The anisotropy fields are added and the demagnetizing fields are introduced trough two demagnetizing factors $N^a_{y_o}$ and $N^a_{z_o}$ (see Appendix B). The dotted curves correspond to $N^a_{y_o}=0.02$ and $N^a_{z_o}=0.97$. The solid curves correspond to $N^a_{y_o}=0.063$ and $N^a_{z_o}=0.92$.

The sample 2 is a 5x4x0.5 mm YIG crystal slab. Originally the slab surfaces were mechanically polished to be optically flat. With that kind sample, no detectable pulse with more than 0.1 sec. delay time were observed. When the same sample was polished with syton, better signals were detected. Results are presented in Figs. (3.11) to (3.14). Basically they give the same information as previous figures for sample 3. However, in Fig. (3.11b), the wiggle occurs at about 0.3 sec. delayed from the original pulse is the echo traveling around the sample, so it has a time delay three times longer than that of the first delayed pulse.

The Fig. (3.12) shows that we have less over all insertion losses, estimated to be about 15DB, when the sample is polished chemically with syton. In Fig. (3.14) the dotted curves are calculated with $N^a_{y_o}=0$ and $N^a_{z_o}=1.0$, the solid curves are calculated with $N^a_{y_o}=0.07$ and $N^a_{z_o}=0.9$.

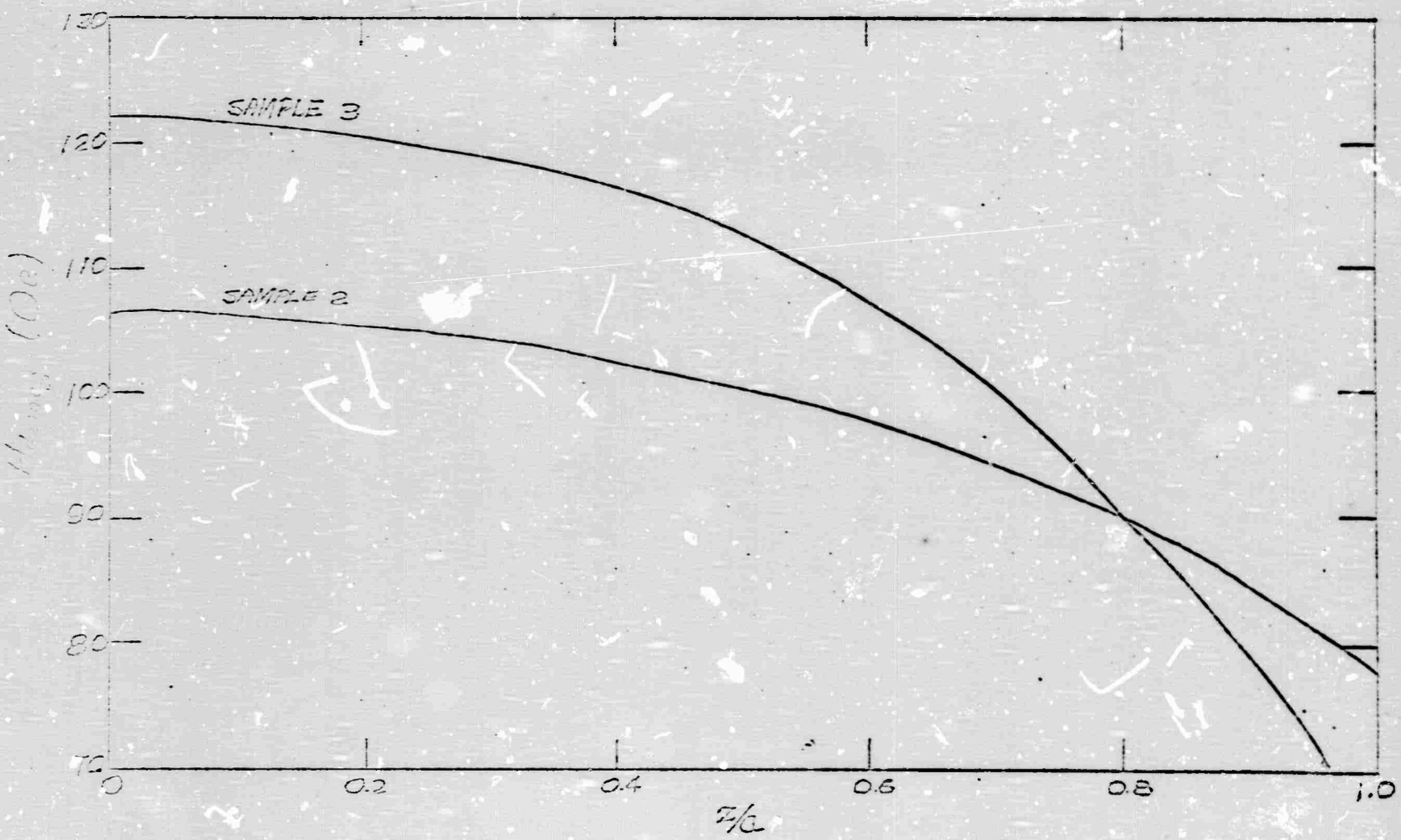

Fig. 3.4 The demagnetizing fields when the slab is magnetized parallel to the slab surface. a for sample 2 is 0.25 mm and for sample 3 is 0.4 mm.

(a) H_o = 612.2Oe

(b) H_o = 597Oe

(c) H_o = 593.8Oe

(d) H_o = 592.2Oe

(e) H_o = 595.7Oe

NOT REPRODUCIBLE

Fig. 3.5 Delayed magnetostatic surface wave pulses at 3.9 GHz. Experiments were done on a 8x4x0.5mm single crystal slab with an external magnetic field H_o applied parallel to the slab surface. The input signal power increases from (a) to (e). (a) shows the transmitted signal with negligible delay time. Time scale = 0.5 μsec/cm.

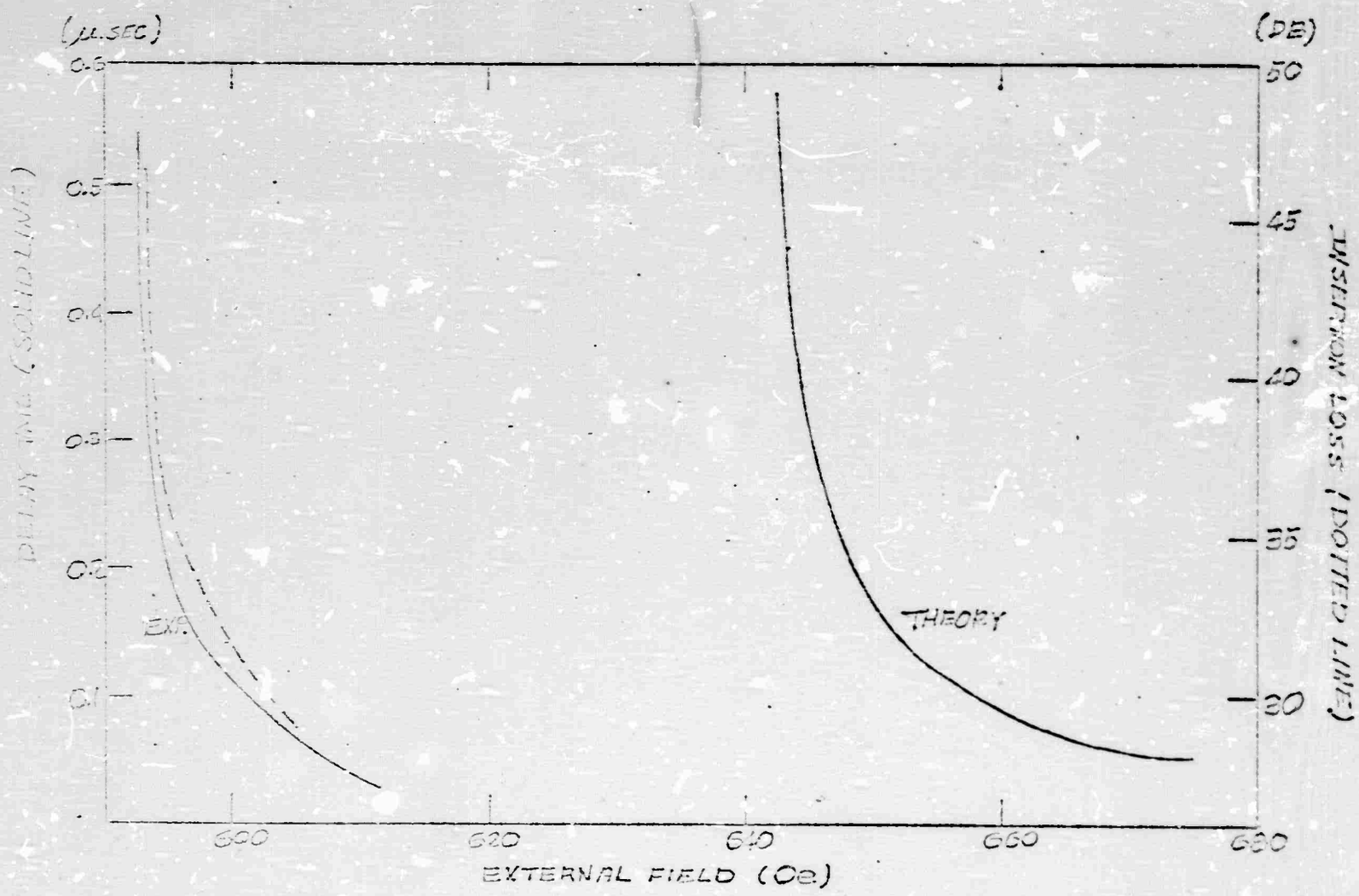

Fig. 3.6 Delay time of magnetostatic surface wave at 3.9 G.HZ for the sample 3. The external field is applied parallel to the slab surface.

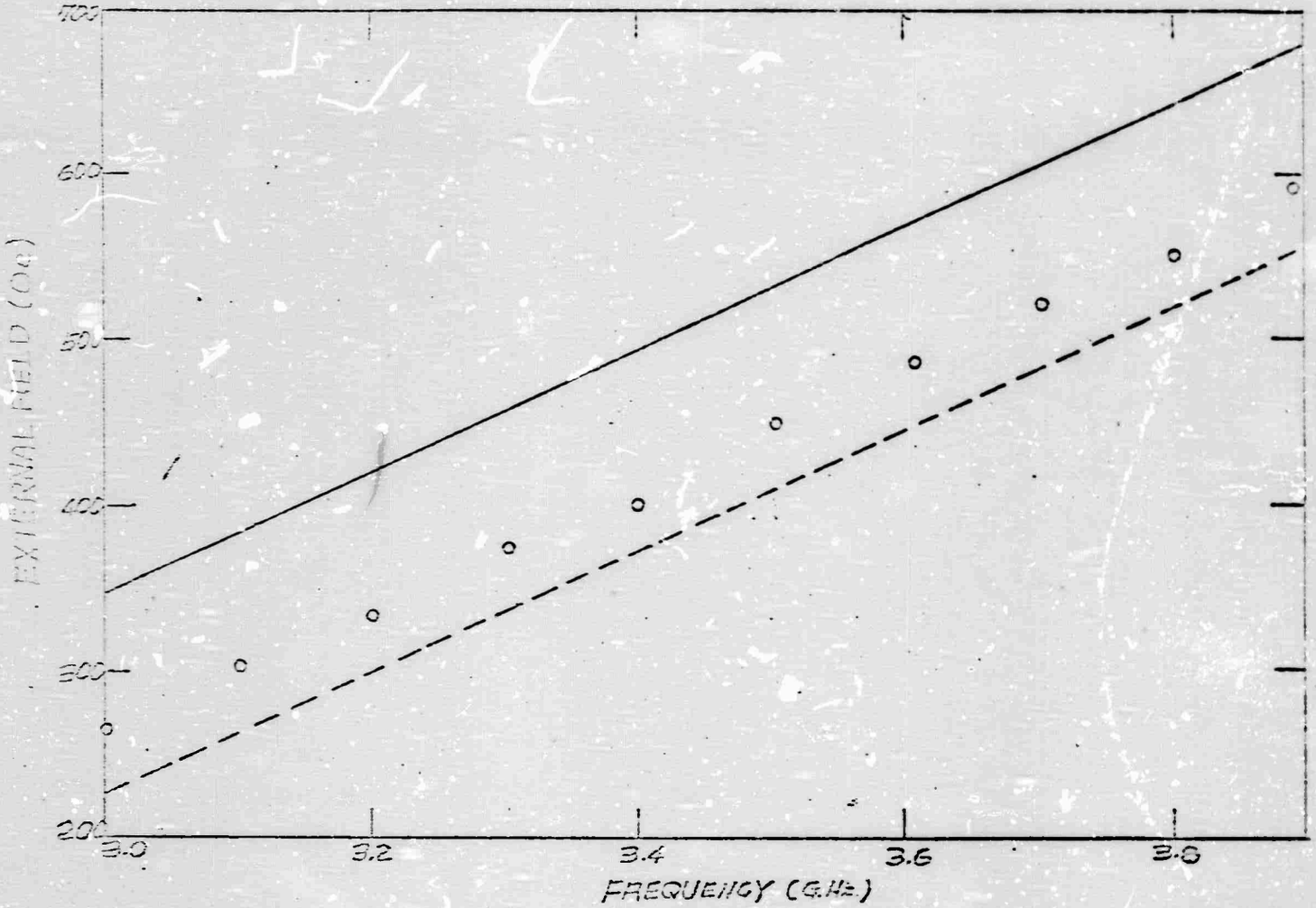

Fig. 3.7 Magnetostatic surface wave cut off fields for the sample 3 corresponding to maximum delay, at different frequencies. The external field is applied parallel to the slab surface.

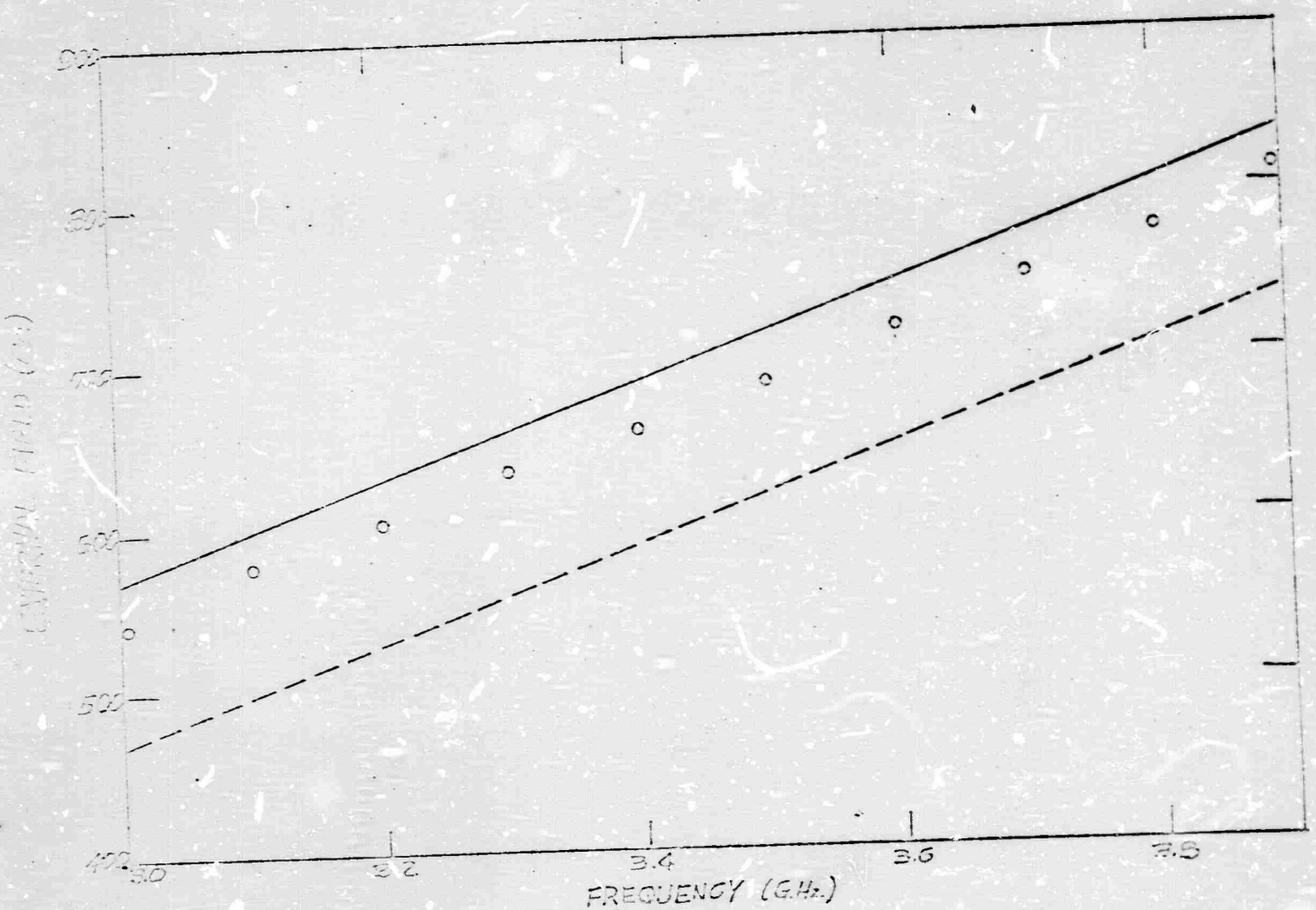

Fig. 3.8 90 degree magnetostatic volume wave cut off fields for the sample 3 corresponding to maximum delay at different frequencies. The external field is applied parallel to the slab surface.

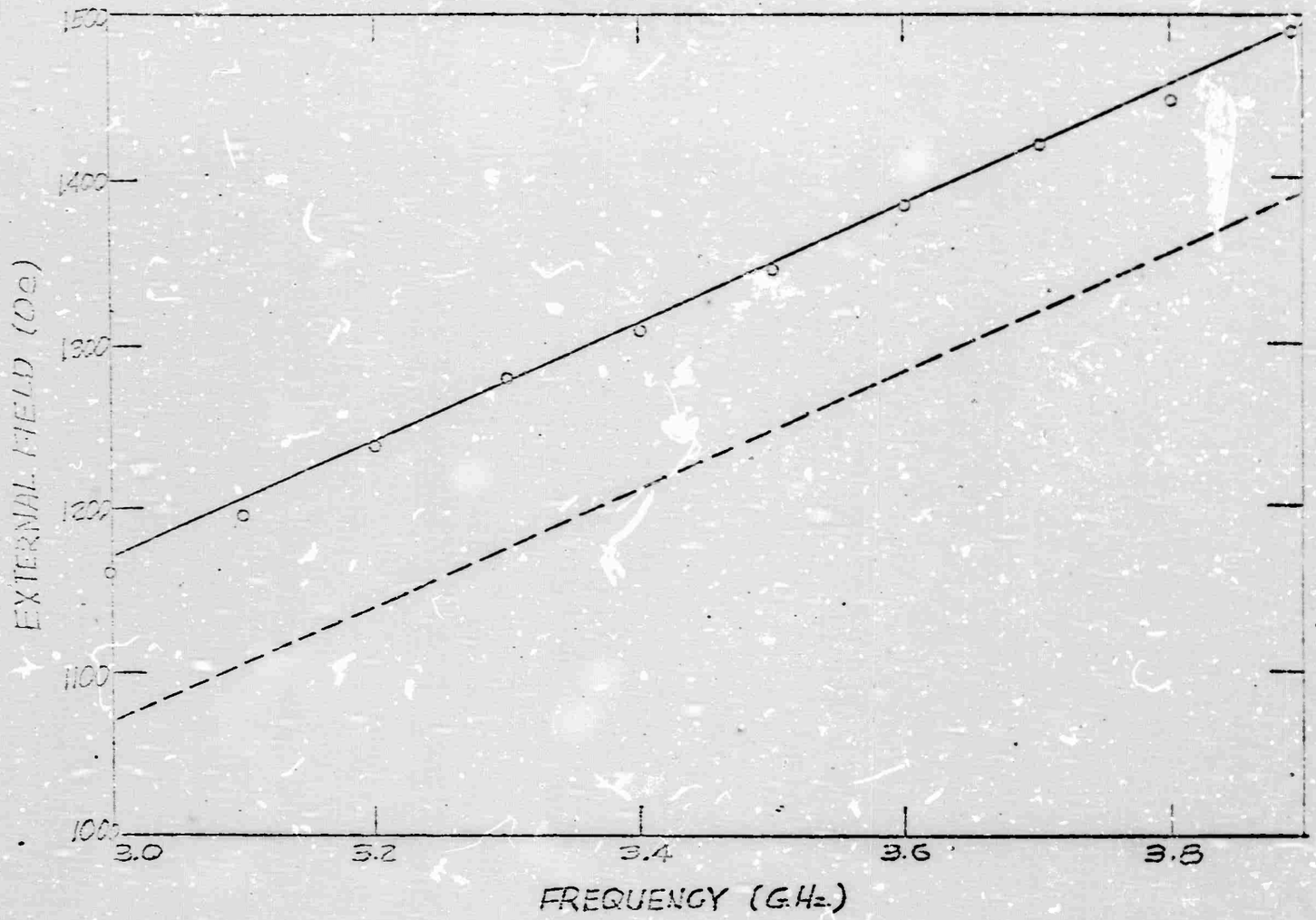

Fig. 3.9 0 degree magnetostatic volume wave cut off fields for the sample 3 at different frequencies. The external field is applied parallel to the slab surface.

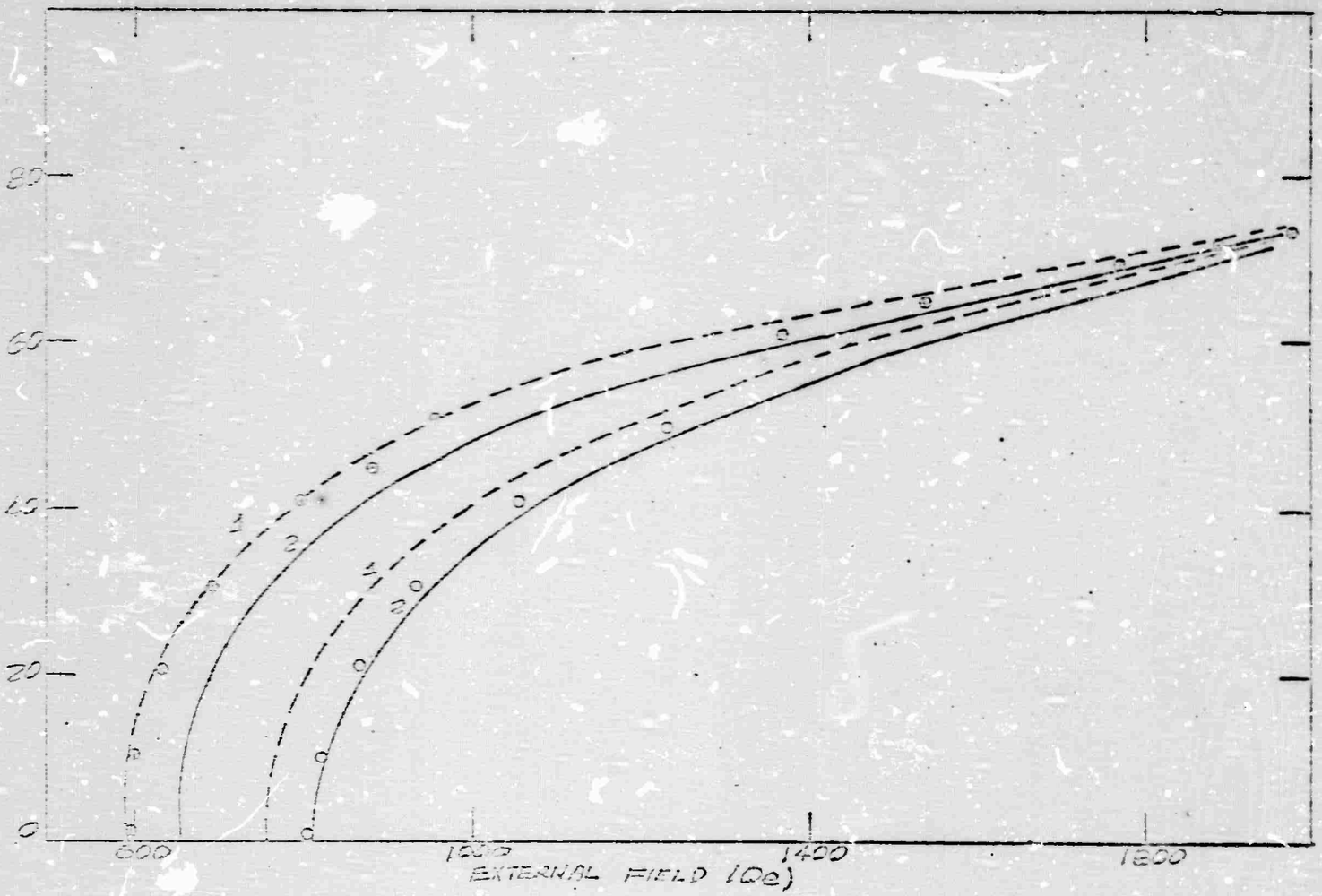

Fig. 3.10 Cut off fields of magnetostatic surface wave (e) and 90 degree volume wave (o) for the sample 3 at 3.9 G.HZ. The external field is applied at an angle with respect to the slab surface.

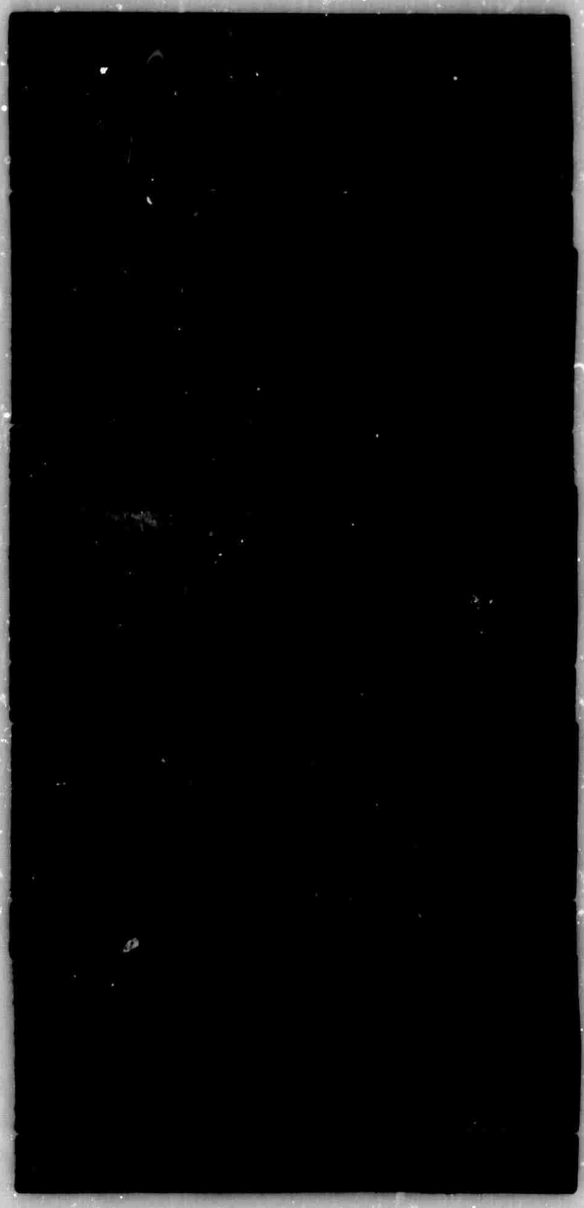

(a) H_o = 737Oe

(b) H_o = 575.1Oe

(c) H_o = 571.5Oe

(d) H_o = 568Oe

(e) H_o = 566.5Oe

Fig. 3.11 Delayed magnetostatic surface wave pulses at 3.9 G.Hz.. Experiments were done a 5x4x0.5mm single crystal YIG slab with an expernal magnetic field H_o applied parallel to the slab surface. (a) shows the transmitted signal with negligible delay time. Time scale = 0.2 μsec/cm.

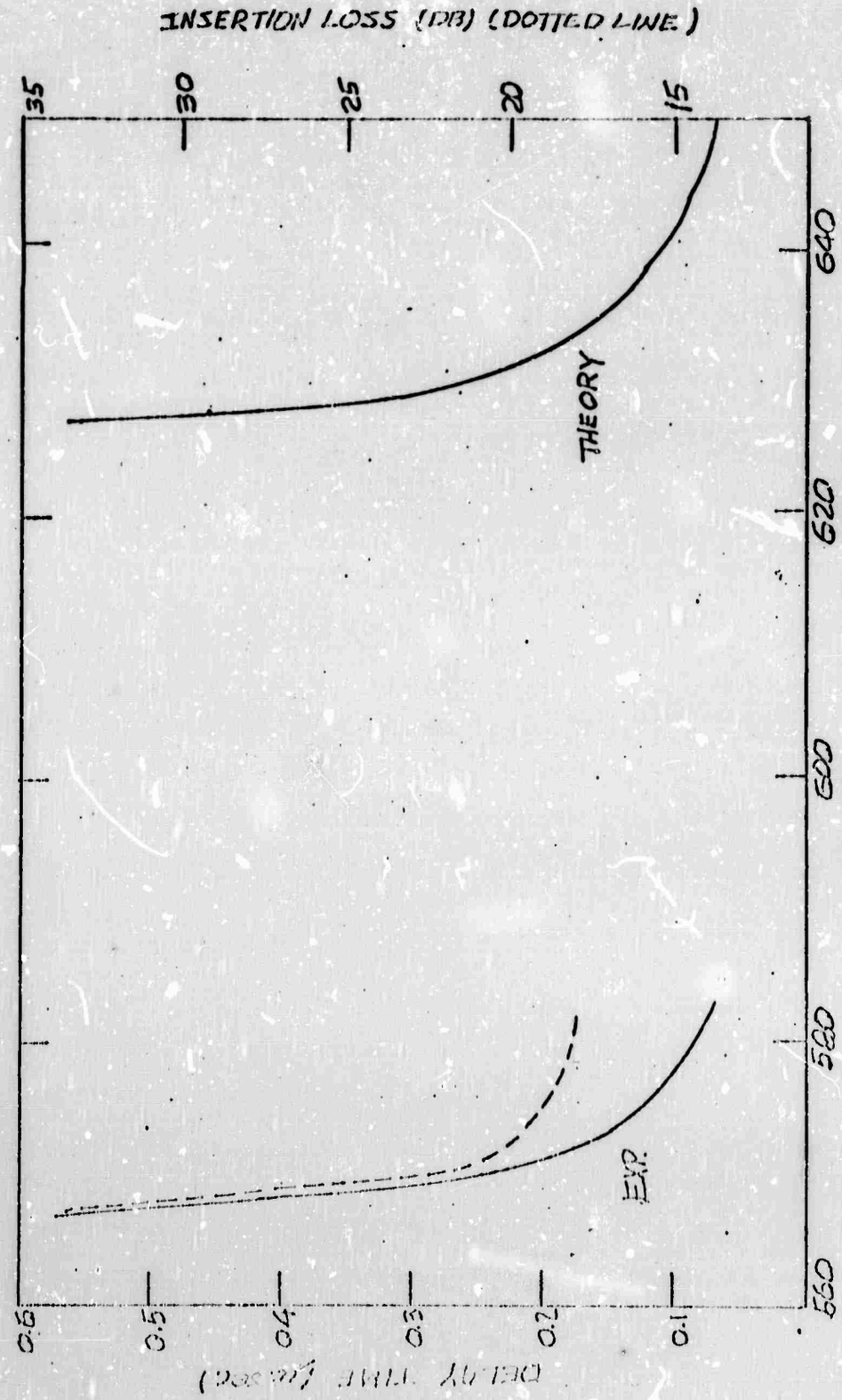

Fig. 3.12 Delay time of magnetostatic surface wave at 3.9 G.Hz. for the sample 2. The external field is applied parallel to the slab surface.

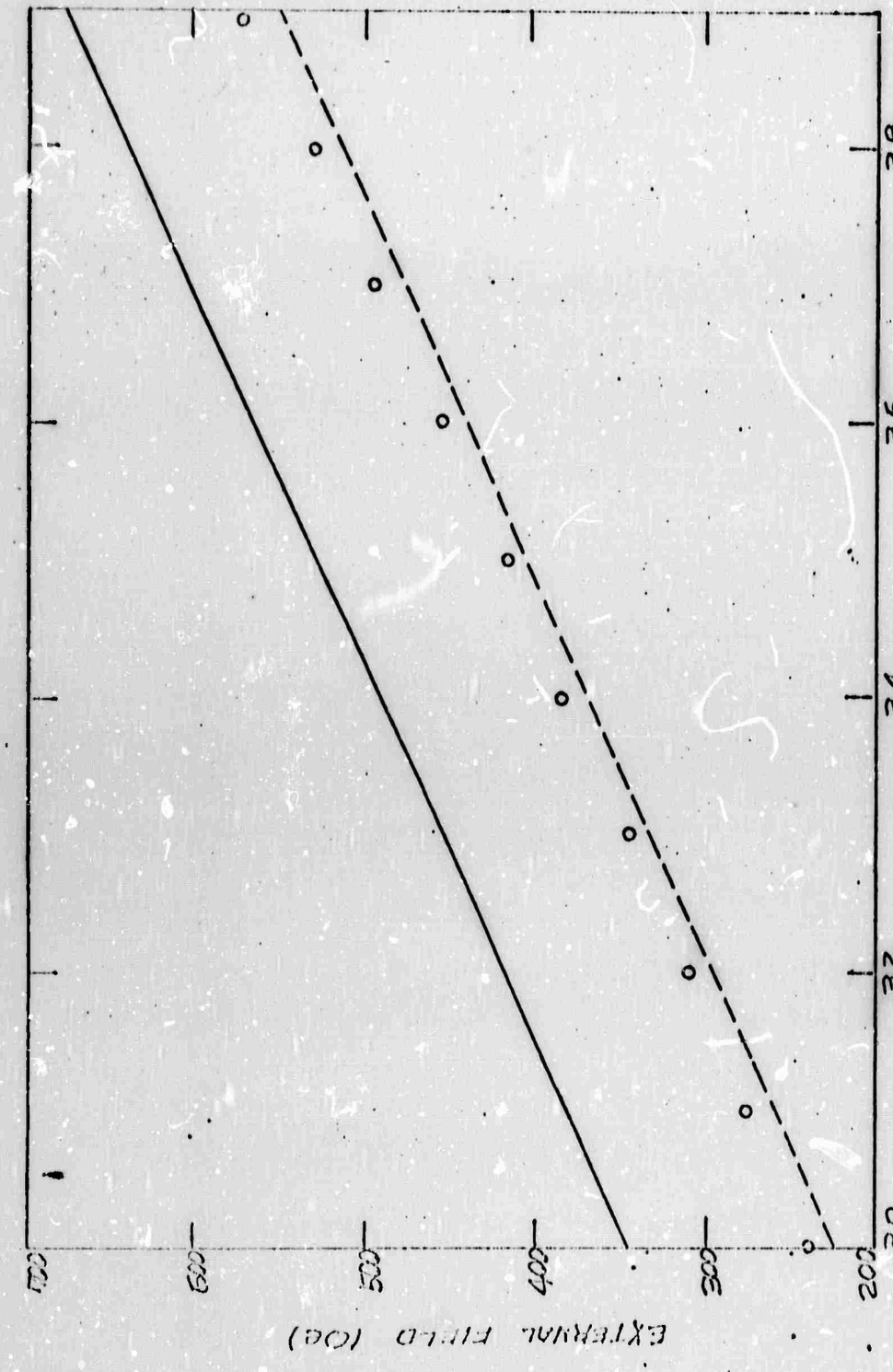

Fig. 3.13. Magnetostatic surface wave cut off fields for the sample 2 corresponding to maximum delay at different frequencies. The external field is applied parallel to the slab surface.

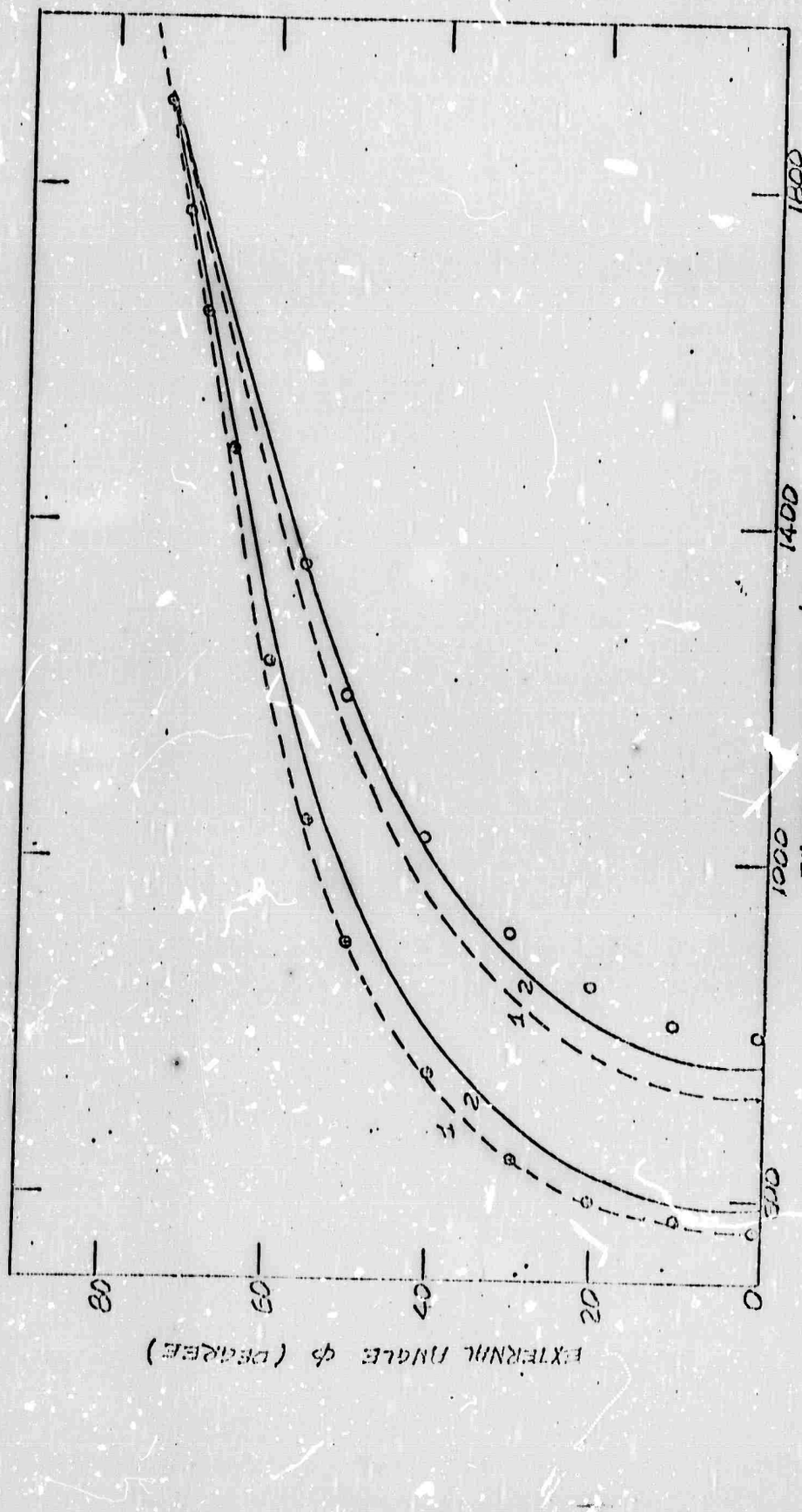

Fig. 3.24 Cut off fields of magnetostatic surface wave (⊕) and 90 degree volume wave (o) for the sample 3 at 3.9 G.HZ. The external field is applied at an angle with respect to the slab surface.

CONCLUSION

The unified normal mode approach, originally developed to study volume magnetostatic spin waves, is extended to the case of surface waves. It is shown that non-reciprocal surface modes exist in a transversely magnetized ferrite slab only when the frequency lie inside a well defined band above the famous volume mode manifold and when the medium is biased below a critical angle,90 degree volume waves, nevertheless always exist and therefore bridge the gap when the medium is nearly normally magnetized, under such condition no surface wave can be supported. Switching of surface modes by varying the magnetic bias direction appears possible although details have not yet been worked out.

Experimentally, non-reciprocal surface wave propagation was observed in a YIG single crystal slab. The slab was transversely magnetized in a arbirary direction and excited at 3.0 to 4.0 G.HZ. with fine wire antennas. For low frequency excitation the reaonance field is low, so there may be incomplete saturation of the sample. At high frequencies there will be large spin wave attenuations. The optimum choice of operating frequency is a compromise between these two limits. In our experiments, we usually observe clearer signals at high frequency and within S band (2.0 to 4.0 G.HZ.).

The surface wave propagating along a mechanically polished surface attenuates very quickly, due to the residual strain left on the surface. However, this thin strained layer can be removed by chemical polishing methods which can reduce the surface wave line width considerably.

The critical angle was observed to be about 50 to 55 degrees which corresponds an external field angle of about 70 to 80 degrees with respect to the slab surface. Therefore, to switch efficiently the surface

wave propagating along one surface to another we should need a switching field parallel to the slab surface with about 3000e peak to peak amplitude in addition to a DC perpendicular bias field.

It is also worthwhile to notice that surface waves merge smoothly into volume wave band arround that critical angle. So, properly biasing the ferrite slab, it will be possible to transfer the surface wave energy into volume wave energy and vise versa by providing a switching field.

It was reported recently that strong Bragg scattering of light from coherent spin waves at microwave frequency was observed in a YIG bar.[23] Because there is no reason why surface spin waves can not interact with light, it is expected that the light probing will definitely serve as a powerful tool to gather information which otherwise may not be obtainable.

APPENDIX A

DISPERSION RELATION OF SURFACE WAVES WITH ANISOTROPY FIELDS ADDED

In Chapter II, the dispersion relation is solved when both exchange and anisotropy fields are neglected. The neglect of the exchange field is justifiable when we operate in the magnetostatic region. On the other hand, the total anisotropic field is by no means small in practice compared to the total resonance field, especially when the DC magnetic field is biased to be parallel to the slab surface. Here a corrected formula is derived for semi-infinite medium. The geometry of the problem shown below corresponds to the YIG crystal used in all experiments discussed before.

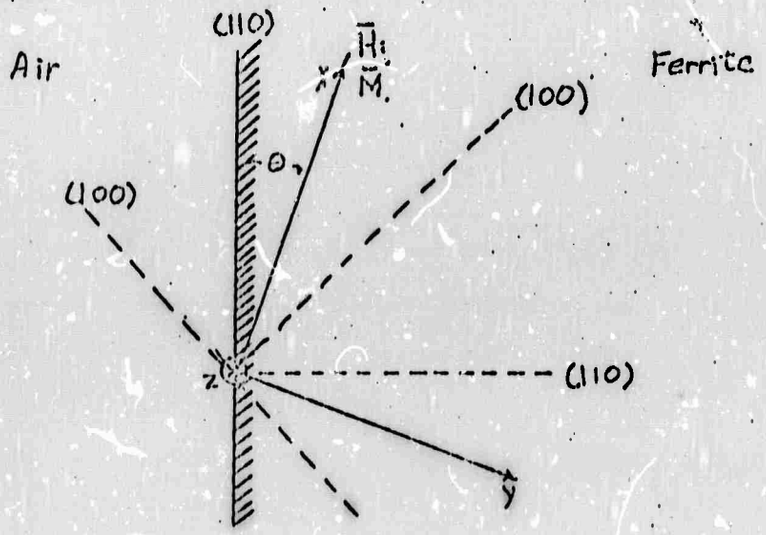

Fig. A.1

The DC as well as the small signal anisotropy field is related to $\bar{M}$ by a tensor operator. For the geometry given above they are

$$h_i^{an} = \sum_{j=2}^{3} N_{ij} m_j \qquad i = 2,3 \qquad \text{(A.1a)}$$

where $N_{33} = 0$ (A.1b)

$$N_{23} = N_{32} = 0 \tag{A.1c}$$

$$N_{22} = \frac{2K_1}{\mu_0 M^2}\left(-\frac{3}{2}\cos^2 2\Theta\right) \tag{A.1d}$$

$$H_1^{an} = \frac{2K_1}{\mu_0 M}\left(1 - \frac{1}{2}\cos^2 2\Theta\right) \tag{A.1e}$$

as given in p 150 in the reference [18]. Correspondence among indices and coordiate system are 1 ⟷ x, 2 ⟷ y, 3 ⟷ z. For YIG

$$\frac{2K_1}{M} = -80\ Oe$$

Considering Eq. (A.1) following replacements should be made in the equation of motion Eq. (2.2).

$$H_i \longrightarrow H_i + H_1^{an}$$

$$\bar{h} \longrightarrow \bar{h} + \bar{h}^{an}$$

Correspondingly, other equations in section 2.1 should be appropriately modified. The boundary condition Eq. (2.14) is changed to

$$m_y \cos\Theta\left(1 - N_{22}\frac{K_2+\alpha}{K_2}\right) = j\, m_z \tag{A.2}$$

Carrying out same procedure outlined in section 2.1 we get

$$\omega_k - (1-N_{22})\omega_0'\cos 2\Theta + \left\{\left[\omega_k - (1-2N_{22})\omega_0'\cos 2\Theta\right]^2 - 4\omega_0'\omega_m N_2(1-N_2)\cos^2\Theta\right\}^{1/2}$$
$$= 2\left\{\omega_k'' - \omega_0'\left[\omega_0' + \omega_m\cos^2\Theta + \omega_m N_{22}\sin^2\Theta\right]\right\} \tag{A.3}$$

where $$\omega_0' = -\gamma\mu_0(H_i + H_1^{an}) \tag{A.4}$$

This is the modified dispersion relation giving ω implicitly as a function of Θ, H_i, and the anisotropic parameter N_{22}.

APPENDIX B

RELATION BETWEEN INTERNAL AND EXTERNAL FIELD ANGLE IN THE TRANSVERSE PLANE OF A FERRITE SLAB

Consider the following geometry used in experiments.

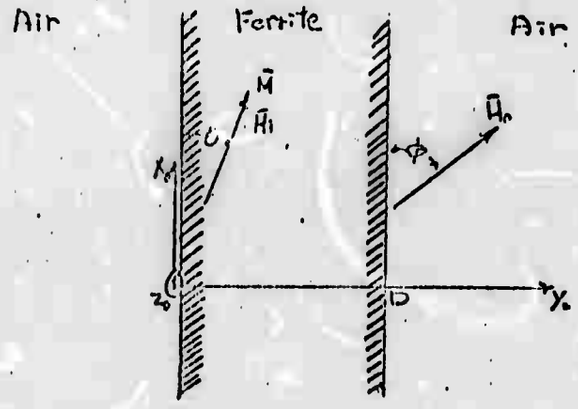

Fig. B.1

Because of geometrical demagnetizing fields, the internal and the external field will not be aligned along the same direction. For an ellipsoidal sample

$$\bar{H}_{demag} = \bar{\bar{N}}^a \cdot \bar{M} \tag{B.1}$$

where

$$\bar{\bar{N}} = \begin{bmatrix} N^a_{y_0}, & 0, & 0 \\ 0, & N^a_{x_0}, & 0 \\ 0, & 0, & N^a_{z_0} \end{bmatrix} \tag{B.2}$$

and

$$N^a_{x_0} + N^a_{y_0} + N^a_{z_0} = 1 \tag{B.3}$$

If a ferrite slab is infinite in X_0, and Z_0 direction, then

$$N^a_{y_0} = 1 \; ; \quad N^a_{x_0} = N^a_{z_0} = 0$$

But for a finite slab, Eqs. (B.1) and (B.2) still approximately apply

with suitably chosen N_x^a and N_y^a . In that case,

$$H_o \sin\phi = (H_i + N_{x_o}^a M)\sin\theta$$
$$H_o \cos\phi = (H_i + N_{x_o}^a M)\cos\theta \qquad (B.4)$$

Note in Eqs. (B.4) we have ignored the fact that for $N_{y_o}^a \neq 0$, $\bar{M}$ and $\bar{H}_i$ are no longer aligned either. For the case $N_{x_o}^a = N_{z_o}^a = 0$; $N_{y_o}^a = 1$, functional relations among parameters in Eqs. (B.4) are plotted in Figs. (B.2), and (B.3) for reference.

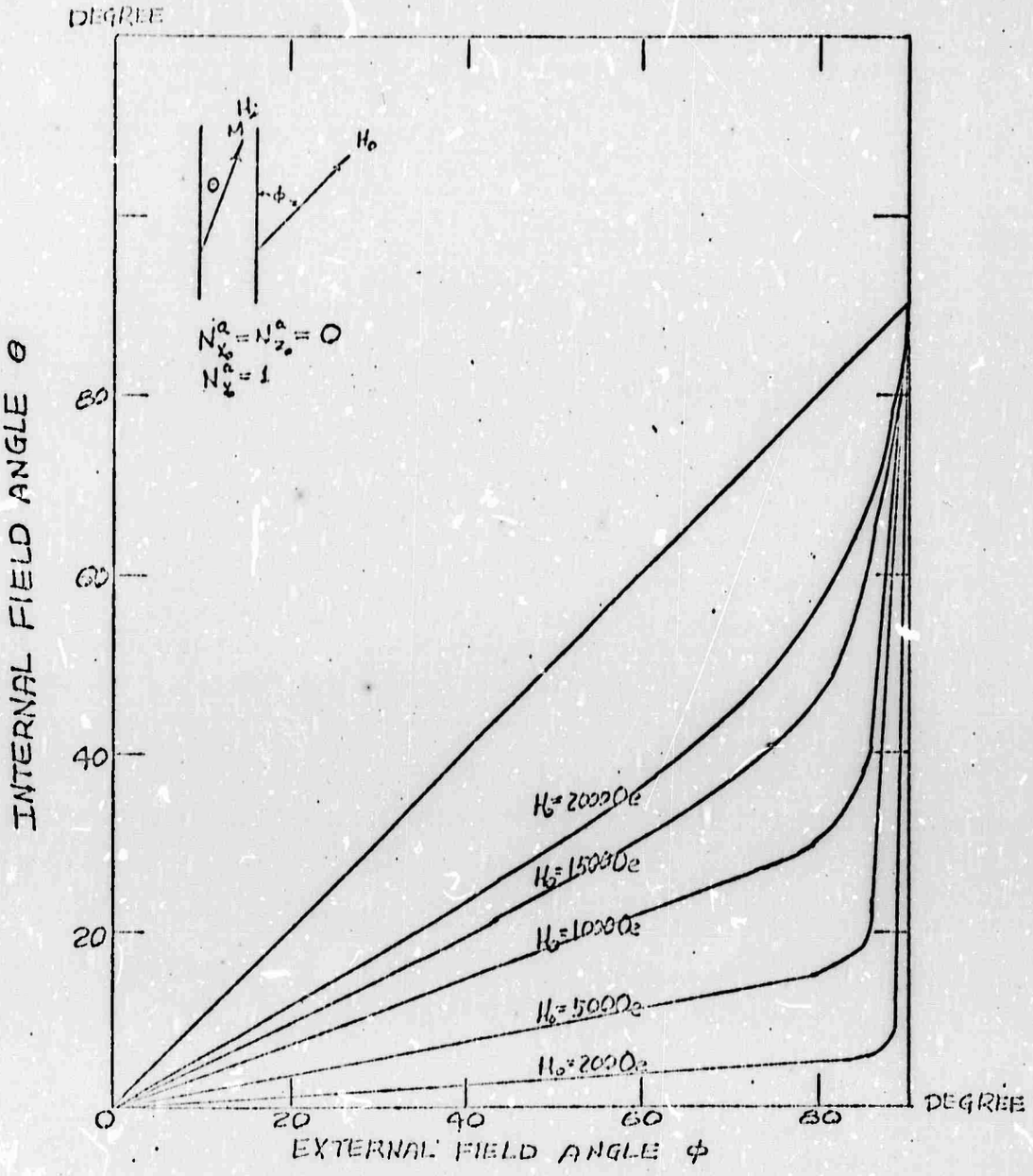

Fig. B.2 Relation of external field angle ϕ and the internal field angle θ relative to the ferrite slab plane.

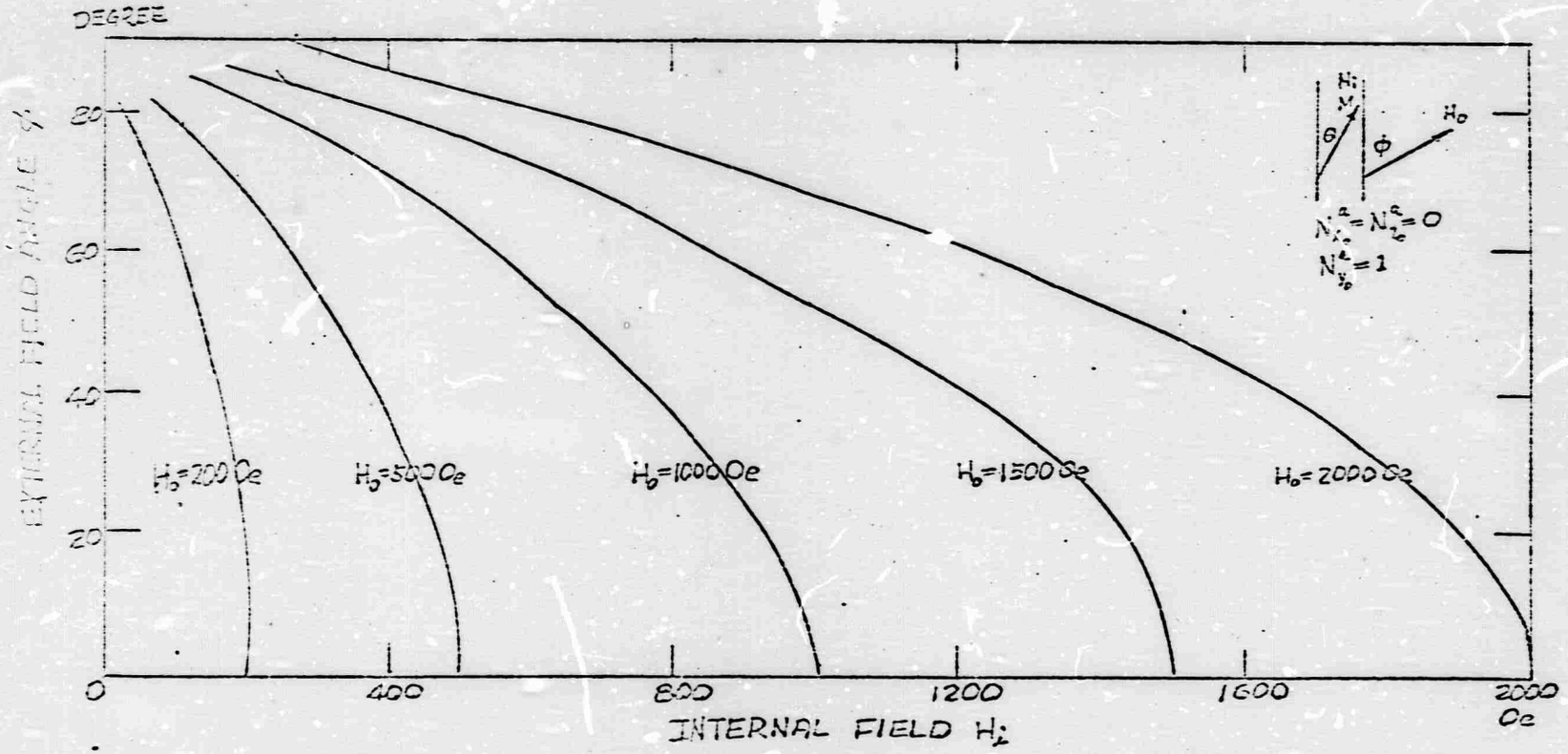

Fig. B.3 Relation of internal field Hi with the external field angle ϕ .

APPENDIX C

MATHEMATICAL TREATMENT OF SURFACE MODES SUPPORTED BY A SEMI-INFINITE FERRITE MEDIUM

This appendix serves as a supplement of section 2.1. Many mathematical relations leading to the results discussed in that section are given in detail. The geometry of the problem is shown in Fig. 2.1. The relation between the two systems of coordinates (x_o, y_o, z_o) and (x, y, z) is

$$\begin{bmatrix} x_o \\ y_o \\ z_o \end{bmatrix} = \begin{bmatrix} \cos\Theta, -\sin\Theta, 0 \\ \sin\Theta, \cos\Theta, 0 \\ 0, 0, 1 \end{bmatrix} \begin{bmatrix} x \\ y \\ z \end{bmatrix} \qquad (C.1)$$

The torque equation for ferrite, when explicitly expressed in (x, y, z) coordinate system is

$$\begin{aligned} m_x &= 0 \\ \dot{m}_y &= -\omega_o m_z + \omega_m h_z \\ \dot{m}_z &= \omega_o m_y - \omega_m h_y \end{aligned} \qquad (C.2)$$

Within the magnetostatic approximation, the dipolar field and the magnetostatic potential satisfy

$$\bar{h} = \nabla\phi \qquad (C.3)$$

and

$$\nabla^2\phi = 0 \qquad \text{for } y_o < 0 \qquad (C.4a)$$

$$\nabla^2\phi = -\nabla\cdot\bar{m} \qquad \text{for } y_o > 0 \qquad (C.4b)$$

The plane wave solution we are looking for takes the following form

$$\Phi = Re\left[-j\frac{\bar{k}_f\cdot\bar{m}_f}{k_f^2}\,e^{-j\bar{k}_f\cdot\bar{r}}\right] \qquad \text{for } y_0>0 \qquad \text{(C.5a)}$$

$$\bar{h} = Re\left[-\bar{k}_f\frac{\bar{k}_f\cdot\bar{m}_f}{k_f^2}\,e^{-j\bar{k}_f\cdot\bar{r}}\right] \qquad \text{for } y_0>0 \qquad \text{(C.5b)}$$

where

$$\begin{aligned}\bar{k}_f &= -j\alpha\,\bar{i}_{y_0} + k_z\,\bar{i}_{z_0} \\ &= -j\alpha\sin\theta\,\bar{i}_x + (-j\alpha)\cos\theta\,\bar{i}_y + k_z\,\bar{i}_z\end{aligned} \qquad \text{(C.6)}$$

and α , k_z , ω are constrained by a relation given later.

For the air region, continuities of Φ and h_z require that

$$\Phi = Re\left[-j\frac{\bar{k}_a\cdot\bar{m}_a}{k_a^2}\,e^{-j\bar{k}_a\cdot\bar{r}}\right] \qquad \text{for } y_0<0 \qquad \text{(C.7a)}$$

$$\bar{h} = Re\left[-\bar{k}_a\frac{\bar{k}_a\cdot\bar{m}_a}{k_a^2}\,e^{-j\bar{k}_a\cdot\bar{r}}\right] \qquad \text{for } y_0<0 \qquad \text{(C.7b)}$$

where

$$\begin{aligned}\bar{k}_a &= -k_y^o\,\bar{i}_{y_0} + \bar{k}_z\,\bar{i}_{z_0} \\ &= -k_y^o\sin\theta\,\bar{i}_x - k_y^o\cos\theta\,\bar{i}_y + k_z\,\bar{i}_z\end{aligned} \qquad \text{(C.8)}$$

because of Eq. (C.4a), we have

$$k_y^{o\,2} + k_z^2 = 0 \qquad \text{(C.9a)}$$

without loss of generality, we will choose

$$k_y^o = j\,k_z \qquad \text{(C.9b)}$$

To make $\bar{h}$ in (C.7) decay in $-y_o$ direction, k_x must have negative real part. The reason for this choice will become clear later. Together with Eqs. (C.1), (C.5b), (C.7b) and (C.9b), the boundary condition on $y_o = 0$

$$(\bar{h} + \bar{m}) \cdot \bar{i}_x \Big|_{y_o = 0_+} = \bar{h} \cdot \bar{i}_{y_o} \Big|_{y_o = 0_-} \tag{C.10}$$

takes the following form

$$\underline{m}_y \cos\theta = j \underline{m}_z \tag{C.11}$$

The contraint (2.14) selects from among all normal modes in the infinite medium those that can exist in the geometry shown in Fig. 2.1. ; it also determines the dispersion relation. Normal modes in the semi-infinite medium can be obtained by substituting (C.5b) into (C.2). After some algebra, we find

$$\begin{bmatrix} \underline{m}_y \\ \underline{m}_z \end{bmatrix} = \begin{bmatrix} -G & , & -E \\ F & , & G \end{bmatrix} \begin{bmatrix} \underline{m}_y \\ \underline{m}_z \end{bmatrix} \tag{C.12}$$

where

$$E = \omega_o + \omega_m \frac{k_z}{k_f^2} \tag{C.13a}$$

$$F = \omega_o - \omega_m \frac{\alpha^2 \cos^2\theta}{k_f^2} \tag{C.13b}$$

$$G = -j \omega_m \cos\theta \frac{\alpha k_f}{k_f^2} \tag{C.13c}$$

$$k_f^2 = k_z^2 - \alpha^2 \tag{C.13d}$$

In order to diagonalze (C.12), define

$$\begin{bmatrix} m_1 \\ m_2 \end{bmatrix} = \frac{1}{2jE(F\omega_k)^{1/2}} \begin{bmatrix} G-j\omega_k & , & E \\ -G-j\omega_k & , & -E \end{bmatrix} \begin{bmatrix} m_y \\ m_z \end{bmatrix} \tag{C.14}$$

Thus

$$\begin{bmatrix} m_y \\ m_z \end{bmatrix} = F^{1/2} \begin{bmatrix} -E & , & E \\ G+j\omega_k & , & G-j\omega_k \end{bmatrix} \begin{bmatrix} m_1 \\ m_2 \end{bmatrix} \tag{C.15}$$

With this transformation, (C.12) is reduced to

$$\begin{bmatrix} \dot{m}_1 \\ \dot{m}_2 \end{bmatrix} = \begin{bmatrix} j\omega_k & , & 0 \\ 0 & , & -j\omega_k \end{bmatrix} \begin{bmatrix} m_1 \\ m_2 \end{bmatrix} \tag{C.16}$$

where

$$\omega_k = (EF-G)^{1/2} = \left[\omega_0^2 + \omega_s\omega_m \frac{k_z^2 - \alpha^2\cos^2\theta}{k_z^2 - \alpha^2}\right] \tag{C.17}$$

or equivalently,

$$\alpha = \pm \left[\frac{\omega_k^2 - \omega_0^2 - \omega_s\omega_m}{\omega_k^2 - \omega_0^2 - \omega_s\omega_m\cos^2\theta}\right]^{1/2} |k_z| \tag{C.18}$$

The constant α is real only when ω_k is large than $[\omega_0^2+\omega_s\omega_m]^{1/2}$. Eqs. (C.16) implies two normal modes solutions in a semi-infinite ferrite medium, they are

$$\begin{bmatrix} m_1 \\ m_2 \end{bmatrix} = \begin{bmatrix} m_{10} \\ 0 \end{bmatrix} e^{j\omega_k t} \tag{C.19a}$$

and

$$\begin{bmatrix} m_1 \\ m_2 \end{bmatrix} = \begin{bmatrix} 0 \\ m_{20} \end{bmatrix} e^{-j\omega_k t} \tag{C.19b}$$

We substitute Eqs. (C.19a), (C.15) into Eq. (C.11). The first mode implies:

$$\omega_k = \left(\omega_0 + \omega_m \frac{k_z}{k_z - \alpha} \right) \cos\Theta \tag{C.20}$$

Together with Eq. (C.17) the dispersion relation

$$\omega_k = \frac{\omega_0 + \omega_m}{2} \cos\Theta + \frac{\omega_0}{2\cos\Theta} \tag{C.21}$$

subject to the constraint

$$\frac{k_z + \alpha}{k_z - \alpha} = \frac{\omega_0}{\omega_m} \tan^2\Theta \tag{C.22}$$

The second mode cannot satisfy Eq. (C.11). But it can be shown that it is the surface eigenmode propagating in positive z direction along $y_0 = 0$ surface shown in Fig. 2.1, if $y_0 < 0$ region is filled with ferrite while $y_0 > 0$ region is free space. In that case the boundary condition (C.11) instead becomes

$$m_y \cos\Theta = -j m_z \tag{C.23}$$

APPENDIX D

MATHEMATICAL TREATMENT OF NORMAL MODES SUPPORTED BY A FINITE FERRITE SLAB

This appendix serves as a supplement of section 2.2. Mathematical procedures used follow closely those in Appendix C.

For a given ferrite slab magnetized in an arbitrary transverse direction, the plane wave solutions of the potential equation (C.4) in the ferrite region $0 \le y_0 \le D$ are

$$\bar{m} = Re\left\{\left[\bar{m}_f e^{-\alpha y_0} + \bar{m}_r e^{\alpha(y_0-D)}\right] e^{-jk_z z_0}\right\} \tag{D.1a}$$

$$\Phi = Re\left\{\left[-j\frac{\bar{k}_f\cdot\bar{m}_f}{k_f^2} e^{-\alpha y_0} - j\frac{\bar{k}_r\cdot\bar{m}_r}{k_r^2} e^{\alpha(y_0-D)}\right] e^{-jk_z z_0}\right\} \tag{D.1b}$$

$$\bar{h} = Re\left\{\left[-\bar{k}_f\frac{\bar{k}_f\cdot\bar{m}_f}{k_f^2} e^{-\alpha y_0} - \bar{k}_r\frac{\bar{k}_r\cdot\bar{m}_r}{k_r^2} e^{\alpha(y_0-D)}\right] e^{-jk_z z_0}\right\} \tag{D.1c}$$

where we define

$$\bar{k}_f = -j\alpha\bar{i}_{y_0} + k_z\bar{i}_z \tag{D.2a}$$
$$= -j\alpha\sin\Theta\,\bar{i}_x - j\alpha\cos\Theta\,\bar{i}_y + k_z\bar{i}_z$$

$$\bar{k}_r = j\alpha\bar{i}_{y_0} + k_z\bar{i}_z \tag{D.2b}$$

Note that

$$k_f^2 = k_r^2$$

For the air region $y_0 < 0$,

$$\Phi = Re\left\{\left[-j\frac{\bar{k}_f\cdot\bar{m}_f}{k_f^2} - j\frac{\bar{k}_r\cdot\bar{m}_r}{k_r^2} e^{-\alpha D}\right] e^{jk_y^a y} e^{-jk_z z_0}\right\} \tag{D.3a}$$

$$\bar{h} = Re\left\{\left[-\bar{k}^a\left(\frac{\bar{k}_f\cdot\bar{m}_f}{k_f^2} + \frac{\bar{k}_r\cdot\bar{m}_r}{k_r^2} e^{-\alpha D}\right)\right] e^{jk_y^a y} e^{-jk_z z_0}\right\} \tag{D.3b}$$

where

$$\bar{k}_a^f = -k_y^o \bar{i}_y + k_z \bar{i}_z \tag{D.4}$$

For the air region $y_o > D$,

$$\varphi = Re\left\{\left[-j\frac{\bar{k}_f \cdot \bar{m}_f}{k_f^2} e^{-\alpha D} - j\frac{\bar{k}_r \cdot \bar{m}_r}{k_r^2}\right] e^{-jk_y^o(y_o - D)} e^{-jk_z z}\right\} \tag{D.5a}$$

$$\bar{h} = Re\left\{-k_a^f\left[\frac{\bar{k}_f \cdot \bar{m}_f}{k_f^2} e^{-\alpha D} + \frac{\bar{k}_r \cdot \bar{m}_r}{k_r^2}\right] e^{-jk_y^o(y_o - D)} e^{-jk_z z}\right\} \tag{D.5b}$$

where

$$k_a^f = k_y^o \bar{i}_y + k_z \bar{i}_z \tag{D.6}$$

Note

$$k_y^{o2} + k_z^2 = 0 \tag{D.7a}$$

$$k_y^o = j k_z \tag{D.7b}$$

The propagation constant k_z is negative as before.

Use Eqs. (D.1a), (D.1c), (D.3b), (D.7b), continuities of magnetic flux across $y_o = 0$, and $y_o = D$ surfaces give two constraints.

On $y_o = 0$ surface we have

$$(k_z - \alpha)(m_{fy}\cos\theta - j m_{fz}) + (k_z + \alpha)(m_{ry}\cos\theta - j m_{rz}) e^{-\alpha D} = 0 \tag{D.8a}$$

On $y_o = D$ surface we have

$$(k_z + \alpha)(m_{fy}\cos\theta + j m_{fz}) e^{-\alpha D} + (k_z - \alpha)(m_{ry}\cos\theta + j m_{rz}) = 0 \tag{D.8b}$$

Inside the ferrite medium, the torque equation (C.2) applies

separately to the forward and the reflected wave. Replacing α by $-\alpha$, G by -G for reflected wave, Eqs. (C.14), (C.15) and (C.16) then lead to

$$\begin{bmatrix} \dot{m}_{fy} \\ \dot{m}_{fz} \\ \dot{m}_{ry} \\ \dot{m}_{rz} \end{bmatrix} = \begin{bmatrix} -G, & E, & 0, & 0 \\ F, & G, & 0, & 0 \\ 0, & 0, & G, & -E \\ 0, & 0, & F, & -G \end{bmatrix} \cdot \begin{bmatrix} m_{fy} \\ m_{fz} \\ m_{ry} \\ m_{rz} \end{bmatrix} \qquad (D.9)$$

With

$$\begin{bmatrix} m_{f1} \\ m_{f2} \\ m_{r1} \\ m_{r2} \end{bmatrix} = \frac{1}{2jE(F\omega_k)^{1/2}} \begin{bmatrix} G-j\omega_k, & E, & 0, & 0 \\ -G-j\omega_k, & -E, & 0, & 0 \\ 0, & 0, & -G-j\omega_k, & E \\ 0, & 0, & G-j\omega_k, & -E \end{bmatrix} \cdot \begin{bmatrix} m_{fy} \\ m_{fz} \\ m_{ry} \\ m_{rz} \end{bmatrix} \qquad (D.10a)$$

and

$$\begin{bmatrix} m_{fy} \\ m_{fz} \\ m_{ry} \\ m_{rz} \end{bmatrix} = F^{1/2} \begin{bmatrix} -E, & -E, & 0, & 0 \\ -G+j\omega_k, & G-j\omega_k, & 0, & 0 \\ 0, & 0, & -E, & -E \\ 0, & 0, & -G+j\omega_k, & -G-j\omega_k \end{bmatrix} \cdot \begin{bmatrix} m_{f1} \\ m_{f2} \\ m_{r1} \\ m_{r2} \end{bmatrix} \qquad (D.10b)$$

we get finally

$$\begin{bmatrix} \dot{m}_{f1} \\ \dot{m}_{f2} \\ \dot{m}_{r1} \\ \dot{m}_{r2} \end{bmatrix} = \begin{bmatrix} j\omega_k, & 0, & 0, & 0 \\ 0, & -j\omega_k, & 0, & 0 \\ 0, & 0, & j\omega_k, & 0 \\ 0, & 0, & 0, & -j\omega_k \end{bmatrix} \cdot \begin{bmatrix} m_{f1} \\ m_{f2} \\ m_{r1} \\ m_{r2} \end{bmatrix} \qquad (D.11)$$

Where ω_k is given in Eq. (C.17) and E, F, G are defined in (C.13).

There are two modes possible decoupled in a medium uniform both in time and space.

The first mode corresponds to

$$\begin{bmatrix} m_{f1} \\ m_{f2} \\ m_{r1} \\ m_{r2} \end{bmatrix} = \begin{bmatrix} A_{f1} \\ 0 \\ A_{r1} \\ 0 \end{bmatrix} e^{j\omega_k t} \qquad \text{(D.12)}$$

Upon substitution Eqs. (D.12), (D.10) into the boundary condition (D.9), we have two coupled equations.

$$A_{f1}\left[(k_z-\alpha)(\omega_k-\omega_0\cos\theta)-k_z\omega_m\cos\theta\right] \qquad \text{(D.13a)}$$
$$+A_{r1}\left[(k_z+\alpha)(\omega_k-\omega_0\cos\theta)-k_z\omega_m\cos\theta\right]e^{-\alpha D}=0$$

$$A_{f1}\left[(k_z+\alpha)(\omega_k+\omega_0\cos\theta)+k_z\omega_m\cos\theta\right]e^{-\alpha D} \qquad \text{(D.13b)}$$
$$+A_{r1}\left[(k_z-\alpha)(\omega_k+\omega_0\cos\theta)+k_z\omega_m\cos\theta\right]=0$$

Set the determinant of Eq. (D.13) equal to zero, then together with Eq. (C.17) the dispersion relation can be shown to be

$$\left[(1+\chi)(1+\chi\cos^2\theta)-\frac{\omega_m^2}{\omega_0^2}\chi^2\cos^2\theta+1\right]\tanh\alpha D \qquad \text{(D.14a)}$$
$$=-2\frac{k_z}{|k_z|}\left[(1+\chi)(1+\chi\cos^2\theta)\right]^{1/2}$$

The susceptibility χ is defined in Eq. (1.9a) by putting

Explicitly Eq. (D.14a) becomes

$$\left[\omega_m^2\cos^2\theta+\omega_0\omega_m(1+\cos^2\theta)-2(\omega_k^2-\omega_0^2)\right]\tanh\alpha D \qquad \text{(D.14b)}$$
$$=2\left[(\omega_k^2-\omega_0^2-\omega_0\omega_m)(\omega_k^2-\omega_0^2-\omega_0\omega_m\cos\theta)\right]^{1/2}$$

or

$$\omega_k^2=\omega_0^2+\omega_0\omega_m\left(\frac{1+\cos^2\theta}{2}\right)$$
$$+\frac{-\omega_0^2\cos^2\theta+\omega_m\coth\alpha D\left[\omega_0^2\sin^4\theta(\coth^2\alpha D-1)+\omega_m^2\cos^2\theta\right]^{1/2}}{2(\coth^2\alpha D-1)} \qquad \text{(D.14c)}$$

To ensure surface mode solution, α must be positive real, so

$$\omega_m^2 \cos^2\theta + \omega_0 \omega_m (1+\cos^2\theta) - 2(\omega_k^2 - \omega_0^2) \geq 0 \qquad \text{(D.15)}$$

Combining Eqs. (D.14c) and (D.15) gives the condition that the surface wave solutions exists only is

$$1 \geq |\cos\theta| \geq \left[\frac{\omega_0}{\omega_0+\omega_m}\right]^{1/2} \qquad \text{(D.16)}$$

Ratios of all field quantities involved can easily be solved from Eqs. (D.10b) and (D.13). They are

$$\frac{m_{fy}}{m_{fz}} = j\,\frac{\omega_0(k_z^2-\alpha^2) + \omega_m k_z^2}{\omega_k(k_z^2-\alpha^2) - \omega_m \cos\theta\, k_z \alpha} \qquad \text{(D.17a)}$$

$$\frac{m_{ry}}{m_{rz}} = j\,\frac{\omega_0(k_z^2-\alpha^2) + \omega_m k_z^2}{\omega_k(k_z^2-\alpha^2) + \omega_m \alpha k_z \cos\theta} \qquad \text{(D.17b)}$$

$$\frac{B_m}{B_{f1}} = -\frac{k_z[\omega_k + (\omega_0+\omega_m)\cos\theta] + \alpha(\omega_k + \omega_0\cos\theta)}{k_z[\omega_k + (\omega_0+\omega_m)\cos\theta] - \alpha(\omega_k + \omega_0\cos\theta)} e^{-\alpha D} \qquad \text{(D.17c)}$$

The second mode that can be supported by the ferrite slab is

$$\begin{bmatrix} m_{f1} \\ m_{f2} \\ m_{r1} \\ m_{r2} \end{bmatrix} = \begin{bmatrix} 0 \\ B_{f2} \\ 0 \\ B_{r2} \end{bmatrix} e^{-j\omega_k t} \qquad \text{(D.18)}$$

Eqs. (D.17) apply directly to the second mode with proper modification, ie., change α to $-\alpha$, ω_k to $-\omega_k$, and index 1 to 2. The dispersion relation (D.14) is valid in both cases.

REFERENCES

1. B. A. Auld, J. H. Collins and D. C. Webb, "Excitation of Magnetoelastic Waves in YIG Delay Lines", J. of Appl. Phy. 39, 1598(1968).

2. R. W. Damon and J. R. Eshbach, "Magnetostatic Modes of a Ferromagnet Slab", J. Phys. Chem. Solids 19, 308(1961).

3. J. R. Eshbach and R. W. Damon, "Surface Magnetostatic Modes and Surface Spin Waves", Phy. Rev. 118, 1208(1960).

4. L. K. Brundle and N. J. Freedman, "Magnetostatic Surface Waves on a Y.I.G. Slab", Elec. Lett. 4, 132(1968).

5. W. L. Bongiami, J. H. Collins, F. A. Pizzarello and D. A. Wilson, "Propagating Magnetic Waves in Epitaxial YIG:, 1969 G-MTT Symposium Digest 376.

6. F. R. Morgenthaler, "A Nonreciprocal Magnetostatic Surface Wave Independently Controllable Propagation and Delay Constants", J. of Appl. Phy. 41, 1041(1970).

7. F. R. Morgenthaler, "Magnetic Control of Exchange Torques and the Penetration Depth of Magnetostatic Surface Spin Waves", Presented at the 1970 International Conference on Magnetism, Grenoble, France, Sept. 1970.

8. J. L. Doane, "Reflection and Transmission Coefficients in Multi-Wave Inforogeneous Media", Technical Report 22, Microwave and Quantum Magnetics Group, M. I. T. (1970).

9. S. M. Rezende, Magnetoelastic and Magnetostatic Waves in Time Varying Magnetic Fields", Technical Report 19, Microwave and Quantum Magnetics Group, M.I.T.(1967).

10. E. Schlomann and R. I. Joseph, "Generation of Spin Waves in Nonuniform Magnetic Fields, I. Conversion of Electromagnetic Power into Spin-Wave Power and Vice Versa, II. Calculation of the Coupling Length", J. of Appl. Phy. 35, 159(1964).

11. E. Schlomann, R. I. Joseph and T. Kohane, "Generation of Spin Waves in Nonuniform Fields, with Application to Magnetic Delay Lines", Proc. of the IEEE 53, 1495(1965).

12. W. Strauss, :Elastic and Magnetoelastic Waves in Yttrium Iron Garnet", Proc. of the IEEE 53, 1485(1965).

13. B. A. Auld, "Walker Modes in Large Ferrite Samples", J. of Appl. Phy. 31, 1642(1960).

14. F. R. Morgenthaler, "Exchange Torque, Power and Momentum Flow, and Stress in a Rigid Ferromagnet", Technical Report 10, Microwave and Quantum Magnetics Group, M.I.T.(1966).

15. F. R. Morgenthaler, "Small Signal Power and Momentum Theorems for a Magnetoelastic Ferromagnet", Technical Report 14, Microwave and Quantum Magnetics Group, M.I.T.(1967).

16. F. R. Morgenthaler, "Magnetoelastic Wave Propagation in Time Varying Magnetic Fields", Recent Advances in Engineering Science, Edited by A. C. Eringen, Gordon and Breach, New York(1970).

17. F. R. Morgenthaler, "Photo/Magnon Conversion Near a Material Interface", Elec. Lett. 3, 299(1967).

18. H. L. P. Hu, "Studies of Magnetostatic Waves and Magnetoelastic Waves in YIG using Optical Probing and Microwave Techniques", Technical Report 25, Microwave and Quantum Magnetics Group, M.I.T.(1971).

19. R. W. Damon and H. Van De Vaart, "Propagation of Magnetostatic Spin Waves Microwave Frequencies. II. Rods, J. of Appl. Phy. 37, 2445(1966).

20. R. W. Damon and H. Van De Vaart, "Propagation of Magnetostatic Spin Waves at Microwave Frequencies in a Normally-Magnetized Disk", J. of Appl. Phy. 36, 3453(1965).

21. R. I. Roseph and E. Schlomann, "Demagnetizing Field in Nonellipsoidal Bodies", J. of Appl. Phy. 36, 1579(1965).

22. J. D. Adam, "Delay of Magnetostatic Surface Waves in YIG", Elec. Lett. 6, 718(1970).

23. H. L. Hu and F. R. Morgenthaler, "Strong Infrared-Light Scattering from Coherent Spin Waves in Yttrium Iron Garnet", Appl. Phy. Lett. 18, 307(1971).